Utrecht University

Experimental Physics Master's Thesis

Graduate School of Natural Sciences

A measurement of neutral mesons inside jets in pp - collisions at $\sqrt{s} = 5$TeV

Author:
J.N. Schoppink

First Examiner:
Dr. M. Verweij

Second Examiner:
Dr. A.G. Grelli

Daily Supervision:
Dr. M.H.P.A. Sas
& J.L. König

April 24, 2023

Contents

1 Introduction **5**

2 Theoretical Background **8**

2.1 Particle Physics and High-Energy Collisions 8

2.1.1 The Standard Model 8

2.1.2 Quantum Electrodynamics 9

2.1.3 Quantum Chromodynamics 10

2.1.4 The Quark-Gluon Plasma 11

2.1.5 Jets 12

2.1.6 Proton-proton collisions 13

2.1.7 Neutral mesons and their decay 14

2.1.8 Nuclear modification factor 16

2.2 Monte Carlo Simulations 16

3 Experimental Setup **18**

3.1 LHC 18

3.1.1 ALICE 18

3.1.2 The Electromagnetic Calorimeter (EMCal + DCal) 19

3.1.3 Time Projection Chamber TPC 21

3.1.4 Inner Tracking System 23

4 Data Processing and Analysis Method **24**

4.1 Photon Reconstruction Methods 24

4.1.1 EMC 24

4.1.2 Photon Conversion Method (PCM) 25

4.2 Jet Reconstruction 26

4.2.1 FastJet & the Anti-k_T algorithm 26

4.2.2 Charged Jets & Full Jets 27

4.3 Datasets 28

4.4 Data Cuts 29

4.4.1 Cluster-, Meson-, and Conversion Cuts 29

4.5 Signal Extraction 31

4.5.1 The Invariant Mass Distribution 31

4.5.2 Background Estimation . . . 32
4.5.3 Event Mixing Method . . . 33
4.5.4 Rotational Background . . . 35
4.5.5 Fitting and Integration . . . 37

5 Correcting the raw yield **39**
5.1 The role of Monte Carlo simulations . . . 40
5.2 Correction Steps . . . 40
5.2.1 Unfolding . . . 41

6 Systematic Uncertainties **45**
6.1 Signal Extraction . . . 45
6.2 Jet Reconstruction . . . 45
6.3 Cluster-, Conversion-, & Meson Cut variations . . . 46

7 Results & Discussion **47**
7.1 Overview . . . 47
7.2 EMC, Single Jet-momentum Bin . . . 47
7.2.1 Neutral mesons p_T-dependent Invariant Yields . . . 47
7.3 PCM-EMC, Single Jet-momentum Bin . . . 50
7.3.1 Neutral mesons p_T-dependent Invariant Yields . . . 50
7.4 EMC-EMC, Two Jet Momentum Bins . . . 52

8 Conclusion **56**

9 Additional Discussion **57**
9.1 Systematics . . . 57
9.2 Event mixing over Rotational Background in low statistics . . . 57
9.3 Charged Jets . . . 57
9.4 More Jet momentum bins . . . 58

A Systematic Uncertainty Plots **60**
A.1 Single Jet Momentum Bin: EMC-EMC . . . 60
A.2 Single Jet Momentum Bin: PCM-EMC . . . 63
A.3 Dual Jet Momentum Bins: PCM-EMC . . . 66

A Signal Extraction Plots **69**

A.1 Single Jet Momentum Bin: EMC-EMC 69

A.2 Single Jet Momentum Bin: PCM-EMC 73

A.3 Dual Jet Momentum Bin: EMC-EMC 77

Abstract

This thesis presents a study of jet production and the decay dynamics of neutral mesons (π^0 and η) within those jets in proton-proton collisions, utilizing data from the ALICE experiment at the LHC. Employing both EMC-EMC and PCM-EMC reconstruction methods, the research investigates the momentum-dependent invariant yields of these mesons across various jet transverse momentum ($p_{T,jet}$) ranges and explores the η/π^0 ratio to understand the underlying production mechanisms and their compatibility with theoretical models.

The analysis reveals a marked agreement between the invariant yields within jets and minimum bias measurements for mesons with p_T above the jet momentum threshold, validating QCD's predictions on meson production rates. The study continues into the exploration of the η/π^0 ratio as a function of jet momentum, providing critical insights into meson production dynamics within jets and indicating a nuanced understanding of nuclear modification factors in heavy-ion collisions. Through a segmented p_T bin analysis, the research highlights the jet-momentum dependency of meson production, showcasing the functionality of alternative analysis methods such as the 2D-unfolding method and rotational background calculations, alongside offering a detailed comparison with preliminary measurements.

The findings contribute to our understanding of jet dynamics and meson production mechanisms in high-energy particle physics, offering valuable benchmarks for future theoretical and experimental studies in both pp and heavy-ion collisions. The thesis underscores the importance of re-evaluating existing particle reconstruction methods and detailed analytical techniques in an effort to enhance our comprehension of fundamental physics.

1 Introduction

In 1969, a paper was published on experiments performed at the Stanford Linear Accelerator Center (SLAC), which showed that, contrary to popular belief at the time, protons are not elementary particles and consist of even smaller particles [7]. These particles we know now as 'quarks'. This discovery inevitably led to the development of a theory describing the behavior of these newly discovered particles, Quantum Chromodynamics (QCD). QCD is a key part of the Standard Model of particle physics and provides a framework for understanding the strong interaction, one of the four fundamental forces. It describes the interactions between quarks and gluons, the latter being the force-carrying bosons which bind quarks together. This binding together of quarks is described by a concept called 'asymptotic freedom' and, unlike more familiar forces such as gravity and electromagnetism, dictates that the forces between quarks become stronger, as they move further apart [24]. A direct result of this is that quarks are almost always found bound together in pairs or in groups of three (or as was discovered in 2014, even five) [1], such that together they become 'color-neutral', a property known as 'color-confinement' [24]. Note the use of 'almost always', for if one would try to remove a single quark or anti-quark from its configuration, asymptotic freedom tells us that the required energy to remove it far enough where one could regard it as 'free' becomes enormous. However, it is believed that in the first few microseconds after the Big Bang, the universe was at such a high temperature and density that there was enough energy to free all of its color-charged constituents from their bounds and roam freely in a 'soup' of quarks and gluons . During this very small time-frame, the universe contained a state of matter not discovered until the late 20th century, known as Quark-Gluon Plasma (QGP) [11].

In an attempt to recreate the conditions of the very early universe, scientists have turned to studying heavy-ion collisions such as those created at the Large Hadron Collider (LHC). These collisions are produced at energies high enough to recreate a tiny droplet of QGP for a fraction of a second [10]. To prove that a droplet of QGP was indeed created in the collider and subsequently perform measurements on its properties poses significant challenges as its brief existence and the conditions under which it forms, make the QGP difficult to observe directly. We must therefore turn to indirect measurements of the QGP, by studying remnants of the collision after the QGP has cooled down again and the strong nuclear force has recombined the colour-charged

particles into hadrons. A commonly made analogy is made with studying the aftermath of a car crash to determine what happened in the collision. One such remnant of the collision of particles in high-energy particle accelerators is what we refer to as jets, which are the subject of this thesis.

Jets are products of hard-scattering interactions, which are interactions between partons (quarks and gluons) characterized by exceptionally high momentum transfer. Ejecting partons from the collisions with energies so high that, when demanded by the laws of QCD to become colour neutral, they do so not by turning back, but by using some of their energy to create whole new partons [25]. Some of these newly created particles combine into hadrons and others continue on their own and repeat the process, resulting in a high-momentum shower of particles moving in roughly the same direction; a jet.

The importance of jets in the study of the QGP arises from an effect known as jet-quenching. As the high-energy jet constituents pass through the QGP, interactions with the free color charged particles alter certain properties of the jet [25]. The ways and severity in which the jet is altered due to its interaction with the QGP carries valuable information about the properties of the medium. Information that is conveniently contained in a narrow beam of particles headed (hopefully) straight towards our detector.

Having established the importance of studying heavy-ion collisions, we move on to the role of proton-proton collisions in this field, as protons themselves are too small to be immediately associated with the QGP. To determine if the jets we measure are indeed altered by their propagation through a droplet of QGP, we must compare them to the properties of jets formed in collisions where no QGP is formed, something to function as a baseline measurement, which will be the collision of the simple proton. Together with neutrons, they are the building blocks of the heavy-ions that are used to recreate the QGP. The measurements of jets and their properties inside these 'clean' collisions where the jets are minimally disturbed, will provide a baseline to which we can compare the results obtained from heavy-ion collisions. The study of jets in pp collisions therefore proves a crucial step in learning more about this elusive Quark-Gluon Plasma.

One property of jets which warrants our specific attention is their content of neutral mesons and the ratios between them. Specifically π_0 and η mesons. Sharing a dominant decay channel into two photons, these mesons contribute up to 95% of the total decay photons in high-energy particle collisions [22]. Their prevalence allows for an analysis

rooted in enough statistics to be significant and valuable to our understanding of jets. Combined with their sizeable contribution to the total amount of decay photons, this makes neutral mesons a valuable subject to devote our time to. And with that observation we are now left with no other option than to be excited about the subject matter of this thesis, which presents precisely that; a measurement of neutral mesons inside jets, at $\sqrt{s} = 5\text{TeV}$.

2 Theoretical Background

2.1 Particle Physics and High-Energy Collisions

2.1.1 The Standard Model

The Standard Model (SM) is the foundation of modern particle physics, providing a description of fundamental particles and the interactions associated with three of the four known fundamental forces, excluding gravity, the inclusion of which can perhaps be considered the modern 'holy grail' in physics research.

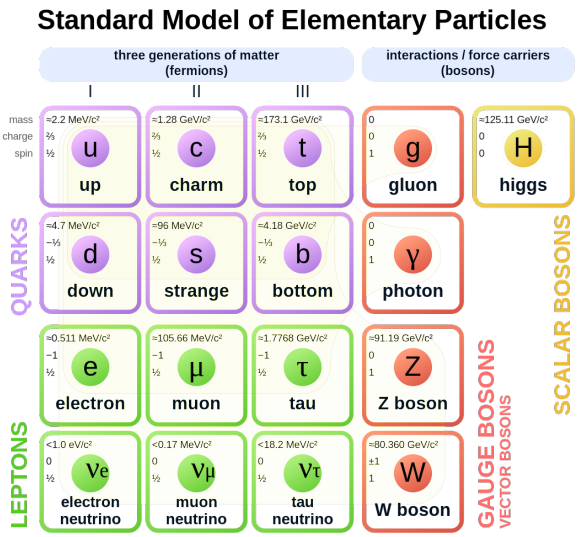

Figure 1: A visualization of the particles described by the standard model

As is nicely illustrated in figure 1, the Standard Model categorizes all fundamental particles into two groups: fermions and bosons.

Bosons, characterized by their integer spin, are the force-carrying particles and the standard model predicts the existence of five types: The photon, the mediator for the electromagnetic interactions, the W and Z bosons, which are responsible for weak nuclear force interactions, and the gluon, the exchange particle for the strong nuclear force. Finally there is the Higgs boson, a spinless excitation of the Higgs field, which interacts with all particles except photons, giving them mass [25].

The fermions are half-integer-spin particles and are the building blocks of matter and are categorized into quarks and leptons, each with six particles divided into three generations. Quarks take part in all of the four fundamental forces and group together to

make up hadrons (protons, neutrons, etc.) and mesons, consisting of a quark-antiquark pair, and including the π_0 and η particles that are the subject of our measurements.

The interactions among fundamental particles are described by quantum field theories: Quantum Electrodynamics (QED) for electromagnetic interactions, Quantum Chromodynamics (QCD) for the strong interactions, and the electroweak theory, which unifies the electromagnetic and weak interactions. The Standard Model Lagrangian encapsulates these theories rather elegantly. Here we see it in its most compact form:

$$\mathcal{L} = -\frac{1}{4}F_{\mu\nu}F^{\mu\nu} + i\bar{\psi}\gamma^{\mu}D_{\mu}\psi + \psi_i y_{ij}\phi\psi_j + \text{h.c.} - V(\phi) \tag{1}$$

This expression summarizes the dynamics of gauge fields ($F_{\mu\nu}F^{\mu\nu}$), the interaction of fermions with those gauge fields ($\bar{\psi}\gamma^{\mu}D_{\mu}\psi$), the Yukawa couplings between fermions and the Higgs field ($y_{ij}\phi\psi_j$), and the Higgs potential ($V(\phi)$), which leads to spontaneous symmetry breaking [24] [25].

Although the Standard Model is not a complete theory, for it fails to incorporate gravity, the focus of this thesis will be primarily on the effects of the strong force and the electromagnetic force, which are both very well described by the standard model.

2.1.2 Quantum Electrodynamics

As the measurements of the neutral mesons performed in the research presented in this thesis are performed by using measurements of the photons into which these mesons decay, it is good to lay some foundation on the theory which describes these photons: Quantum Electrodynamics (QED).

Quantum Electrodynamics (QED) is the quantum field theory (QFT) developed to describe interactions between light (photons) and matter, particularly charged particles, like electrons and quarks. Like all QFTs, excitations in the fields they describe are associated with particles. In the case of QED, that is the photon, an elementary 'quantum' of electromagnetic radiation and mediator of the electromagnetic force.

QED is a gauge theory, a specific type of field theory that is derived from the requirement that its Lagrangian density must remain invariant under a group of local (gauge) transformations, in this case $U(1)$.

The Lagrangian density for Quantum Electrodynamics is given by:

$$\mathcal{L}_{\text{QED}} = \bar{\psi}(i\gamma^{\mu}D_{\mu} - m)\psi - \frac{1}{4}F_{\mu\nu}F^{\mu\nu} \tag{2}$$

where ψ represents the field of the electron (or any other charged particle), $D_\mu = \partial_\mu + ieA_\mu$ is the covariant derivative incorporating the interaction with the electromagnetic field A_μ, m is the mass of the electron, and $F_{\mu\nu} = \partial_\mu A_\nu - \partial_\nu A_\mu$ is the electromagnetic field tensor.

The requirement for the Lagrangian density to be invariant under local $U(1)$ transformations leads directly to the introduction of the electromagnetic potential A_μ in the covariant derivative and the resulting expression completely dictates the interactions between charged particles and the electromagnetic field.

Although the focus of this thesis is on neutral mesons, which lack electrical charge and thus do not directly engage with the electromagnetic field, the electromagnetic force plays a crucial role in their decay mechanism and in their reconstruction. It is, after all, their decay into *photons* that we use to study these mesons. More details on the decay of neutral mesons will be provided in section 2.1.7.

2.1.3 Quantum Chromodynamics

Similarly to QED, Quantum Chromodynamics (QCD) is a quantum field theory (QFT) that describes the interactions between quarks and gluons, the fundamental particles that make up protons, neutrons, and other hadrons. QCD is the theory of the strong nuclear force.

QCD is a gauge theory based on the non-abelian SU(3) symmetry group, in contrast to the U(1) symmetry of QED. This difference in symmetry groups leads to significantly different behaviors between the two theories. While QED deals with the electromagnetic interactions mediated by photons, QCD describes the strong interactions mediated by gluons. Gluons, like photons in QED, are the quanta of the field, but with an important distinction: they carry color charge, the strong force analogue to electric charge in electromagnetism, and can interact with each other.

The Lagrangian density for Quantum Chromodynamics is given by:

$$\mathcal{L}\text{QCD} = \bar{q}i(i\gamma^\mu D\mu^{ij} - m)\psi_j - \frac{1}{4}G\mu\nu^a G_a^{\mu\nu} \tag{3}$$

where q_i represents the field of a quark with color i, $D_\mu^{ij} = \partial_\mu \delta^{ij} + ig_s A_\mu^a T_a^{ij}$ is the covariant derivative that incorporates the interaction with the gluon field A_μ^a, m is the mass of the quark, $G_{\mu\nu}^a = \partial_\mu A_\nu^a - \partial_\nu A_\mu^a + g_s f^{abc} A_\mu^b A_\nu^c$ is the gluon field strength tensor, g_s is the strong coupling constant, T_a are the generators of the SU(3) group, and f^{abc} are the structure constants of SU(3).

The increased complexity of QCD arises from the non-abelian nature of the SU(3) gauge group, which results in self-interaction among gluons. This leads to two unique properties of the strong force: asymptotic freedom, which means that the force between quarks becomes weaker as they come closer together, and as a direct result: confinement, which means quarks and gluons must never be found in isolation but always bound with other quarks in color-neutral combinations.

2.1.4 The Quark-Gluon Plasma

The Quark-Gluon Plasma (QGP), theorized in the early 1970s as a fundamental state of matter which may form under extremely high pressure and temperature, and subsequently discovered through high-energy heavy-ion collision experiments in the early 2000s, represents one of the universe's most extreme environments. This plasma state is achieved at temperatures so high, that the strong nuclear force is no longer strong enough to enforce the concept of color-confinement discussed in Section 2.1.3. The quarks and gluons, which are usually confined within protons, neutrons, and other hadrons, are liberated to form a dense and hot mass of freely roaming color-charged particles.

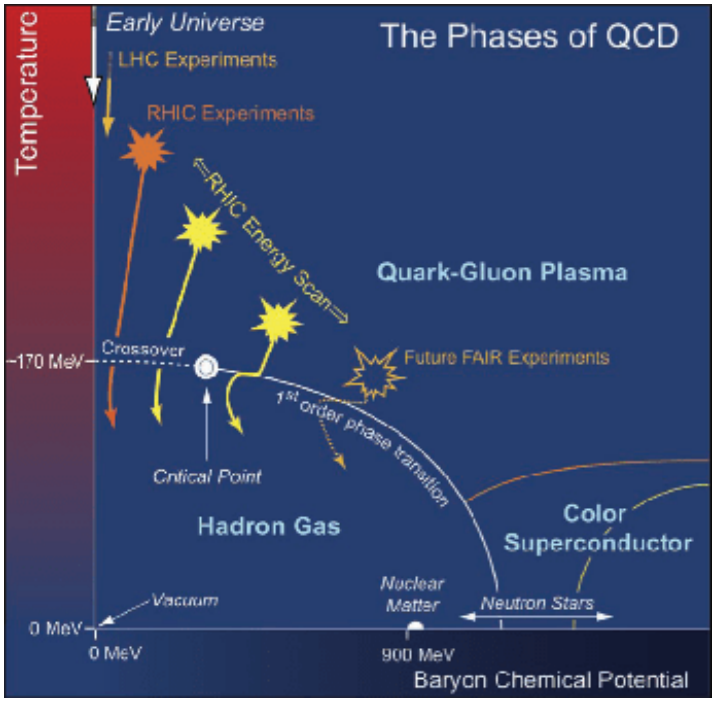

Figure 2: Phase diagram of Quantum Chromodynamics showing the transition from hadronic matter to Quark-Gluon Plasma at high temperature and baryon chemical potential.

The phase diagram of QCD (figure 2 is a useful tool for visualizing what exactly is meant when it is said that the phase transition to a QGP requires extreme conditions. The phase diagram represents the states of nuclear matter as a function of temperature T and baryon chemical potential μ_B, which can be interpreted as the QCD equivalent of thermodynamic pressure; it is a measure of the change in energy of the system as the baryon number (the difference between baryons and antibaryons) is varied:

$$\mu_B = \frac{\partial E}{\partial N_B} \tag{4}$$

Central to the interpretation of the phase diagram is the boundary separating hadronic matter from the QGP. As the baryonic density increases, the required temperature for a phase transition from hadronic matter to a QGP decreases. However, determining exactly when this phase transition occurs, where the hypothetical critical point of the first-order phase transition lies and what happens at the crossover at high temperature and low μ_B, are the subject of a lot of research and are some of the primary objectives in current research into the QGP as the answers to these questions would be extremely valuable to our understanding of QCD and therefore help us understand the workings of the early universe, and the force that keeps most of the matter surrounding us together.

Experimentally, QGP can be studied through high-energy heavy-ion collisions, such as those conducted at the Large Hadron Collider (LHC) at CERN and the Relativistic Heavy Ion Collider (RHIC) at Brookhaven National Laboratory. These facilities accelerate and smash together heavy ions at near-light speeds, creating temperatures and densities high enough for the QGP to form, albeit briefly.

To perform measurements on the QGP and study its properties, scientists use several types of probes. Messengers from inside the QGP that arrive in our detectors long after the QGP has cooled down, but carry valuable information about the conditions inside. One such probe is jets.

2.1.5 Jets

Jets are formed from the hadronization of quarks and gluons produced in the initial, high-energy stages of particle collisions. When two heavy ions collide at near-light speeds, the energy density in the collision region can become sufficient to overcome the forces binding quarks within hadrons, potentially forming a QGP. As the system evolves, quarks and gluons from the plasma, or directly from the collision, undergo

fragmentation and hadronization processes, coalescing into streams of hadrons moving in roughly the same direction. These streams, observed as cones of particles in detectors, are referred to as jets.

Jets serve as an excellent tool for investigating the QGP for several reasons. Firstly, the initial production of quarks and gluons that results in jet formation takes place on a very brief timescale, well before the potential formation of the QGP. This renders jets sensitive to the earliest and most extreme conditions generated in the collision. Secondly, as jets traverse the QGP, they interact with it, losing energy in a phenomenon called jet quenching. The degree of jet quenching is contingent upon the properties of the QGP, such as its temperature and density, making measurements of jet energy loss a valuable means for probing the characteristics of the plasma.

Experimental Physicists use a variety of methods to reconstruct jets from the many particles detected in each event. These include algorithms designed to cluster particles based on their momentum and direction, allowing for the reconstruction of the jet's original energy and direction. Comparing jet measurements in heavy-ion collisions to those in proton-proton collisions, where QGP formation is thought not to occur, provides a baseline for understanding how the presence of the QGP modifies jet characteristics.

2.1.6 Proton-proton collisions

Proton-proton collisions are a fundamental aspect of particle physics research, as they serve as a simpler system for studying the basic interactions between quarks and gluons without the complexity introduced by heavy ions. In the context of QGP and jet studies, proton-proton collisions are particularly valuable because they provide a control experiment against which the results of heavy-ion collisions can be compared. By examining jets produced in proton-proton collisions, physicists can establish a benchmark for jet behavior when QGP is not expected to form. This benchmark is crucial for identifying and quantifying the modifications to jet properties that occur specifically due to the interaction with the QGP in heavy-ion collisions. Moreover, studying proton-proton collisions helps refine the theoretical models of jet production and evolution, which are essential for interpreting the results from more complex systems and for making predictions about the behavior of matter under extreme conditions.

Jet formation in proton-proton collisions is an important part of exploring the strong force. When protons collide at high energies, their constituent quarks and gluons can undergo hard scattering, resulting in the emission of high-energy partons that subse-

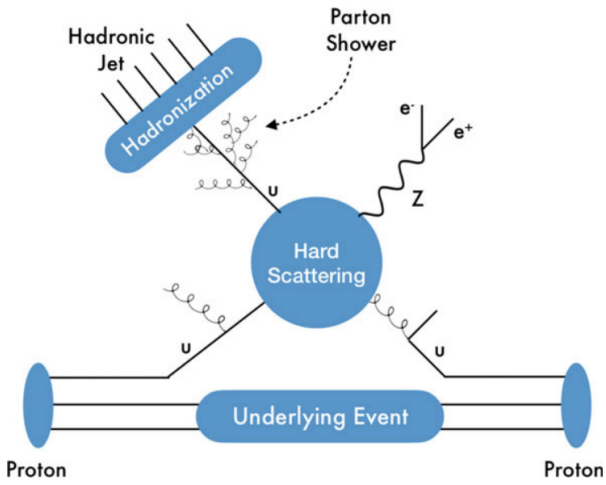

Figure 3: Schematic representation of a pp collision, involving a quark-gluon hard-scattering that leads to a final state consisting of a Z boson and a jet

[19]

quently evolve into jets, as depicted in Figure 3. This process provides a testing ground for perturbative Quantum Chromodynamics (pQCD) predictions, enabling physicists to probe the internal structure of protons through the study of parton distribution functions.

2.1.7 Neutral mesons and their decay

At last we now have discussed all of the background needed to invite the main protagonist of this thesis onto the stage, the neutral mesons. Specifically, the π_0 and η mesons. These hadrons are composed of a quark and its corresponding antiquark. Specifically, the π^0 is made up of an up quark and an anti-up quark, or a down quark and an anti-down quark, with the quarks in a quantum superposition of these states. The η meson is more complex, being a mixture of up, down, and strange quark-antiquark pairs. These mesons are not stable particles; they are produced in high-energy processes and quickly decay into other particles.

The π^0 meson is the lightest hadron (and therefore, lightest meson) predicted by the Standard Model and has a very short lifetime, around 8.52×10^{-17} seconds, and predominantly decays into two photons (γ), which is a process mediated by the strong and electromagnetic interactions. The decay can be expressed as:

$$\pi^0 \rightarrow \gamma + \gamma.$$

This decay mode accounts for approximately 98.823% of all π^0 decays, making it the most common decay path.

The η meson, on the other hand, is a bit heavier and has an even shorter lifetime of about 5×10^{-19} seconds, and its decay is less dominated by the two-photon decay mode, although still the largest contribution:

$$\eta \to \gamma + \gamma.$$

Additionally, the neutral η meson can also decay into three pions, either all neutral ($\pi^0\pi^0\pi^0$) or two charged and one neutral ($\pi^+\pi^-\pi^0$), among other less common decay channels. The decay into two photons occurs about 39% of the time, while the decays into three pions occur approximately 32.5% and 23% for the neutral and charged modes, respectively. [17]

The decays of neutral mesons are of particular interest because they proceed through the electromagnetic interaction, despite the fact that the mesons are formed due to the strong interaction. These decay processes are well-explained by quantum electrodynamics (QED), and the Feynman diagrams representing the two-photon decay modes of π^0 and η mesons share similarities. Both processes involve a virtual quark loop that interacts with the final state photons. [17]

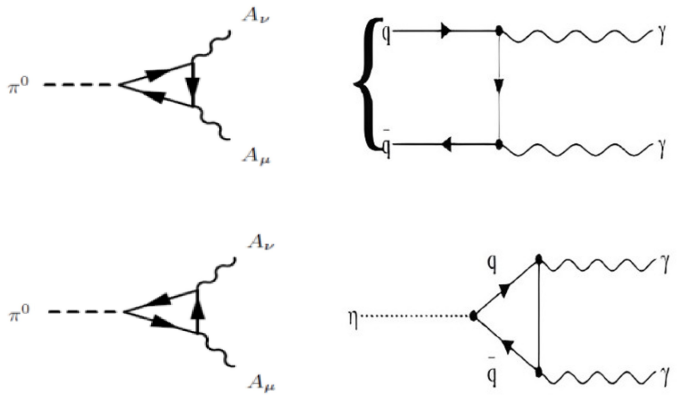

Figure 4: Feynman diagrams depicting Feynman diagrams for the two-photon decay of (left) the π^0 meson and (right) the η meson.

2.1.8 Nuclear modification factor

The nuclear modification factor R_{AA} is used to compare the particle yield in heavy-ion collisions, specifically lead-lead (Pb-Pb) interactions, with the yield expected from proton-proton (pp) collisions. Its main purpose is to detect any deviations from the baseline established by pp collisions, which would indicate the presence of nuclear effects in the heavy-ion environment. In this work, the baseline will be presented as the ratio η/π_0. Mathematically, R_{AA} is defined as:

$$R_{AA} = \frac{\frac{d^2N_{AA}}{dp_T dy}}{T_{AA} \cdot \frac{d^2\sigma_{pp}}{dp_T dy}}$$

Here, $\frac{d^2N_{AA}}{dp_T dy}$ represents the differential yield of particles in a heavy-ion collision with respect to transverse momentum p_T and rapidity y, while $\frac{d^2\sigma_{pp}}{dp_T dy}$ is the corresponding differential cross-section in pp collisions. The quantity T_{AA} is the nuclear thickness function, which is related to the number of binary nucleon-nucleon collisions in the overlap region of the colliding nuclei. The η/π_0 ratio measured in this work serves as a reference point, as any results obtained from it, such as particle yields, can be attributed solely to simple QCD interactions and hard scattering processes. On the other hand, in heavy-ion collisions, the presence of the quark-gluon plasma can significantly affect particle production. Therefore, any deviations of R_{AA} in Pb-Pb collisions can be attributed to QGP-related effects.

2.2 Monte Carlo Simulations

Monte Carlo simulations are computational algorithms that rely on repeated random sampling to calculate their outcomes. These simulations are named after the well-known Monte Carlo Casino in Monaco because they depend on random number generators. They are widely used in various scientific fields such as physics, finance, and engineering. The fundamental principle of Monte Carlo methods is to use statistical sampling to mimic the intricate behavior of systems and obtain numerical solutions for problems that may be theoretically deterministic but too complicated for analytical solutions. By conducting numerous simulations and averaging the results, Monte Carlo methods can approximate the behavior of an complex systems, even if the specific interactions within the system are unpredictable. This makes them particularly valuable for investigating phenomena that are influenced by chance events or are otherwise difficult to determine

analytically.

The core concept of Monte Carlo simulations relies on generating random numbers, which are utilized to sample from probability distributions that represent the system being studied. These distributions can range from simple, such as the uniform distribution, to more complex ones tailored to specific physical processes. The law of large numbers is a fundamental principle that ensures the average of the simulation approaches the expected value as the number of trials increases. Additionally, the central limit theorem guarantees that, under certain conditions, the distribution of the simulation results will converge to a normal distribution, regardless of the underlying distribution of the random variables. This is crucial for the reliability of the method, as it enables the estimation of uncertainties and confidence intervals around the simulated outcomes. In this context, convergence refers to the point at which increasing the number of simulations leads to diminishing returns in terms of the precision of the estimated results.

3 Experimental Setup

3.1 LHC

The Large Hadron Collider (LHC) holds the record for the world's largest particle accelerator, featuring a 27-kilometer circular track of superconducting magnets situated beneath the French-Swiss border. This impressive piece of technology is able to propel proton and lead-ion beams to velocities approaching that of light, resulting in collision energies of up to 13TeV. The European Organization for Nuclear Research (CERN) oversees the construction and maintenance of a number of physics research projects, of which the LHC is the largest. As an intergovernmental organization comprising 23 member states, CERN's collaborative efforts provide scientists from these countries and beyond with the means to extend the boundaries of particle physics and conduct research that would have been impossible without this remarkable display of human ingenuity and cooperation.

The LHC's circular track is home to four major detectors — ATLAS, CMS, ALICE, and LHCb—each with its own distinct research focus. ATLAS and CMS serve as general-purpose detectors, dedicated to investigating a wide range of physics phenomena, including the quest for the Higgs boson and other discoveries beyond the Standard Model. LHCb specializes in elucidating the disparities between matter and antimatter, contributing to our understanding of the early universe's asymmetries. And finally, ALICE is specifically designed to explore the properties of quark-gluon plasma, which is also the underlying incentive for the research presented in this thesis.

3.1.1 ALICE

A Large Ion Collider Experiment (ALICE), is one of the LHC's four main experiments and is optimized for heavy-ion physics. Its primary objective is to study the quark-gluon plasma, a state of matter believed to have existed just after the Big Bang. The detector is equipped with a solenoid magnet and an array of sophisticated detection systems capable of tracking thousands of particles simultaneously. The ALICE detector stands out for its capability to handle the highest particle multiplicities that occur during lead-lead collisions at the LHC. This makes it a strong tool for studies into the extreme conditions of the early universe and the strong force that binds quarks and gluons into nucleons.

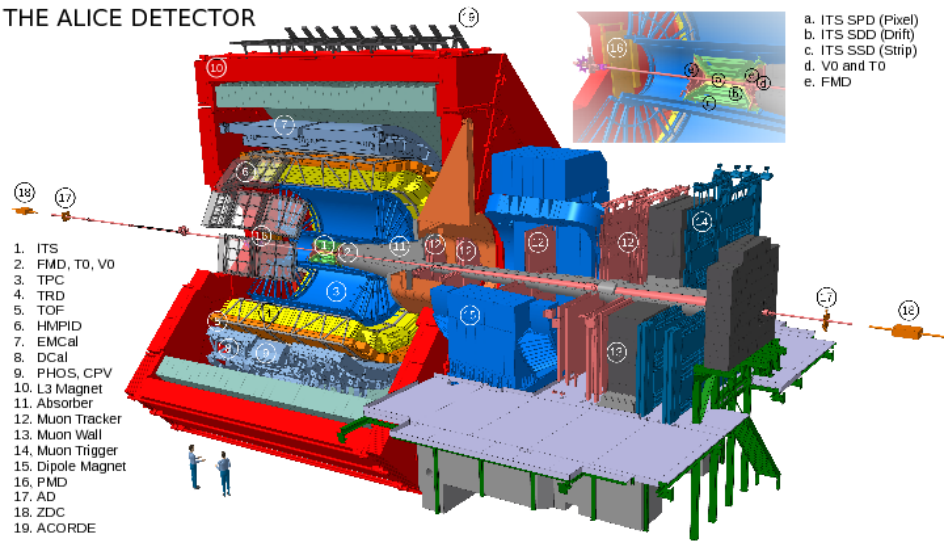

Figure 5: A schematic overview of the ALICE detector, with a legend naming the large components and humans to scale to give an indication of its size.

The ALICE detector is designed primarily to study lead-lead collision events and has a configuration designed with this specific purpose in mind. It is a large cylindrical structure that is 26 meters tall and has a diameter of 16 meters. Figure 5 provides a schematic representation of the detector, showing its complex layout and large size. The ALICE experiment consists of multiple detector systems arranged concentrically around the beam pipe, which is the central point for high-energy collisions produced by the LHC. The Inner Tracking System is positioned closest to the beam pipe and captures the trajectories of particles after the collision. The Time Projection Chamber surrounds the Inner Tracking System and provides tracking and particle identification data over a larger volume. The Time-Of-Flight detector, located around the inner layers, is important for determining particle velocity by measuring the time it takes for particles to reach it, which helps in particle identification. The detector also includes electromagnetic calorimeters and muon spectrometers on the periphery, which are dedicated to measuring the energy of photons, electrons, and heavier particles. By combining data from all these components, a detailed analysis of the collision events can be performed, leading to a better understanding of their nature.

3.1.2 The Electromagnetic Calorimeter (EMCal + DCal)

The Electromagnetic Calorimeter (EMCal) is a system of calorimeters within the ALICE experiment designed to measure the energy of photons and electrons emerging from the collisions. As particles pass through the EMCal, they interact with the material of

the detector and undergo a cascade of secondary particles called a shower. The EMCal measures the collective energy of these showers, allowing the energy of the original particle to be determined with high precision. This information is vital for reconstructing the events that occur during collisions and for identifying processes that involve highly energetic photons such as events with jets.

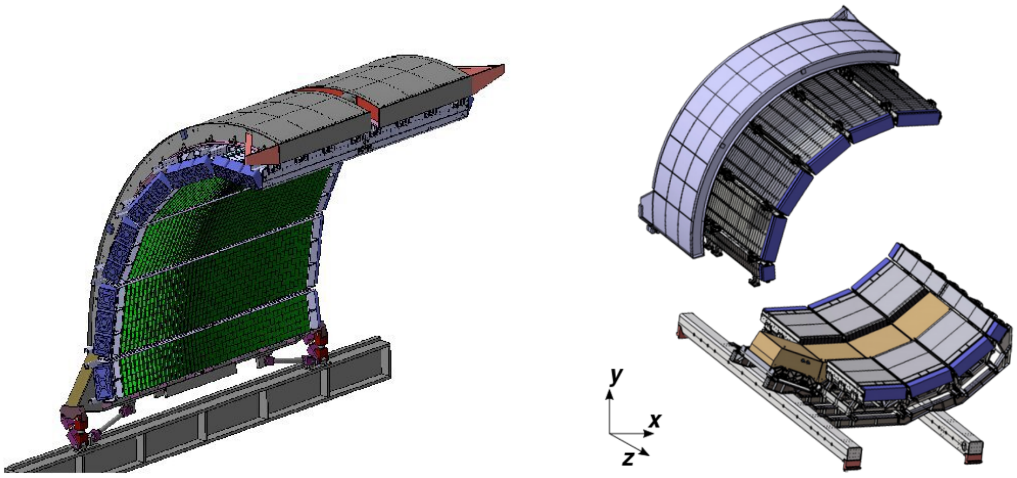

Figure 6: Left: Engineering schematic of the EMCal as it was during LHC run 1 with its mechanical support structure (grey), electronics read-out (blue) and the modules containing the photoscintillating polystyrene (green). Right: A schematic representation of the complete EMCal system with the original EMCal module (top) and the complementary DCal (bottom) that was added in the long shutdown between LHC runs 1 and 2 [23, 9]

The EMCal's ability to accurately measure particle energy relies on scintillating materials, photodetectors, and electronic read-out systems. The scintillating materials within the EMCal are designed to produce light when struck by a particle. This light is then captured by Avalanche Photo Diodes (APDs) and converted into an electrical signal through a direct connection to a Charge Sensitive Preamplifier (CSP) [9]. The strength of this signal is proportional to the energy of the particle that initiated the shower, allowing for precise energy measurements. The electronic readout systems are tasked with processing these signals, digitizing them, and preparing the data for further analysis. By combining the scintillating properties of its materials with efficient photodetection and sophisticated electronics, the EMCal plays an essential role in a big part of the research done by the ALICE Collaboration, as it does in the research presented here.

During the first long shutdown (LS1) of the LHC, which started early 2013 and lasted almost two years, the EMCal was complemented by the addition of the Di-Jet Calorimeter (DCal). This second large calorimeter sits exactly opposite the EMCal

in azimuth, for the specific purpose of making the combined system *much* more fit to analyze di-jet events. Di-jet events are events where two high momentum jets are created with opposite momentum vectors, and are to a large extent - though in *pp* collisions, not perfectly - associated with a narrow, pencil-like event shape [21]. For our research, the orientation of jets relative to each other is not very relevant, but we will gratefully use the DCal data to increase the size of our dataset. In the rest of this thesis, we will refer to the combined system of EMCal+DCal as simply 'EMCal' and only refer to the DCal specifically, in situations where making the distinction is relevant.

3.1.3 Time Projection Chamber TPC

The Time Projection Chamber (TPC), part of the Inner Tracking System (ITS), takes on the role of main device for tracking charged particles. By detecting the position and momentum of these particles, the TPC provides essential data for reconstructing their trajectories after they emerge from high-energy collisions. It does this by allowing particles to ionize the Ne-CO_2-N_2 gas within its volume, which spans from 85 cm to 250 cm radially from the beam pipe and is kept at atmospheric pressure.

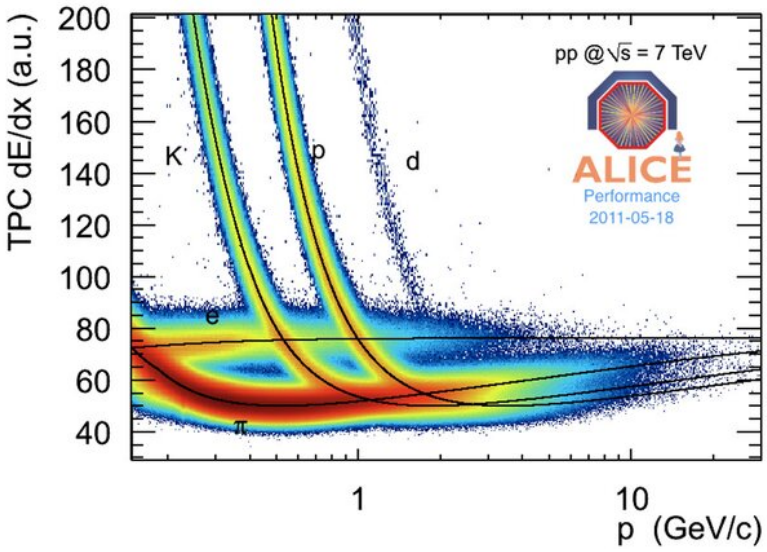

Figure 7: The specific ionization energy loss vs. transverse momentum in the TPC. The letters indicate each particle species and each black line represents the parameterization for that species. [23]

The paths of charged particles reconstructed using the TPC data will be curved due to the electric field in the TPC and can therefore be used for particle identification by calculating the specific energy loss dE/dx. By analyzing the dE/dx profiles, an observable that is dependent on the particle's mass, charge and momentum, scientists

can distinguish between different types of particles, such as electrons, protons, and charged pions. Figure 7 helps visualize this identification process.

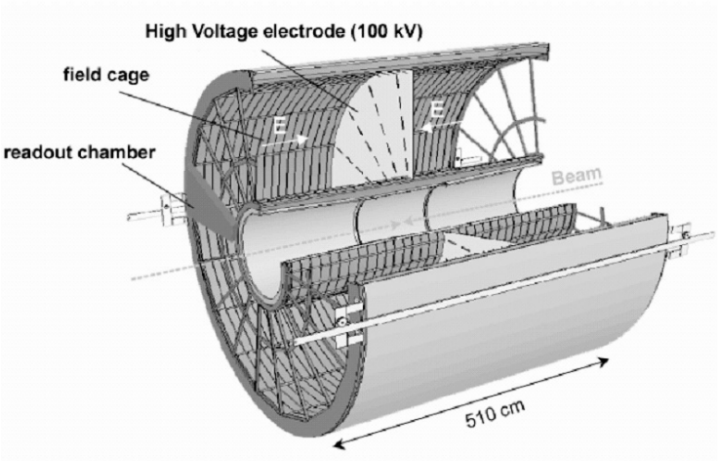

Figure 8: Layout of the ALICE TPC detector. [20]

3.1.4 Inner Tracking System

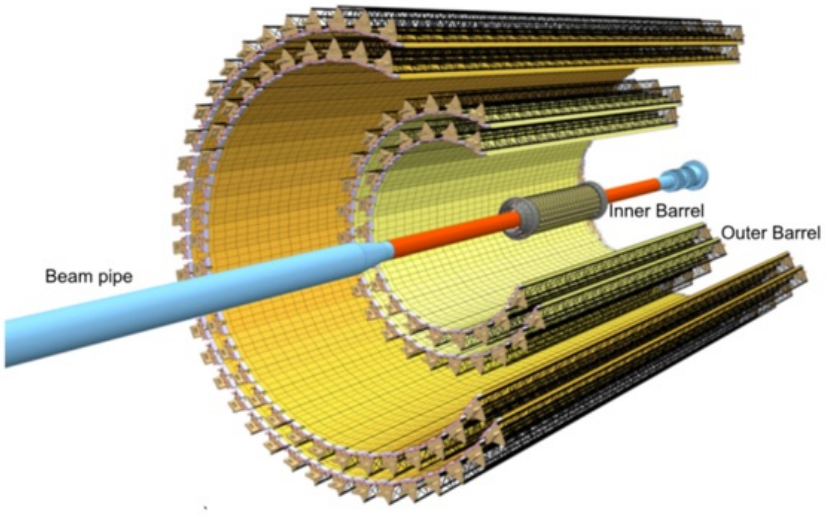

Figure 9: Schematic overview of the Inner Tracking System (ITS) detector at ALICE

The Inner Tracking System (ITS) provides precise tracking and pinpointing of particle collision points. Located nearest to where collisions occur, the ITS is comprised of six high-resolution silicon detector layers: the Silicon Pixel Detectors (SPD), Silicon Drift Detectors (SDD), and Silicon Strip Detectors (SSD), situated within a radius range of 4 to 43 cm from the collision point. These layered detectors offer exceptional spatial resolution, crucial for accurately pinpointing the locations of primary and secondary vertices—the points where particles either originate or decay. The ITS, with a pseudorapidity coverage of $|\eta| \leq 0.9$, aims to locate the primary vertex with a precision better than 100 μm. The SPD, being the innermost layers, is especially important for its role in tracking and identifying particles very close to the collision point. [14]

The ITS works by detecting the charged particles produced in collisions as they traverse its six silicon layers, which record a precise hit. By connecting these hits, the path of the particle can be reconstructed with improved momentum and angle resolution, thanks to the ITS's enhancement of the tracking capabilities when used in conjunction with the Time Projection Chamber (TPC). This ability to track particles with such precision is vital for measurements that require an understanding of the particle's origin. The outer four layers of the ITS, with their analog readout, measure the energy loss per unit length due to ionization, which helps identify particles moving at lower momenta using only ITS data.

4 Data Processing and Analysis Method

4.1 Photon Reconstruction Methods

In this thesis, we distinguish two distinct methods of photon reconstruction, each utilizing data from different detectors. The first method, referred to as EMC, involves reconstructing the momentum of a photon that has interacted with the EMCal detector material, causing an electromagnetic shower. The process of deducing the photon's momentum from this interaction will be elaborated upon in section 4.1.1. The second method is the Photon Conversion Method (PCM), which focuses on reconstructing photons that have converted into an electron-positron pair, using data from the Inner Tracking System (ITS) and the Time Projection Chamber (TPC). This method will be detailed further in section 4.1.2.

4.1.1 EMC

When particles interact with the EMCal, they generate electromagnetic showers that typically spread their energy over multiple neighboring cells. The calorimeter cells, sensitive to both charged particles and photons, produce a signal in response to this energy deposition. However, as this energy deposition takes on the shape of a shower, all of the energy rarely ends up in a single calorimeter cell. The next step, therefore, is clusterization. This involves combining the signal from multiple, neighbouring cells into clusters. These clusters represent the total response of the calorimeter, which can then be used to determine the total energy of the particle.

The process of clusterization in the EMCal begins with the identification of a seed hit, which is a cell with an energy deposit exceeding a certain threshold. Surrounding cells with lower, but significant, energy deposits are then aggregated around this seed hit to form a cluster. This is done by an iterative process where a cluster C is formed by a seed cell s and its neighboring cells n_i, if the condition $E_{n_i} > E_{\text{threshold}}$ is fulfilled. Here, E_{n_i} is the energy of the i-th neighboring cell. The total energy E_{total} of the cluster can be calculated as:

$$E_{\text{total}} = \sum_{i \in C} E_i = E_s + \sum_{n_i \in C} E_{n_i}, \tag{5}$$

where E_s is the energy of the seed cell and E_{n_i} are the energies of the neighboring cells included in the cluster. After clusterization, the centroid position of the cluster

is determined, often by a weighted average of the cell positions, taking their energy deposits as weights. This provides a more accurate determination of the particle's position and, consequently, its energy.

The EMCal detector's capability to identify both charged particles and photons, along with the large number of particles produced in these collisions, may lead to several particles striking the detector at nearly the same time and place. Fortunately, for charged particles like electrons, the clusters can be associated with tracks identified in the Inner Tracking System (ITS). By extending these trajectories, we can determine the location where these particles will interact with the EMCal, as well as the amount of energy they will release. This capability is particularly advantageous in photon reconstruction, as it allows for the removal of a large background signal from energy deposited by charged particles, thereby minimizing noise in the photon signal.

4.1.2 Photon Conversion Method (PCM)

The second method that will be used for the research in this thesis is the Photon Conversion Method (PCM), which exploits the fact that photons can convert to electron-positron pairs in the presence of an atomic nucleus. This process is an example of 'pair production', which is an umbrella term for all processes that lead to the production of a particle-antiparticle pair. The PCM technique involves detecting these daughter particles using the Inner Tracking System (ITS) and the Time Projection Chamber (TPC) of the detector apparatus. By reconstructing these tracks and extrapolating them back to their common origin, we can calculate the momentum vector of the original photon.

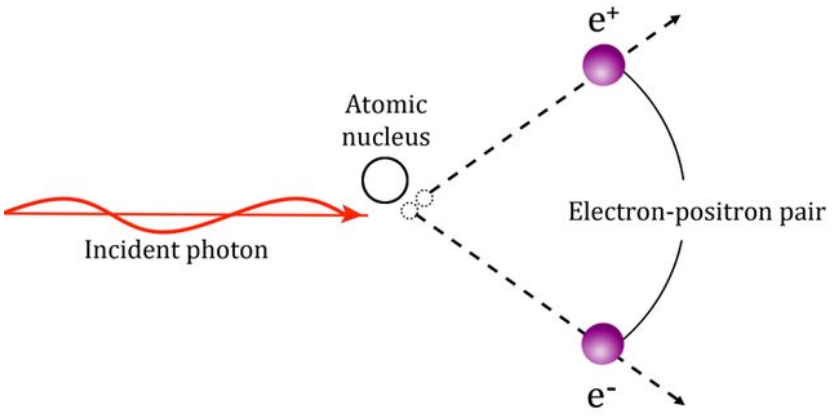

Figure 10: Schematic example of pair production; a photon interacts with a nucleus (in the detector material) and converting to a electron-positron pair. [18]

The probability of a photon converting to a e^+e^- pair is relatively small, influencing the amount of statistic provided by this method. This probability depends on the distance the photon travels through the detector material, and the material's radiation length X_0. The conversion probability per unit length is given by:

$$P_{\text{conv}}(x) = \frac{1}{X_0} e^{-x/X_0}, \tag{6}$$

where x is the distance traveled by the photon in the material. In practice, PCM requires a precise tracking system to detect the relatively few photon conversions that occur. Once an electron-positron pair is detected, their momenta are measured, the invariant mass of the system can be calculated to verify that it is consistent with a photon conversion. This method complements the detection of photons in the EMCal by providing a way to reconstruct photons that did not interact with the calorimeter, thus improving the overall photon detection efficiency of the ALICE experiment.

4.2 Jet Reconstruction

4.2.1 FastJet & the Anti-k_T algorithm

Now that we have covered the tools used to find the photons from which we will reconstruct the neutral mesons, the next step is to identify the jets in which we are to look for them, because although there are a lot of them inside jets, also many of them are not. For this task, the FastJet package is used. FastJet is a software library that offers various algorithms and tools specifically designed to efficiently detect and reconstruct jets in particle collisions. One of the algorithms included in the FastJet package is the anti-k_t algorithm, known for returning jets with a regular, conical shape and being less affected by soft radiation and contributions from the underlying event compared to other jet-finding algorithms [8]. We will discuss briefly the inner workings of this algorithm.

The anti-k_t algorithm clusters particles based on their relative angular separation and transverse momentum. It gives priority to combining particles with higher transverse momentum, resulting in stable and well-defined jets even when there are softer background particles. In FastJet, this algorithm is implemented using an iterative combination procedure. Consider the the final state particles of the collision as a list of "protojets". For each protojet, define d_{iB} as the square of the protojets momentum and for each combination of protojets, define a distance d_{ij} between protojets i and j.

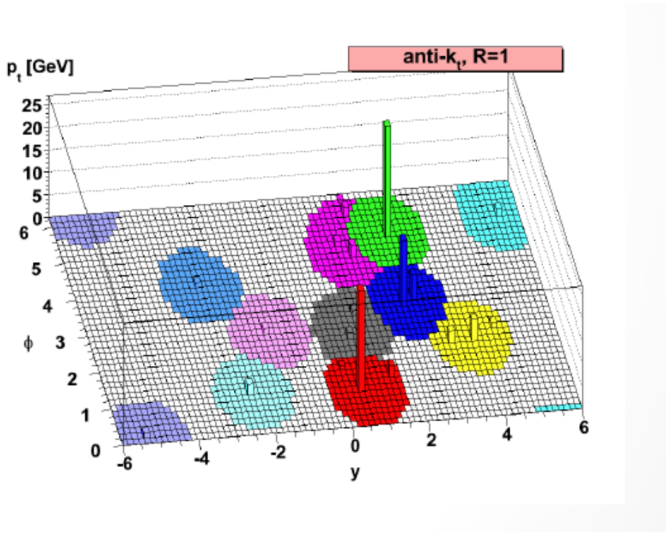

Figure 11: A schematic representation of the result of the anti-k_T algorithm, using a simulated parton-level event, along with numerous randomly distributed soft "ghosts." These have been organized by the anti-k_T algorithm to show the "active" areas of influence for the resulting hard jets. [8]

Then for any protojet i find the smallest value among these. If the smallest value is one of the d_{ij} values, add it to the protojet. If d_{iB} is the smallest value, call i a jet and move on to the next. The distance metric d_{ij} is chosen to be inversely proportional to the transverse momentum squared, ensuring that the shape of the jets is not affected by low-momentum noise. The expression for d_{ij} reads.

$$d_{ij} = \min(k_{ti}^{-2}, k_{tj}^{-2}) \frac{\Delta R_{ij}^2}{R^2}, \tag{7}$$

$$d_{iB} = k_{ti}^{-2} \tag{8}$$

where k_{ti} and k_{tj} are the transverse momenta of particles i and j, respectively, denoted with k_t instead of p_T to specifically refer to parton transverse momentum [15]. The expression $\Delta R_{ij}^2 = (\eta_i - \eta_j)^2 + (\phi_i - \phi_j)^2$ defines the squared distance between the two particles in the rapidity-azimuth space. η represents the rapidity, and ϕ represents the azimuthal angle. R is the radius parameter used by the jet clustering algorithm and has been set to $R = 0.4$ for all jets found in this research. [8]

4.2.2 Charged Jets & Full Jets

In the analysis of ALICE data, the reconstruction of jets distinguishes between charged jets and full jets. It is important to emphasize that, from a physics perspective, they are identical. The distinction lies solely in the reconstruction process. When only charged particles are used for jet reconstruction, the resulting jets are referred to as "charged

jets". The rationale for using only charged particles is related to the acceptance of the different detectors of the ALICE experiment. By sacrificing the slightly improved reconstruction that the inclusion of neutral particles would provide (the neutral energy fraction in the data analyzed in this thesis is approximately 17%), we can take advantage of the full acceptance of the ITS+TPC. As previously discussed, the Photon Conversion Method also utilizes these detectors and therefore has the same acceptance region. Consequently, its value is most evident in meson analysis methods that involve one or two photons from the PCM (i.e., PCM-PCM and PCM-EMC).

Full jets, on the other hand, include both charged and neutral particles and are reconstructed by combining track information from the ITS+TPC (both part of the central barrel) with EMCal data [16]. The inclusion of EMCal data comes at the cost of limiting our acceptance to that of the EMCal, which corresponds to $|\eta| \leq 0.7$ in pseudorapidity and an average azimuthal range of approximately 150 degrees (the azimuthal range of DCal is limited for $|\eta| \leq 0.22$), significantly smaller than that of the central barrel, which covers the full azimuthal angle ϕ and $|\eta| \leq 0.9$ in pseudorapidity. However, despite the reduction in the range in which we can search for jets, the additional EMCal data, which contains information on neutral particles, allows for a more complete reconstruction of the jet.

Moreover, the photon reconstruction efficiency of the EMCal is much higher than that of the Photon Conversion Method. As we will later see in this thesis, this leads to the meson reconstruction method that uses two photons from the EMCal data (see section 4.1.1) offering a larger statistical sample than the methods where one or both photons are reconstructed with the PCM, despite the limited acceptance of the EMCal detector. For the EMC method, it appears that full jets are the superior choice, as this method is already limited to the acceptance of the EMCal.

4.3 Datasets

For this research, the following datasets were used:

- Data: `LHC17_5TeV_pass1_FASTandwoSDD_AOD234`
- (JJ)MC: `PYT8JJ_5TeV_anchLHC17pq_p1`

The `LHC17_5TeV_pass1_FASTandwoSDD_AOD234` dataset includes data taken from November 10 to November 19, 2017, with interactions occuring at a rate of 50 kHz.

The High Level Trigger (HLT) mode was set to C, and the FAST cluster was active for all runs. Notably, around 60% of the events were recorded without Silicon Drift Detector (SDD) information due to the SDD being busy when the trigger was issued. The total number of events recorded is 1181 million across all triggers, with 1063 million attributed to the kINT7 FAST trigger.

For Monte Carlo we use the dataset `PYT8JJ_5TeV_anchLHC17pq_p1`. This is a PYTHIA8-generated dataset, containing roughly 178 million simulated events. Although this is a smaller number than the detector dataset that is used, this is compensated by the use of PYTHIA's `HardQCD:All` flag (indicated by the `JJ` (Jet-Jet) in `PYT8JJ`. This sets up the simulation such that a large momentum transfer hard scattering event is forced. Since these events cause jets, the relative amount of events with jets in our dataset becomes much higher ($\sim$ 84% of JJMC event contain jets, as opposed to $\sim$ 38% in our detector dataset). Because of this, the usable amount of events for this work is similar for both datasets. Furthermore, this JJMC dataset is anchored to the `LHC17p` and `LHC17q` data taking periods, mimicking the detector conditions of the period in which our detector data was obtained.

4.4 Data Cuts

The amount of data gathered by the ALICE detector is massive. Being such a complex experiment, with so many components working together, not only from ALICE itself but also the LHC and the collisions it produces, not every data point can be perfect. Many variables influence what parts of the many terabytes of data are valuable to our analysis. In an effort to improve the quality of our analysis by using only data most suitable for it, we apply cuts to the data. The various types of cuts will be discussed in this section.

Firstly, we apply cuts on entire events. The most basic requirement for an event to even be stored in the ALICE data server is called the minimum bias 'trigger', INT7. Which will be the trigger used in this work. It requires activation of both the V0A and V0C detectors, two disks of plastic scintillator material, covering pseudorapidity range $2.8 \leq \eta \leq 5.1$ and $-3.7 \leq \eta \leq -1.7$.

4.4.1 Cluster-, Meson-, and Conversion Cuts

Then for the photons detected in the events that activated the minimum bias trigger, more cuts are applied with regards to the clusters in the EMCal detector (cluster

cuts), the photon conversion method (conversion cuts) and cuts determining which combinations of photons can be used to fill the invariant mass histogram (meson cuts). The numerical values of the cuts applied can be found in tables 1, 2, and 3.

Cluster Cut	**Cutoff Value**
η_{cluster} range	$-0.67 < \eta_{\text{cluster}} < 0.66$
ϕ_{cluster} range	$1.40 < \phi_{\text{cluster}} < 3.28$
$\phi_{\text{cluster}}^{\text{DCAL}}$ range	$4.56 < \phi_{\text{cluster}}^{\text{DCAL}} < 5.70$
Time difference	-20.00 ns $< \Delta T < 25.00$ ns
E_{cluster}	> 0.70 MeV
M_{02} (Shower shape)	$0.10 <$ M02 < 0.50

Table 1: Cluster Quality Cuts for EMCal photons. Here, η is the pseudorapitidy, a measure for the angle with the beam axis, $\eta = 0$ being perpindicular to the beam. ϕ is the azimuthal angle, cut in two pieces for EMCal and DCal as separate parts. The time difference is the time around the arrival of the 'seed' particle that a cluster will take measurements as being from a single shower. $E_{cluster}$ is the minimum energy. The second moment (M_{02}) of a cluster in the EMCal, related to the lateral spread of the energy deposition.

Conversion Cut	**Cutoff Value**
Pseudorapidity (η)	$\lvert\eta_e\rvert < 0.80$
Electron Transverse Momentum (p_T)	$p_{T,e} \geq 0.05$ GeV/c
Photon Transverse Momentum (p_T)	$p_{T,\gamma} > 0.02$ GeV/c
Particle Identification	
Electron Identification ($n\sigma_{e,TPC}$)	$-3 < n\sigma_{e,TPC} < 4$
Pion Rejection ($n\sigma_{\pi,TPC}$)	$n\sigma_{\pi,TPC} < 1$ for $0.40 < p_{T,e} < 3.50$ GeV/c $n\sigma_{\pi,TPC} < 0.50$ for $p_{T,e} > 3.50$ GeV/c
Photon Selection	
Invariant Mass Cut (q_T)	$q_T < 0.05$ GeV/c
Pair Angle Cut (ψ_{pair})	$\lvert\psi_{pair}\rvert < 0.18 \times e^{-0.06\chi^2}$
Conversion Radius (R_{conv})	5 cm $< R_{conv} <$ 180 cm
Conversion distance in Z (Z_{conv})	$\lvert Z_{conv}\rvert < 1000$ cm
Conversion Pseudorapidity (η_{conv})	$\lvert\eta_{conv}\rvert < 0.80$
TPC Clusters/Findable Clusters Ratio	> 0.60
Cosine of Pointing Angle ($\cos(\theta_{point})$)	$\cos(\theta_{point}) > 0.85$

Table 2: Summary of Conversion Cuts. These cuts are specific to the PCM, and are therefore only relevant for the PCM-EMC method.

Meson Cut	**EMC**	**PCM-EMC**
Rapidity (y)	$\lvert y\rvert < 0.80$	$\lvert y\rvert < 0.80$
Opening angle	$\theta_{\text{open}} > 0.0170°$	$\theta_{\text{open}} > 0.0050°$
Momentum Asymmetry	$\alpha < 1.00$	$\alpha < 1.00$

Table 3: Meson Selection Cuts for the meson reconstruction methods EMC-EMC and PCM-EMC. These are cuts that are applied upon the combination of two photons to fill the invariant mass distribution.

Additionally, for this research we will disregard any meson reconstruction that does not result in a meson momentum vector that is inside a reconstructed jet (see section 4.2 about jet reconstruction). This jet must have a transverse momentum $p_{T\text{Jet}} \geq 5\text{GeV}$ and we consider only the combined momentum vector of the photons. If one or both photons end up outside of the jet cone, the meson will still enter the analysis.

4.5 Signal Extraction

4.5.1 The Invariant Mass Distribution

After recording the photons using the Electromagnetic Calorimeter (EMC) or Photon Conversion Method (PCM), we proceed to isolate the signal of neutral mesons from the gathered data. This involves pairing photons and computing their combined invariant mass (M_{inv}). The invariant mass is a measure of the system's mass, that is constant regardless of the its velocity. This reasoning means we can consider both a meson and its decay particles as systems with equivalent invariant mass. In the context of our search for neutral mesons, the invariant mass is what one would observe if the meson were at rest (or, for scientific correctness: in the meson's rest frame). Generally, it can be calculated using the energy and momentum of the decay products through the equation:

$$m_{\text{inv}}^2 = E_{\text{total}}^2 - \vec{p}_{\text{total}}^2 c^2, \tag{9}$$

where E_{total} is the total energy of the decay products, $\vec{p}_{\text{total}}$ is their total momentum, and c is the speed of light. For our case of a neutral meson decaying into two photons, we can use that photons are massless and thus $E_\gamma = p_\gamma c$, and after some algebraic manipulation, the relationship simplifies to:

$$m_{\text{inv}}^2 = 2E_{\gamma 1}E_{\gamma 2}(1 - \cos\theta_{\gamma\gamma}), \tag{10}$$

where $E_{\gamma 1}$ and $E_{\gamma 2}$ are the energies of the two photons, and $\theta_{\gamma\gamma}$ is the angle between their momenta.

This is a very powerful metric in particle analysis, because it is a property that is intrinsic to each particle species. Reconstructing the m_{inv} of two photons, or any other complete collection of daughter particles, that originate from a π_0 decay will always yield the same result (with some degree of uncertainty, of course). This combining of the momenta of decay products to calculate the invariant mass is therefore a crucial

part of the analysis done in this thesis, and in experimental particle physics in general.

Now, recognizing that this invariant mass is in some sense a fingerprint of a particle species, the next step is to plot the m_{inv} for all photon pairs. Such a graph is known as an invariant mass distribution, as shown in figure 12. We then count the ones that coincide with the expected meson mass, and we find the signal peaks we are looking for, although still obscured by a background.

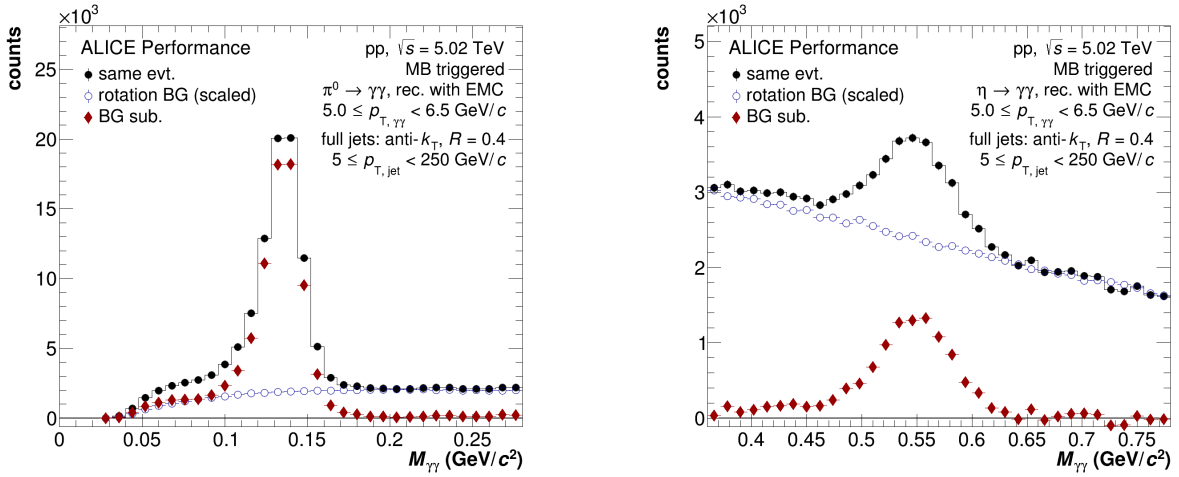

Figure 12: Two snapshots of a single invariant mass distribution (black), the estimated background (blue) and the background-subtracted invariant mass distribution (red). These are focused on the invariant mass regions for the π_0 (left) and the η (right) mesons. These graphs include only photon pairs detected inside full jets with a meson transverse momentum between 5.0 and 6.5 GeV.

4.5.2 Background Estimation

The cause of the combinatorial background obscuring our meson signal is twofold. One stochastic part, originating from the fact that *any* random combination of two photons may yield a m_{inv} equal or similar to that of the π_0 or η meson, simply by chance. Luckily, to all photons not originating from the same decay, m_{inv,π_0} is no more special than any other value. Their values lie along a smooth curve that makes up the bulk of the background. A second contribution to the combinatorial background is partially correlated in nature and is caused primarily by particle decays that produce more than two photons, and jet structures. This part of the background becomes increasingly significant at high transverse momenta, as is the case inside jets. [9]

Traditionally, the shape of the background is estimated using 'event mixing'. Unfortunately, as it uses data from multiple events, this event mixing technique does not account for the partially correlated contribution to the background. A different technique has been developed within the ALICE collaboration, based on [2], known as the

rotation technique. As both techniques are used to some extent for this research, both will be described in detail in this section.

4.5.3 Event Mixing Method

Event mixing is a technique used to create a reference for background noise by combining photons from different collisions. The reasoning behind this method is that photons from separate collisions will never show correlations of particle decay. This allows us to model the random background in the invariant mass spectrum. By pairing photons from different events and calculating their invariant mass (m_{inv}), we can create a smooth distribution that represents the random nature of the background. This distribution serves as a basis for comparison with the actual invariant mass distribution, which includes both the signal of interest and all background elements. The effectiveness of this technique depends on the similarity of the chosen events in terms of overall characteristics such as the number of particles produced and the spatial arrangement of the event.

To implement event mixing, we start by selecting events that have similar general characteristics, such as the number of particles and the spatial layout. Once suitable events have been chosen, we pair the photons from these events using criteria that aim to replicate the random combinations of photons observed in real collision events. We then calculate the invariant mass (m_{inv}) for each pair of photons and compile these values into a distribution. This distribution represents the random background, which we can then compare to the actual data that includes both the signal and all background elements. The accuracy of event mixing depends on the similarity of the selected events and the selection criteria used for pairing the photons. [5]

Considering that this research focuses only on mesons inside jets, and that jets are produced in every direction, the event mixing method has needed to be altered slightly. Before combining the photons from many different events and calculating their invariant mass distribution, we first rotate all events so that the momentum vector of the highest momentum jets points in the same direction for all events. This conserves as much as possible of the directionally dependent correlations inside jets, and prevents the background from representing that of an event where only very high momentum -and for larger opening angles, heavy- particles are produced in all directions. This results in a much more realistic approximation of the background, while not drastically changing the concept of the event mixing method.

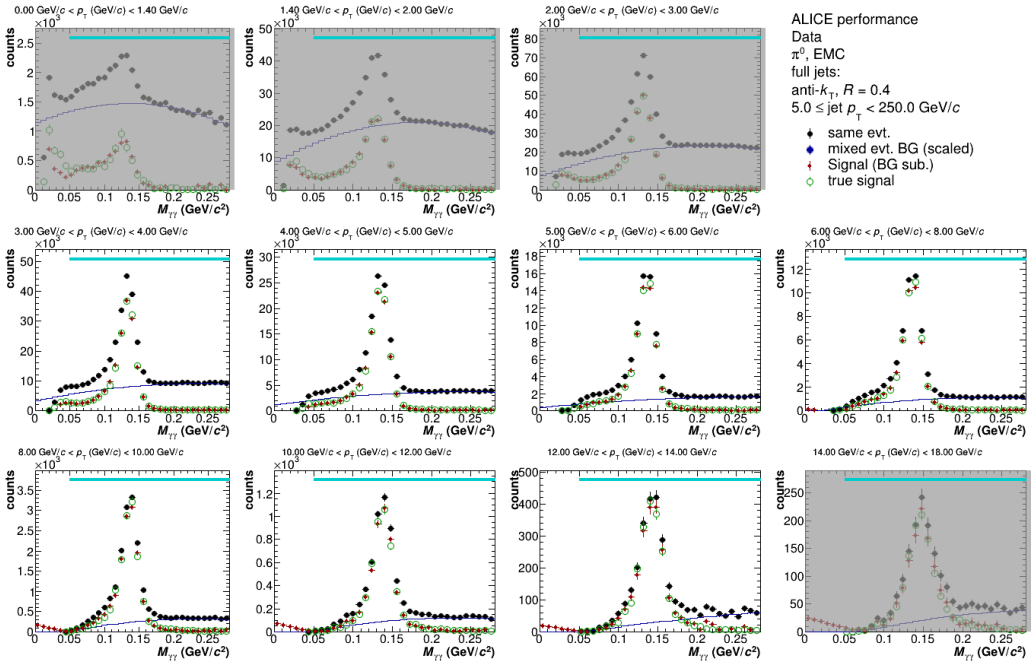

Figure 13: An example showcasing the performance of the mixed event background, showing the signal for the π_0 meson (red) obtained by subtracting the background (blue) from the total invariant mass distribution (black), and the true meson signal (green) determined from MC simulations. Greyed out bins are deemed not fit for the analysis.

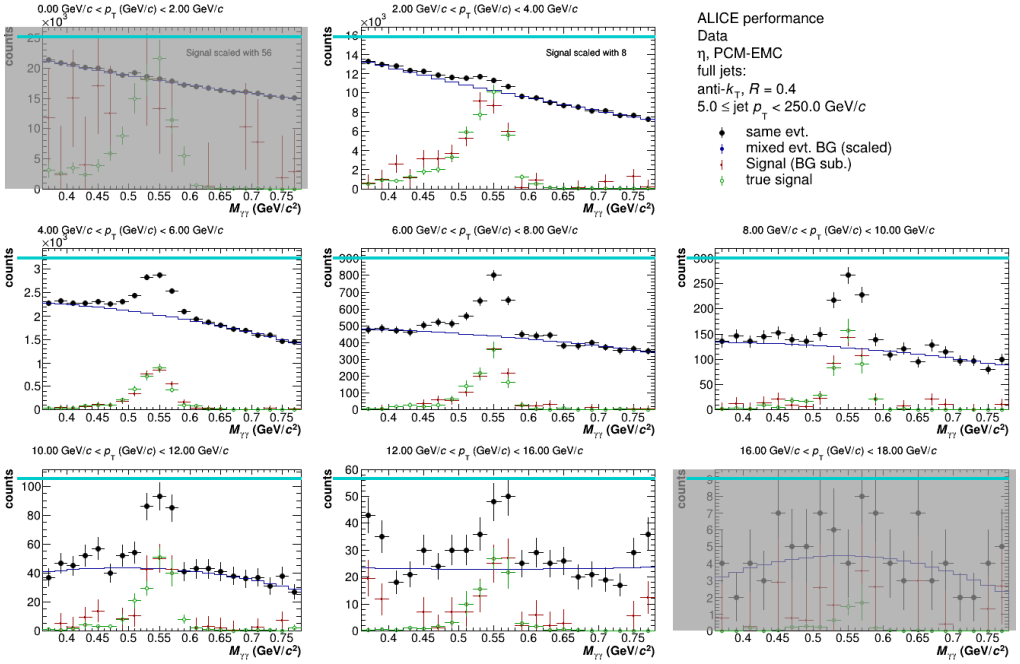

Figure 14: An example showcasing the performance of the mixed event background, showing the signal for the η meson (red) obtained by subtracting the background (blue) from the total invariant mass distribution (black), and the true meson signal (green) determined from MC simulations. Greyed out bins are deemed not fit for the analysis.

4.5.4 Rotational Background

The "rotation technique", on the other hand, uses only photons from a single event, allowing it to include any internally correlated background, such as caused by jets or particles decaying into more than two photons. Therefore, this method should give a more accurate description of the combinatorial background.

The main idea of the rotation technique is to pair two arbitrary photons from the same event, assume that they have originated from a common mother particle, with momentum vector $\vec{p_M}$, equal to the combined momenta of the photons. We then proceed to rotate the momenta of the photons around the momentum vector $\vec{p_M}$, by $\pi/2$, end combine each of the rotated photons with every other photon in the analysis, except for the other rotated photon.

This approach effectively removes the direct correlation between the photons in the background estimation, while leaving the momenta and relative distance of the photn pair unchanged. Because the two rotated photons are not paired with each other, a possible signal from their momenta is cancelled. The correlations with all other photons is cancelled by the rotation of the momentum vector. However, other correlations like those due to jets are preserved, because the substructure of the collision remains largely intact.

The key step in this technique is the rotation of the photon pair around the axis of their pair-momentum vector by 90 degrees. This rotation leaves the momenta and relative distance of the pair unchanged. The rotated photons are included in the pairing process only if they would still be detectable within the acceptance of the employed reconstruction technique. This method is applied to each possible photon pair combination in the event.

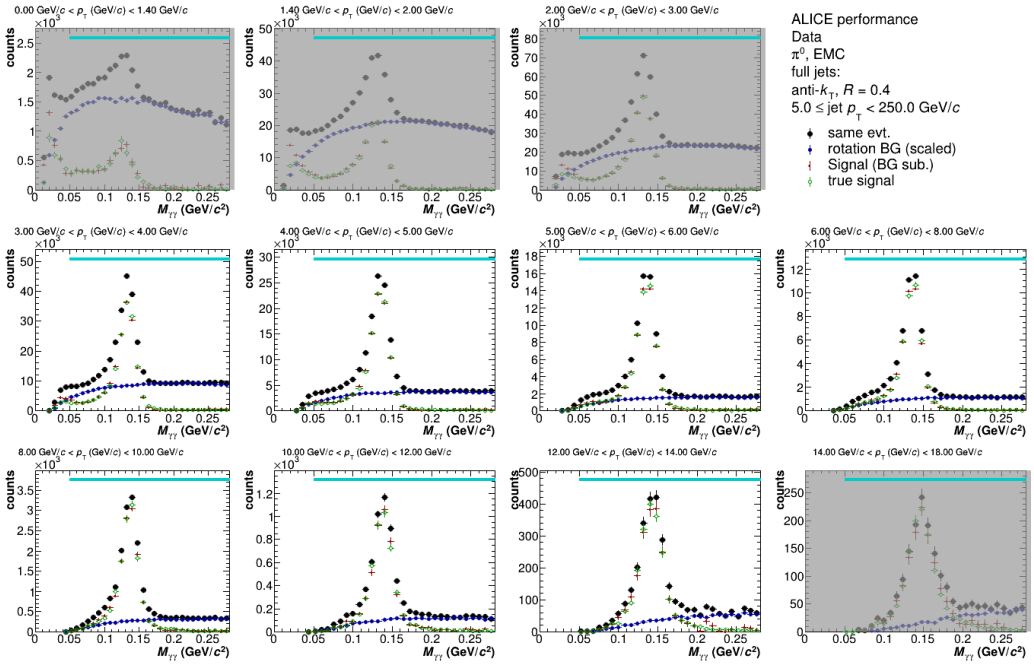

Figure 15: An example showcasing the performance of the rotational background, showing the signal for the π_0 meson (red) obtained by subtracting the background (blue) from the total invariant mass distribution (black), and the true meson signal (green) determined from MC simulations. Greyed out bins are deemed not fit for the analysis.

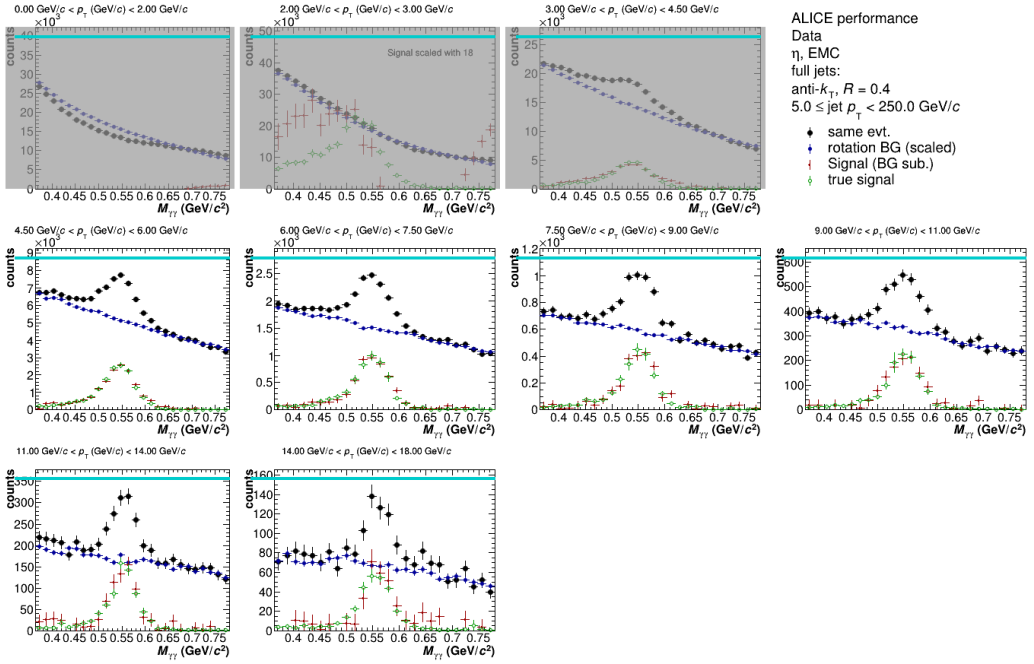

Figure 16: An example showcasing the performance of the rotational background, showing the signal for the η meson (red) obtained by subtracting the background (blue) from the total invariant mass distribution (black), and the true meson signal (green) determined from MC simulations. Greyed out bins are deemed not fit for the analysis.

4.5.5 Fitting and Integration

Having obtained the shape of the background noise, we now have all we need to extract the raw meson yield from the invariant mass distribution. To do this, we subtract the background from the total distribution, but we need to scale it first, because the invariant mass distributions for the signal and background are not normalized, so their amount of entries may differ. This is done using the template method, as opposed to the standard scaling method, which normalizes the background to match a predefined region of the signal. The scaling method approaches this differently by first fitting the signal with a polynomial. The resulting polynomial will yield parameters that describe the signal and parameters that describe the background. Then the parameters that describe the background are used to accurately scale the background. This scaled background is then subtracted from the total distribution, yielding an accurate representation of the raw meson signal. This raw signal is fit with a two-part Gaussian of the form:

$$f(x) = \begin{cases} A\left(\exp\left(-\frac{1}{2}\left(\frac{x-\mu}{\sigma}\right)^2\right) + \exp\left(\frac{x-\mu}{\tau}\right)\left(1 - \exp\left(-\frac{1}{2}\left(\frac{x-\mu}{\sigma}\right)^2\right)\right)\right), & \text{if } x < \mu \\ A\exp\left(-\frac{1}{2}\left(\frac{x-\mu}{\sigma}\right)^2\right), & \text{if } x \geq \mu \end{cases} \tag{11}$$

Where A is the amplitude of the peak, μ is the position of the peak (the meson mass), σ is the standard deviation, from which we will obtain the meson width, and τ is a parameter for the exponential component (only on the left side of the peak) of the gaussian fit which accounts for Brehmstrahlung energy loss for electrons (relevant for PCM) or imperfect photon energy reconstruction due to the finite resolution of the EMCal detector [9].

The best fit of this function to the raw meson signal is then calculated to obtain the meson width and mass, which are used as measures to determine the quality of our analysis. The mean μ is then used to determine the range over which we will integrate the raw meson signal (not the Gaussian). The integration ranges for each method can be seen in table 4. The result of this integration is the raw meson yield.

Detector	$M - M_{\pi^0}$ (GeV/c^2)	$M - M_{\eta}$ (GeV/c^2)
EMC	$[-0.06, +0.05]$	$[-0.06, +0.06]$
PCM	$[-0.04, +0.03]$	$[-0.04, +0.04]$
PCM-EMC	$[-0.04, +0.04]$	$[-0.05, +0.05]$

Table 4: Invariant mass difference ranges for various detectors.

5 Correcting the raw yield

The raw meson yield we have extracted following the methods described in section 4.5.2 is in its current state, not suitable for use in theoretical research or very meaningful in comparison with results from other experiments, present or future. It is in essence, still a count of the amount of mesons that have not only been produced in the collisions, but subsequently decayed into two photons, which interacted with the detector in such a way that the relevant recontruction methods (PCM/EMC) were able to reconstruct them *both* and pass them to our refined, yet imperfect extraction process, where the resulting raw yield will be shifted once more.

From this distorted representation of reality that is the raw meson yield, we want to move to a clear, reproducible value that is independent of the efficiency of the detector, reconstruction method, etc. So that, if this same measurement were to be performed in a different lab, with a different detector and different data processing methods, the same invariant value will be obtained (if both are performed correctly, of course). We will refer to this value as the Invariant Yield. Mathematically, it can be expressed as

$$\left(\frac{1}{2\pi p_T}\frac{d^2N}{dp_T dy}\right), \tag{12}$$

where, p_T is the transverse momentum of the particles relative to the beam axis, the factor $\frac{1}{2\pi p_T}$ normalizes the yield to the transverse momentum and ensures the invariance under rotations in the transverse plane, making the yield independent of the azimuthal angle ϕ $\frac{d^2N}{dp_T dy}$ is the double differential yield of the particles, indicating the number of particles (N) produced per event within a differential element of transverse momentum dp_T and rapidity dy, y is the rapidity, a measure related to the velocity of the particles along the beam direction. It's used instead of the velocity because rapidity differences are invariant under Lorentz transformation along the beam axis, making it a suitable variable for relativistic collisions. The factor $\frac{1}{2\pi p_T}$ normalizes the yield to the transverse momentum and ensures the invariance under rotations in the transverse plane, making the yield independent of the azimuthal angle ϕ.

In this research, we will be presenting most results as function of transverse momentum (p_T), therefore take the derivative of the invariant yield with respect to that transverse momentum, and the expression for the transverse momentum-dependent invariant yield is obtained:

$$\frac{d}{dp_T}\left(\frac{1}{2\pi p_T}\frac{d^2N}{dp_T dy}\right). \tag{13}$$

5.1 The role of Monte Carlo simulations

To obtain the invariant yield from the raw meson yield, some corrections must be applied to account for the aforementioned distortions. To know by how much the raw yield needs to be corrected, we need to know its ratio to the invariant yield. Such a ratio would ideally be calculated by simply dividing the raw yield by the invariant yield. However, that would suggest that to calculate the invariant yield, we would need said invariant yield, which is clearly paradoxical. However there is a way to circumvent this, namely by way of Monte Carlo simulations.

As discussed in section 2.2, Monte Carlo simulations are computational algorithms rooted in statistics that can be used to make approximations of the behaviour of complex systems. For this research, simulated data generated by PYTHIA8 is used. PYTHIA is a scientific code library that is used in particle physics research for the generation of events in high-energy collisions between particles. The physics used to calculate the final states from a few-body hard-scattering to a complex final state is based in a combination of theory and phenomenological models [6]. The final state that is calculated by PYTHIA is then passed through another framework, GEANT4. Which is used to simulate the response of the ALICE detector to this hypothetical final state. The exact process behind this, like for PYTHIA, is beyond the scope of this thesis, but can be studied in their respective documentations. [6][3].

Being computer-generated, the simulated data from PYTHIA8+GEANT4 allows us to extract any information from the collision we need. This solves the problem of obtaining the ratio of raw yield to invariant yield. For each step performed between collision and raw yield, we apply the exact same to the MC data, check how it affects the yield, and use the result to correct the yield obtained from real data.

5.2 Correction Steps

In the rest of this section, all corrections required to move from raw yield to the invariant yield will be discussed. All of them, except for the normalization will use the MC-simulated data. The ones related to the concept of 'unfolding' warrant a more detailed discussion and will be discussed in the next sections. The rest of these corrections

are relatively straightforward, such as the signal extraction efficiency, where the yield is scaled by the ratio (obtained from MC) of yield entering the extraction to the yield that was actually extracted. The secondary correction corrects for neutral mesons that have originated from weak decays such as $K^0_S \rightarrow \pi^0 + \pi^0$, which in the π_0 yield can contribute up to 10% of the total yield [22]. For the η meson the secondary contribution is very small: fractionally, between 0.00001 and 0.002, depending on meson p_T. However, for consistency we perform the secondary correction for both. All thats left then is normalization with regards to the amount of events and jets. The step that we have not discussed yet is the meson (and jet) unfolding, which deserves its own section.

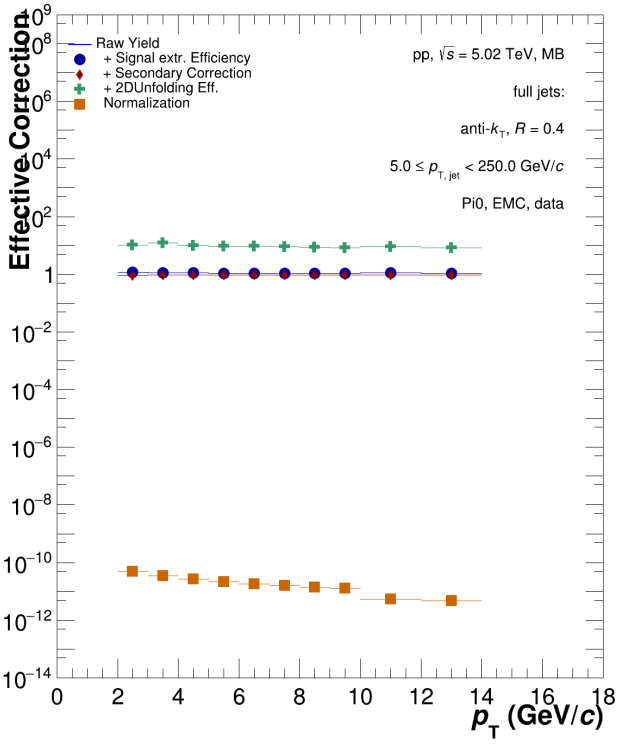

Figure 17: The effective correction for every step in the signal correction process.

5.2.1 Unfolding

After applying the signal extraction efficiency and secondary correction to the raw yield, and before moving on to the meson finding efficiency, we need to perform an operation known as unfolding. When we reconstruct all meson momenta, to achieve a relevant amount of statistics, we will need to divide them into bins. The statistical nature of the uncertainty of this measurement causes some mesons (or jets) with a true p_T that falls in the range of a momentum bin i to be placed in momentum bin $i+1$, $i-1$ or,

statistically, any other bin. The same happens for jets. This is something we should correct for if we want to obtain an accurate in-jet meson invariant yield as function of p_T in the end. This process, determining the true distribution from a convoluted one, is known as unfolding. We represent the reconstructed distribution as a function of true distribution as

$$g(s) = \int_{\Omega} R(s,t) f(t)\, dt$$

where $R(s,t)$ is the response function that describes the probability that a meson or jet with true momentum t is observed as having momentum s. The integral is over the range of possible true momenta, Ω.

The process of unfolding is then the inverse problem where we aim to solve for $f(t)$ given $g(s)$ and $R(s,t)$. Given the finite resolution of our momentum binning, we must also discretize the expression, and it becomes

$$\mathbf{g} = \mathbf{R}\mathbf{f}$$

Now, $\mathbf{g}$ is a vector representing the observed distribution across the bins, $\mathbf{R}$ is now a matrix known as the response matrix, and $\mathbf{f}$ is the vector representing the true momentum distribution we aim to solve for. Fortunately, we can calculate a good approximation of the response matrix using Monte Carlo generated data.

The main goal of the correction discussed in this section is then to perform the matrix multiplication obtaining the corrected distribution for the meson momentum. Since our research has not only divided the meson momentum into bins, but also the jet momentum, and both of them are convoluted. We see the problem at hand when considering that because in this work we are measuring mesons inside jets, the meson momentum needs to not only be corrected for its own finite resolution, but also for that of the jets. If we choose to start with the meson resolution correction, we can express the corrected yield as

$$\mathbf{p}_{T,\text{corr}} = \mathbf{R}\mathbf{p}_{T,\text{uncorr}},$$

where, due to the multiplication with the jet response matrix, the meson p_T distribution is now a function of the reconstructed jet. Afterwards, we would apply a second unfolding for jet resolution. However, this introduces the complexity of unfolding a distribution that has already been unfolded for meson momentum. This leads to inac-

curacies because the first unfolding does not account for the influence of jet resolution on meson momentum.

In this work, we attempt to solve this issue by introducing a method based on [13]. This method addresses the issue described above by employing a "4D" construct - a matrix of response matrices - that allows for a simultaneous correction of both meson and jet momenta, an example of such a matrix is displayed in figure 18. This four-dimensional matrix encapsulates the cross-correlations between jet and meson momenta, allowing for a more accurate reconstruction of the true yield by avoiding the recursive inaccuracies that arise from doing the unfolding sequentially. The procedure is illustrated in figure 19

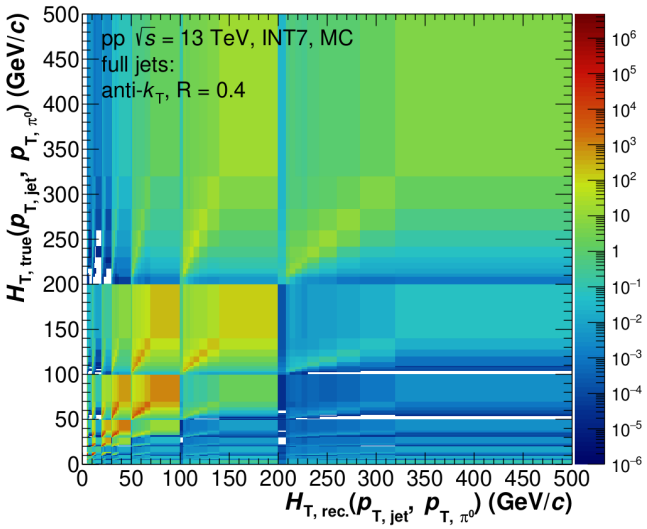

Figure 18: A visual representation of the matrix of matrices used for the 2-dimensional unfolding method. [12]

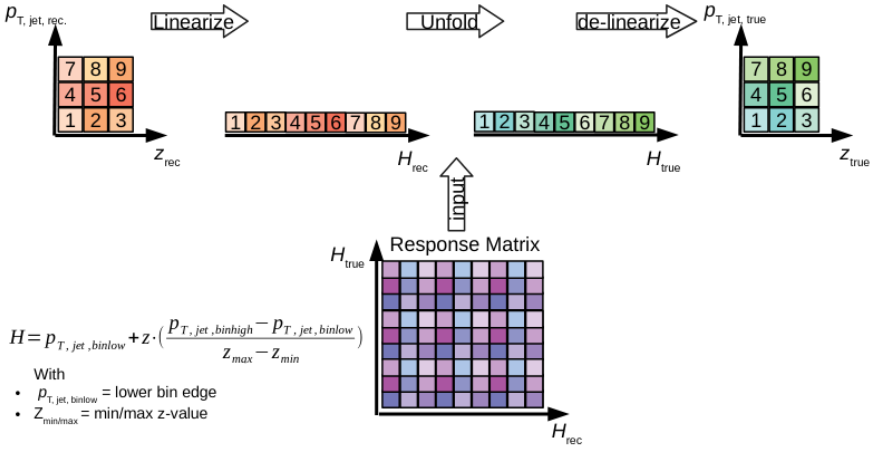

Figure 19: Simplified illustration of the 2-dimensional unfolding process, describing the linearization, unfolding, and subsequent delinearization processes. [12]

6 Systematic Uncertainties

Systematic uncertainties arise in many places within the analysis. To address them we run the analysis many times, each time varying a single variable that could influence the result. By comparing the results of these separate analysis we can calculate the systematic errors of the final result, essentially a measure of its stability. We will divide the variables that have been tested into a few categories, the figures containing the systematic error values obtained from these variations will be included in appendix A.

6.1 Signal Extraction

Parameter	**Variation**
Background fitting	Linear fit, 3rd degree polynomial
Fit template range	Wide: 0.04 to 0.29, Narrow: 0.07 to 0.22
Δ signal integration region	Wide: ± 0.06, Narrow: ± 0.04
Number of Unfolding iterations	3 - 8
Secondary fraction	80%, 120%
Unfolding method	Bin-by-Bin

Table 5: Systematic Uncertainties for Signal Extraction Variations

6.2 Jet Reconstruction

Parameter	**Variation**
Hadronic Correction	minimum ionizing particle energy deposition (MIP)
	F07

Table 6: Systematic Variations in Jet Reconstruction

6.3 Cluster-, Conversion-, & Meson Cut variations

Cluster Cuts		Conversion Cuts	
Parameter	**Variation**	**Parameter**	**Variation**
Max M_{02}	0.4	Min p_T electron	40 MeV
	0.7		50 MeV
	1.0		100 MeV
	$0.5 < M02 < 0.7$	TPC cluster	35%
			70%
Cluster timing	$[-50, 50]$ ns	$Cos(p.a.)$	0.9
	$[-30, 35]$ ns		0.75
	$[-12.5, 13]$ ns	$n_{\sigma e}$	$[-4, 5]$
			$[-2.5, 4]$
Min N cells		$nn_{\sigma\pi}$	$[2, -10]$
			$[0, -10]$
		Pion n_σ min p	0.50 GeV/c
			0.25 GeV/c
		Pion n_σ max p	2.00 GeV/c
$E_{\min}$	0.5 MeV		5.00 GeV/c
	0.6 MeV	Ψ pair	0.1
	0.8 MeV		0.05
Exotic clusters	$F+ < 0.95$	q_T and α 2D	$q_T < 0.110 p_T$
			$q_T < 0.125 p_T$
			$q_T < 0.130 p_T$
			$\alpha < 0.99$
Fiducial Volume	0.4 rad from detector edge		
Meson Cuts			
α cut	$0 - 0.75$		
	$0 - 0.65$		
Opening angle	1 cell dist +0.0152		
	1 cell dist +0.0202		
	1 cell dist +0		

Table 7: Summary of systematic uncertainties for Cluster, Conversion, and Meson Cuts in ALICE experiments, focusing on EMCal and TPC+ITS detectors. M_{02} measures the lateral energy spread in EMCal clusters, critical for photon identification. TPC cluster percentage and cos(p.a.) (cosine of the pointing angle) are key in conversion electron identification, with $n_{\sigma e}$ and $n_{\sigma\pi}$ indicating deviations from expected energy loss for PID. q_T and α parameters, along with Ψ Pair, relate to kinematics of conversion pairs in PCM.

7 Results & Discussion

7.1 Overview

This section will contain the results of this analysis of neutral mesons (π^0 and η) inside jets in pp collisions, the results will be presented in segments, divided by jet momentum ranges and reconstruction methods. As the results will be discussed along with their presentation, a quick overview may be useful.

- **EMC-EMC Full Jets:** We present invariant yields for π^0 and η mesons, noting a clear alignment with preliminary minimum bias measurements for mesons with momenta exceeding the jet momentum threshold. These results highly benefit from the large amount of statistics provided by the EMC-EMC method. We provide the first results of the calculated η/π_0 ratio and use an observation of its limited range in low momentum to introduce the PCM-EMC method.
- **PCM-EMC Full Jets:** By combining PCM and EMC methods, we can go to, and achieve finer resolution at lower meson p_T ranges. Due to the cost of statistics in the choice of adding PCM to the analysis, the results in this section are obtained using the mixed event method for background calculations.
- **Two p_T Bins in Full Jets:** We analyze the results inside full jets in two $p_{T,jet}$ bins and discuss jet-momentum dependency of meson invariant yield. The high momentum jet bin provides a better comparison with preliminary measurements, offering insights into the suppression of the η/π^0 ratio with increasing jet momentum.

To maintain the flow of the narrative, detailed plots of the signal extraction process will be included in the corresponding appendix A, instead of in this main results section.

7.2 EMC, Single Jet-momentum Bin

7.2.1 Neutral mesons p_T-dependent Invariant Yields

The momentum-dependent invariant yields for the $\pi 0$ and η (figure 20) mesons inside full jets EMC-EMC are presented. The meson yields have been reconstructed by combination of the decay photons of the $\pi_0 \to \gamma\gamma$ and $\eta \to \gamma\gamma$ decay modes, respectively,

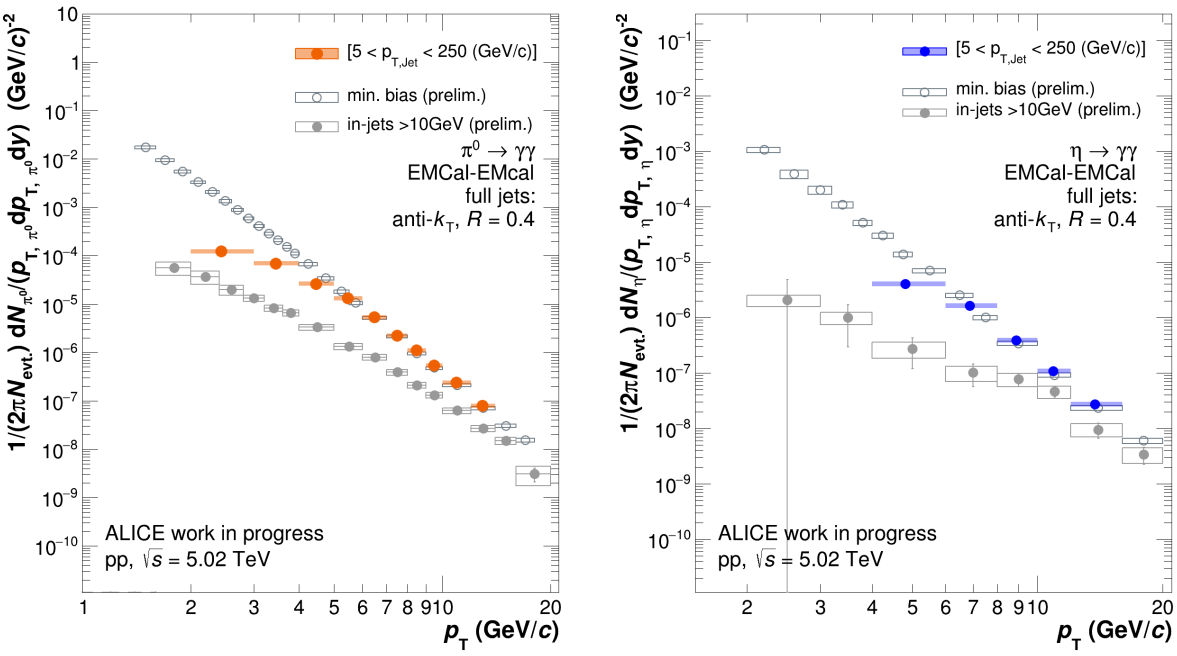

Figure 20: The momentum-dependent invariant yield for the pi_0 (left, orange) and η (right, blue) mesons inside full jets with $p_{T,jet}$ >5GeV. Mesons are reconstructed by combinations of two decay photons, both reconstructed using the ALICE EMCal detector. Preliminary ALICE results providing a minimum bias measurement and an inside charged jets with $p_{T,jet}$ >10GeV are included for comparative purposes.

as described in section 4.5.2 . A sharply falling trend with increasing p_T can be seen for both neutral mesons, which is consistent with theory. In accordance with QCD, which predicts the parton distribution function (PDF) to drop quickly with p_T. Simply; higher momentum mesons cost more energy to produce and are therefore produced less.

A comparison is made to results from an ALICE preliminary measurement performed in 2019, which measured the invariant yield of pi_0 and η mesons inside charged jets with jet $p_T \geq$ 10GeV [22]. A minimum bias (no jet constraint) measurement is provided from the same preliminary.

A clear agreement can be seen between the invariant yield inside full jets and the minimum bias measurement in bins exceeding 5GeV. This is consistent with expectations. As the in-jet mesons are always a subset of the total meson production of the collision, the minimum bias measurement can never be exceeded within the scope of this thesis. The clear agreement in yield above 5GeV is the logical result of our jet momentum threshold of $p_{T,jet} >$ 5Gev. Any meson that carries energy above this threshold will itself be classified as a jet and therefore be included in the in-jet yield,

resulting in congruence with min. bias above this threshold.

Invariant yield for both mesons in bins below the jet momentum threshold can be seen to diverge from the minimum bias measurement with decreasing transverse momentum, indicating that lower p_T mesons are less and less likely to be found inside a jet, a congruent observation to before.

It must be stated clearly that measurements to which the comparison is made are still in preliminary stages. Still, the consistent invariant yield obtained using different analysis methods is appreciated.

Although shown in figure 20 for reference, a comparison to the inside jets is difficult to draw conclusions from in this section of the results. Not only is that measurement done inside charged jets as opposed to full jets, the jet momentum threshold is also higher. Further comparisons will be discussed in section 7.4, where the minimum jet momenta will be aligned.

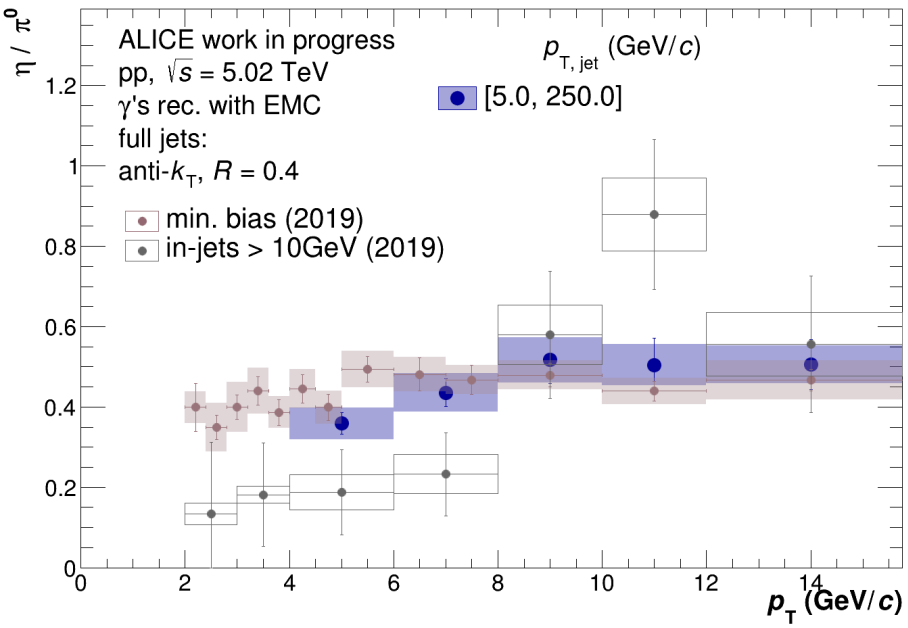

Figure 21: The ratio of η/π_0 yield inside full jets with $p_{T,jet}$ >5GeV. Mesons are reconstructed by combinations of two decay photons, both reconstructed using the ALICE EMCal detector. Preliminary ALICE results providing a minimum bias measurement and an inside charged jets with $p_{T,jet}$ >10GeV are included for comparative purposes.

Figure 21 presents the ratio of η to π_0 yield inside jets with mesons reconstructed by EMC-EMC photon combinations. The previously obtained η yield is used, while to accomodate for bin division, the π_0 analysis is performed again with the binning set to that of the η analysis.

Serving as the most important measurement of this research, the η/π_0 ratio represents the baseline reference for the nuclear modification factor obtained from heavy-ion collisions. Again a good agreement with the minimum bias preliminary measurement can be observed at higher meson transverse momentum.

An important aspect of this analysis is the suppression of the η/π_0 ratio with increasing jet momentum as predicted by Monte Carlo simulations using PYTHIA8, which is a model grounded in perturbative QCD theory, see section 5.1. [4]

Using this knowledge to interpret the results displayed in figure 21, an apparent diverging trend from the minimum bias result towards lower p_T can be observed. Although the statistical and systematic errors must be taken into consideration here and conclusions must be drawn with them in mind. A defensible conclusion is that out measured η/π_0 ratio inside full jets with $p_{T,jet}$ >5GeV, using the EMC-EMC meson reconstruction method at least equal to or lower than the same measurement performed in minimum bias. A large factor in the difficulty experienced to draw conclusions from this result is the lack of bins that are fully below 5GeV. This problem will be less present in the next section, 7.3.1, where the inclusion of a PCM-reconstructed photons will allow for better resolution at low meson p_T.

7.3 PCM-EMC, Single Jet-momentum Bin

7.3.1 Neutral mesons p_T-dependent Invariant Yields

In this section, the results obtained using the PCM-EMC reconstruction method will be presented, where we run an equivalent analysis save for one photon in every pair originating from the PCM. A large part this section will be congruent to section 7.2.1. To avoid a repetitive narrative, the focus will be more on points where these results differ from those obtained using the EMC method.

The Photon Conversion Method, using detectors not dependent on energy deposition in calorimeter cells, but instead reconstructing tracks of charged particles, provides a valuable addition to the indispensable functionality of the EMCal detector. The inclusion of a photon from the Photon Conversion Method (PCM) in our analysis allows us to measure in lower momentum ranges than possible when using only EMCal photons. This is however, at the cost of statistics, due to the restriction to the EMCal acceptance to accomodate the second photon (and measure full jets), and the conversion rate for photons into the necessary e^-e^+ pair being relatively low. In an effort to combat

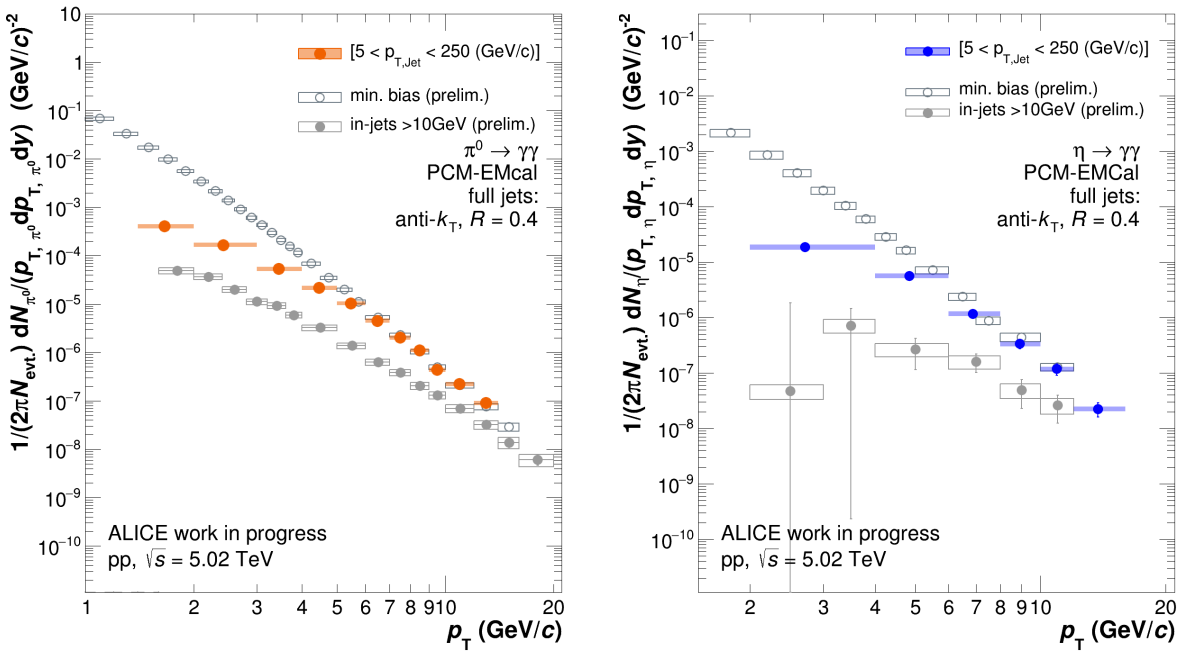

Figure 22: The momentum-dependent invariant yield for the pi_0 (left, orange) and η (right, blue) mesons inside full jets with $p_{T,jet}$ >5GeV. Mesons are reconstructed by combinations of two decay photons, one reconstructed by the EMCal detector and one by the Photon Conversion Method. Preliminary ALICE results providing a minimum bias measurement and an inside charged jets with $p_{T,jet}$ >10GeV are included for comparative purposes.

the low statistics, for this section the decision was made to trade the more accurate background description provided by the rotational method, for the improved statistics the mixed event method provides.

In figure 20 the momentum-dependent invariant yields of the PCM-EMC reconstructed neutral mesons are presented. The difference in momentum range is immediately apparent, especially for the π_0 (orange). Apart from this observation, the conclusions to be drawn from these invariant yields results is very similar to those from the EMC-EMC method. Again, for both mesons, we observe good agreement with minimum bias at higher meson momenta, and divergence below the minimum jet momentum threshold.

Analyzing the η/π_0 ratio obtained using the PCM-EMC method, presented in figure 23, the benefits of the low momentum photon addition from the PCM become readily apparent. A clear distinguishment can now be made between the minimum bias measurement and our result inside jet. The conclusion may safely be drawn that when going towards lower meson p_T, the η/π_0 diverges from the minimum bias and displays

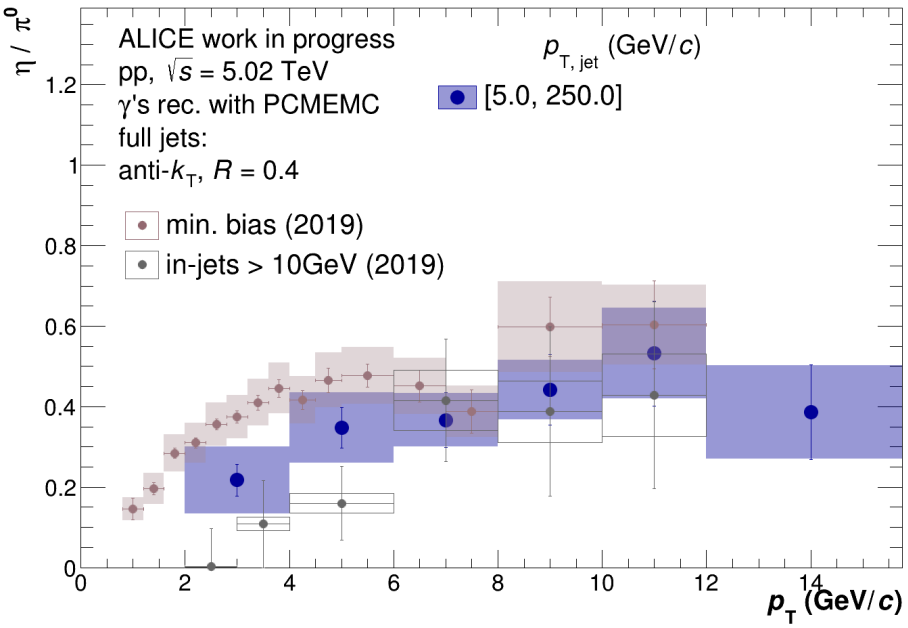

Figure 23: The ratio of η/π_0 yield inside full jets with $p_{T,jet}$ >5GeV (blue). Mesons are reconstructed by combinations of two decay photons, both reconstructed using the ALICE EMCal detector. Preliminary ALICE results providing a minimum bias measurement and an inside charged jets with $p_{T,jet}$ >10GeV are included for comparative purposes.

an eta suppression somewhere in between that of the measurement inside charged jets and minimum bias, fully consistent with Monte Carlo and theory predictions.

7.4 EMC-EMC, Two Jet Momentum Bins

The final result that will be presented in this thesis is from the analysis where the jet momentum is split into two bins, namely $5 < p_{T,jet} < 10$ GeV and $10 < p_{T,jet} < 250$ GeV. Here, we are rewarded with the full benefits of the 2-Dimensional unfolding method described in section 5.2.1. Although it was also applied in results presented in the sections above, the case of the single jet momentum bin reduces this unfolding technique to the traditional efficiency correction.

Dividing the jet momentum in two provides valuable information. A valid comparison can be made at last to the preliminary result in charged jets with momenta exceeding 10GeV. Additionally, it provides insights into the behavior of the η/π_0 ratio near the upper edge of the lower bin, between 8 and 10 GeV meson p_T, where a meson is not only inside a jet, but it essentially *is* the jet.

As may be expected at this point, firstly the momentum-dependent invariant yields of the η and π_0 mesons are presented (see figure 24). From it, many similar conclusions

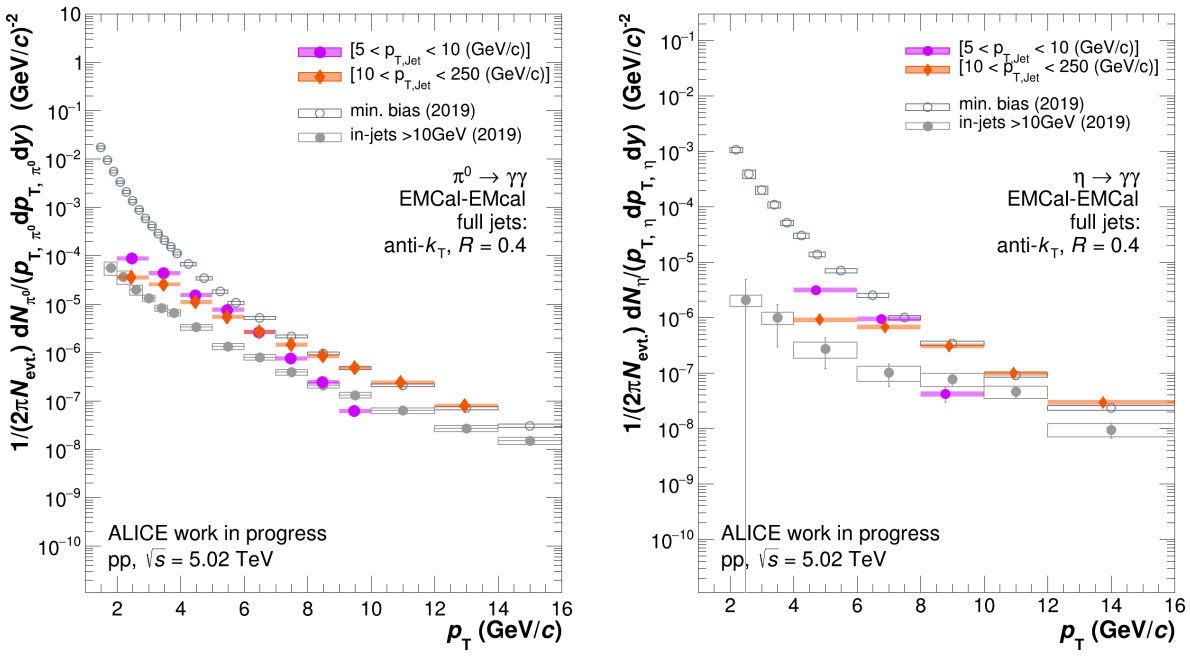

Figure 24: The momentum-dependent invariant yield for the pi_0 (left) and η (right) mesons inside full jets jets divided into 5< $p_{T,jet}$ <10GeV (pink) and 10< $p_{T,jet}$ <250GeV (orange). Mesons are reconstructed by combinations of their decay photons, both reconstructed by the EMCal detector. Preliminary ALICE results providing a minimum bias measurement and an inside charged jets with $p_{T,jet}$ >10GeV are included for comparative purposes.

can be drawn as in the single jet momentum bin case, while also providing some new details. Primarily, we can now do a fair comparison between the preliminary measurement of neutral mesons inside jets and the high momentum jet bin. When doing this visually, we notice still a large discrepancy. This is caused by the nature of the measurement performed. Charged jets are measured only by their charged content. As the particles measured in this analysis carry no charge, this means that the spectrum is shifted. For a 10GeV charged jet to contain a 5GeV neutral meson, its total momentum would be at least those combined. Therefore, should it have been measured as a full jet, it would have a momentum of at least 15GeV. This is likely a large contribution to the shift in yield we observe in figure 24. However, to definitively conclude this, additional measurements are needed.

Additionally, the invariant yield in the lower jet momentum bin can be seen to drop significantly towards the edge of the bin (10GeV), while below 5GeV, it is relatively dominant.

This effect is more visually discernible in figure 25, where for π_0 the ratio to the

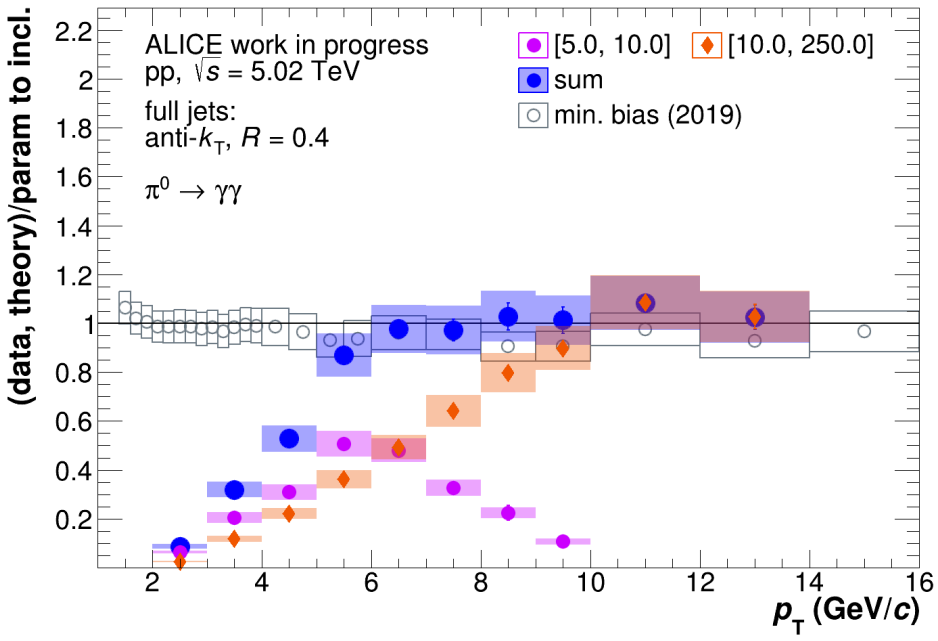

Figure 25: The ratio of the momentum-dependent invariant yield for the π_0 meson inside full jets jets divided into 5< $p_{T,jet}$ <10GeV and 10< $p_{T,jet}$ <250GeV, and their sum (blue). Mesons are reconstructed by combinations of two decay photons, both reconstructed by the EMCal detector. Preliminary ALICE results providing a minimum bias measurement and an inside charged jets with $p_{T,jet}$ >10GeV are included for comparative purposes.

minimum bias measurement is shown. This figure provides valuable information on the distribution of neutral pion yield as a function of jet momentum. We see a clear transition around 6 GeV, where high momentum jets overtake low momentum jets as the dominant source of π_0 mesons. Additionally, from the drop towards the upper edge of the lower jet momentum bin, we learn that a high momentum π_0 is much more likely to be in a high momentum jet, than it is to be the single momentum dominating particle in a jet. This confirms that indeed jets are usually not caused by single high momentum particles, but rather, are collimated streams of many. Or, drawing conclusions strictly from the data this figure provides and nothing else, at least two.

To conclude the results section we will discuss figure 26, which shows the η/π_0 ratio for the two jet momentum bins, and allows for a good comparison between the inside charged jets ALICE preliminary and the inside full jets result presented in this work, for in the ratio of η/π_0, most of this shifted yield from the charged jets result will be cancelled out. Clearly, a good agreement between this result and minimum bias is observed above 10GeV. Beyond that limit, they should - theoretically - be the same measurement, after all. Below that is where more interesting observations lay. We observe an amount of η suppression in the high jet momentum bin landing in between

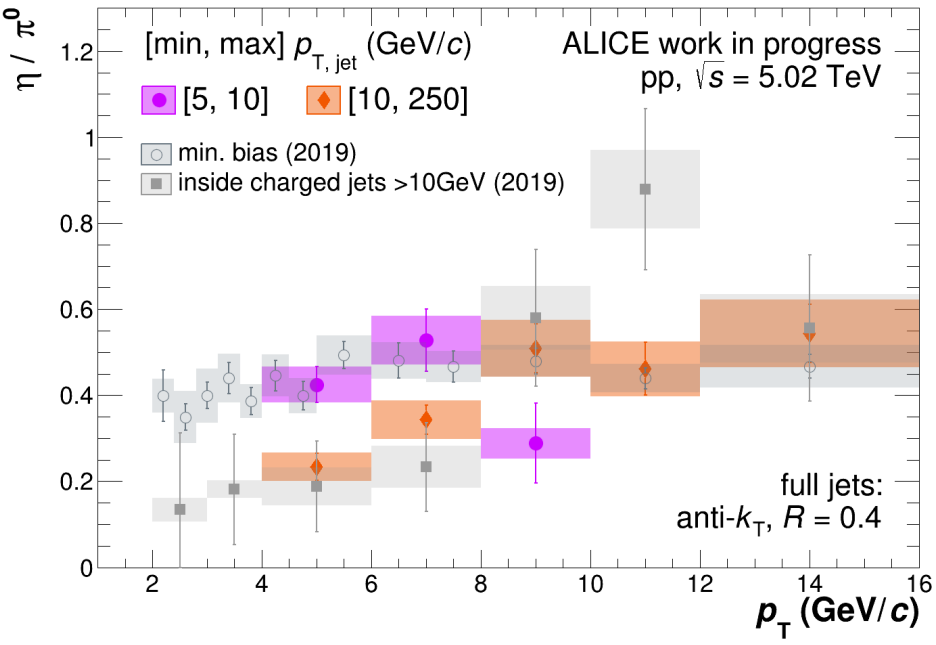

Figure 26: The ratio of η/π_0 yield inside full jets with $p_{T,jet}$ >5GeV (blue). Mesons are reconstructed by combinations of two decay photons, both reconstructed using the ALICE EMCal detector. Preliminary ALICE results providing a minimum bias measurement and an inside charged jets with $p_{T,jet}$ >10GeV are included for comparative purposes.

that of the low jet momentum bin and the charged jet measurement. Again, this can be attributed largely to the missing neutral energy fraction in charged jets, which increases with neutral meson momentum. A jet momentum threshold in charged jets of $p_{T,jet} > 10$GeV, is not equivalent to the same threshold in full jets. The true charged jet threshold should be corrected by a factor > 1, the determination of which is beyond the scope of this thesis, but an interesting topic for future research.

8 Conclusion

In conclusion, this thesis provides a detailed analysis of jet production and the yield of neutral mesons within these jets in proton-proton (pp) collisions, using data from the ALICE experiment at the LHC, specifically the EMCal, ITS and TPC detectors. By examining the momentum-dependent invariant meson yield inside full jets at varying jet momenta, we attempt to contribute to the understanding of meson production inside jets, and thereby, Quantum Chromo Dynamics and the Quark Gluon Plasma.

The results, which include analyses for full jets in single and dual jet momentum bins, reveal a sharply dropping p_T-dependent invariant yield of the neutral mesons π_0 and η consistent with theory. Also demonstrated is the alignment of neutral mesons yield inside full jets with minimum bias measurements for mesons with transverse momenta exceeding that of the jet threshold. Furthermore, the observed divergence from min. bias measurements in neutral meson yields below this threshold suggests a lower likelihood of finding mesons with lower p_T within jets, providing valuable insight into the distribution of mesons in high energy proton-proton collisions.

The inclusion of a photon from the Photon Conversion Method PCM in the filling of the invariant mass distribution, in addition to an EMCal-reconstructed photon extends the analysis to lower momentum ranges, although statistical limitations exist. Nevertheless, this approach allows better resolution in a very important transverse momentum range, , particularly in the η/π^0 ratio, namely the range below the jet momentum threshold, where we look to observe eta suppression as a function of jet momentum. Consistency of this analysis in observing an increased eta suppression with increasing jet momentum confirms the predictions from QCD theory and Monte Carlo simulation in describing this phenomenon

Additionally, dividing jet momentum into two bins has allowed for a valuable, yet inconclusive comparison with previous measurements performed using charged jet reconstruction, underlining the effects arising from fundamental differences in charged - and full jets analysis.

The results obtained in this work demonstrate the effectiveness of the rotational background method in yielding results from jet momentum-restricted data that show good agreement with minimum bias measurements at high meson p_T. However, in cases of low statistics, such as in the case of PCM-EMC, the shape of the background so carefully preserved by the rotation method is lost due to statistical variation in bin content alone, making the mixed event method, with its potentially near-infinite statisics, a more reliable choice in analyzing events with limited photon statistics.

9 Additional Discussion

9.1 Systematics

Due to ongoing data processing on the ALICE grid at the time of this writing, certain analyses related to Meson and Cluster cut variations are not yet complete. As a result, these specific variations have not been included in the results presented. This limitation is recognized, and it is important to mention that these analyses could be integrated into our study in the future, should there be further interest or demand. Including these systematic error variations would improve the quality of the measurement and thereby the conclusions that can be drawn from it.

9.2 Event mixing over Rotational Background in low statistics

During this thesis, considerable focus was laid on the methodology used for background subtraction, specifically by implementing an alternative method to the traditional event mixing, namely the rotational background. The rotational background is very elegant and has proven by generating the EMC-EMC results in this thesis that it is a viable method to perform the background calculation for an analysis such as the one in this work.

In cases of very low statistics, however, the carefully reconstructed shape of the background is lost due to statistical variations in bin content. Because of this, and the low statistics found in the PCM-EMC method, the decision was made to present the PCM-EMC results that were obtained using the event mixing method. Figures 28 and 27 are included to motivate the decision. They illustrate clearly why event mixing may be preferable in cases of low statistics.

9.3 Charged Jets

In addition to studying full jets, we also ran this analysis on charged jets in order to gain a more complete understanding of jet dynamics in pp collisions. However, the results from the analysis of charged jets deviated from theoretical predictions. The yields of charged jets were unexpectedly higher than those observed in minimum bias scenarios. Clearly, this is not physical. Time limitations have not allowed for further investigation into this issue. It may be related to the way in which the corrections are applied, and

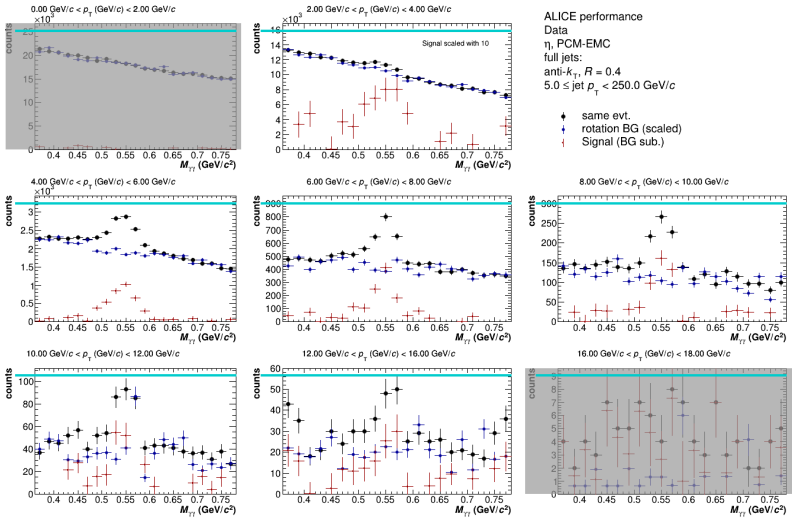

Figure 27: Background fit using the rotational method in low-statistics data, highlighting potential inaccuracies in background shape determination.

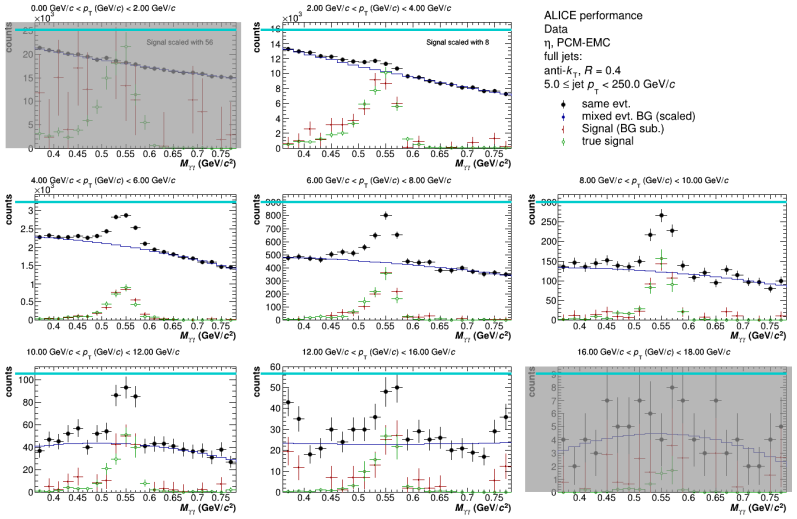

Figure 28: Background fit with the event mixing method, showcasing its effectiveness and reliability in low-statistics scenarios.

is an interesting topic to look into, especially given the full jets results seem to agree quite well with the preliminary results in minimum bias.

9.4 More Jet momentum bins

Although using the 2-dimensional unfolding method discussed - though not originating from - this thesis, its true potential lies in the analyses with a higher number of jet momentum bins. This is also where potential errors would need to be checked. Having gone up only to two jet momentum bins, there was some, but no results-altering difference in using the 2-dimensional unfolding method as oppposed to the tradtional

efficiency correction. In the current state of the research, statistics are simply too low to go to a higher number of jet momentum bins and use the results to draw any valid conclusions. However, should the future provide means to perform the analysis with higher statistics, and more jet momentum bins be a possibility, the results presented in this thesis - having used the 2-dimensional unfolding also in the singular jet momentum bin for consistency - will remain relevant.

A Systematic Uncertainty Plots

A.1 Single Jet Momentum Bin: EMC-EMC

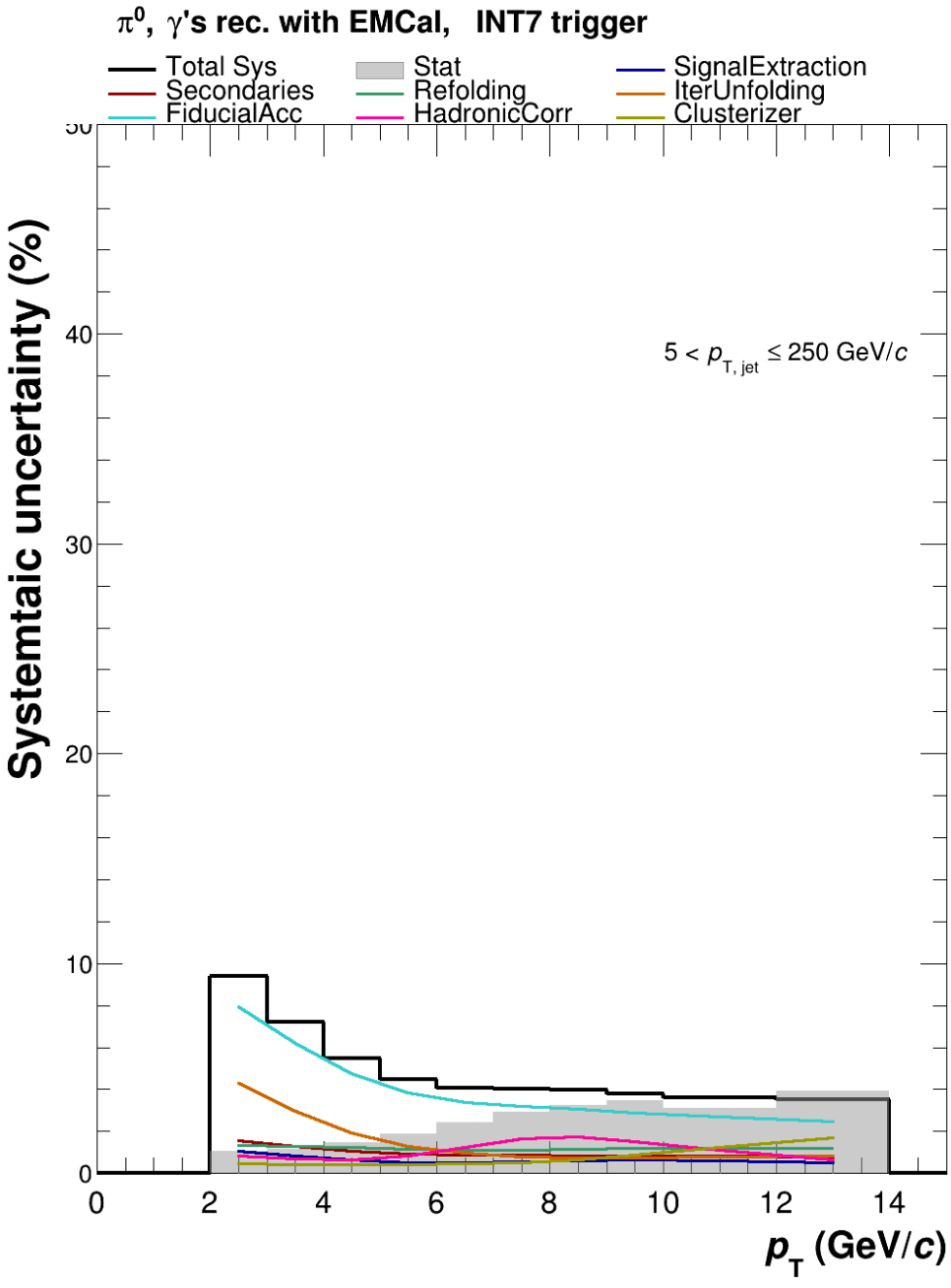

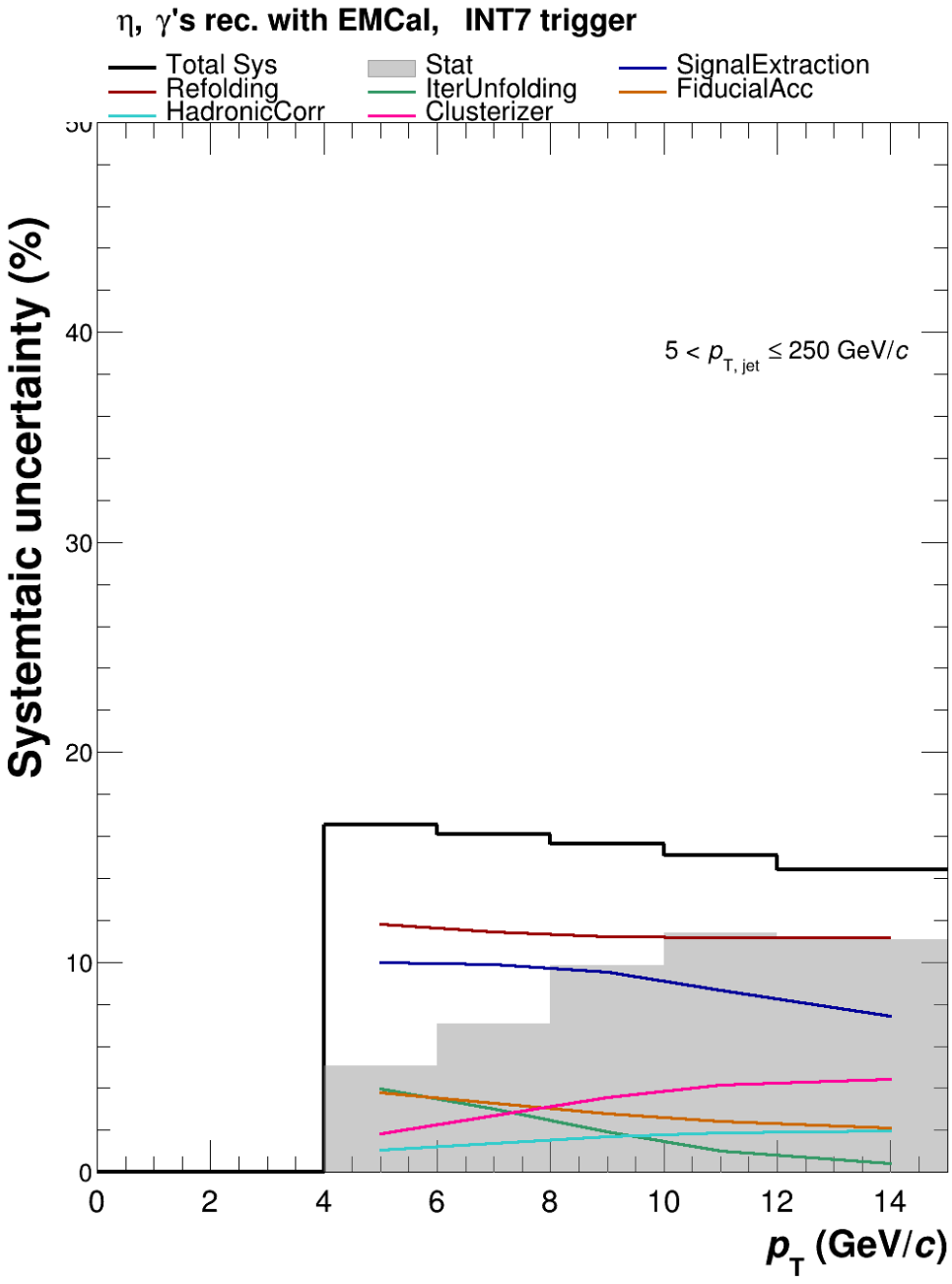
η, γ's rec. with EMCal, INT7 trigger
Total Sys
Stat
SignalExtraction
Refolding
IterUnfolding
FiducialAcc
HadronicCorr
Clusterizer
5 < $p_{T, jet}$ ≤ 250 GeV/c
Systemtaic uncertainty (%)
p_T (GeV/c)
0
10
20
30
40
0
2
4
6
8
10
12
14

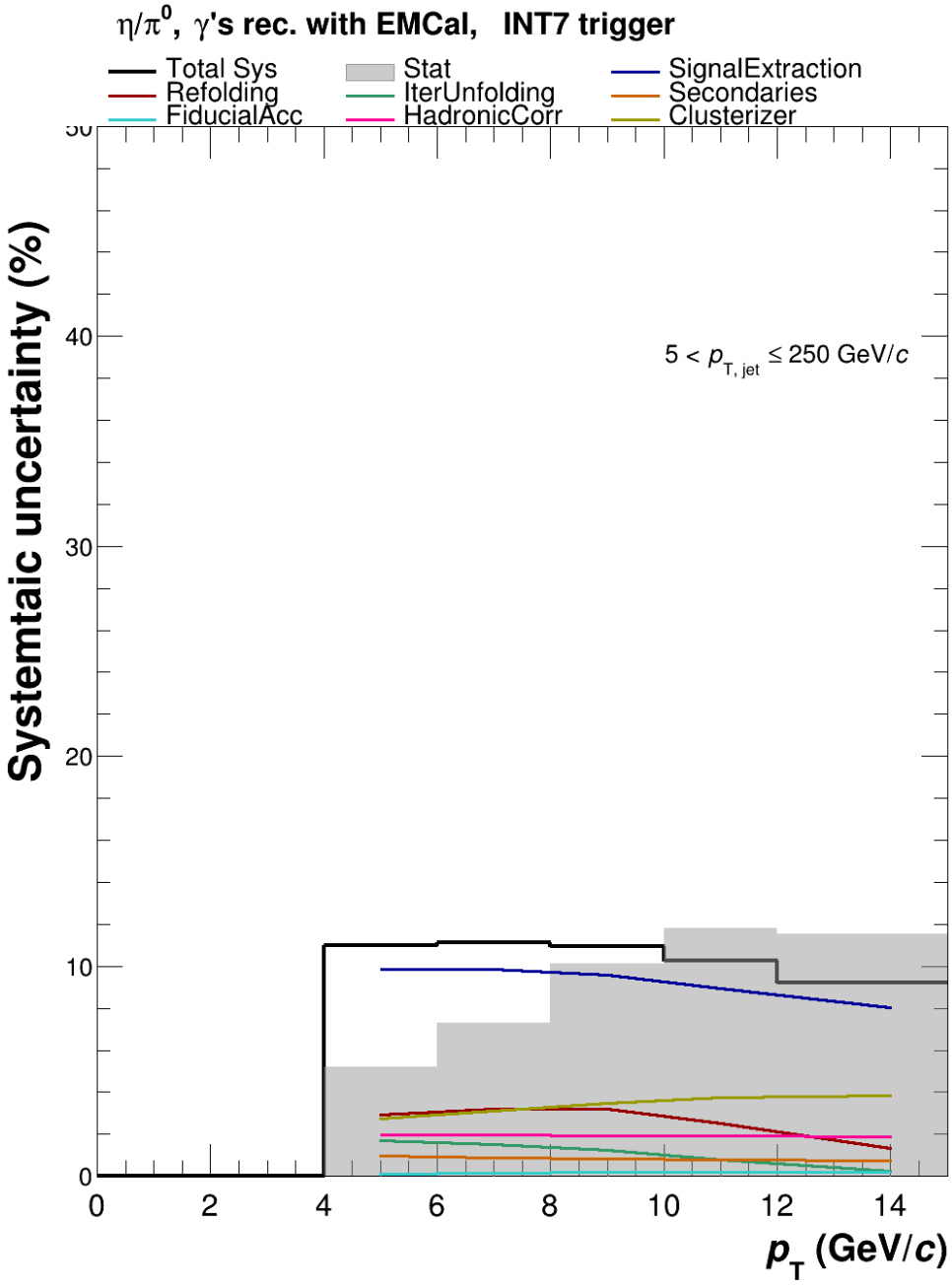
η/π⁰, γ's rec. with EMCal, INT7 trigger
Total Sys
Stat
SignalExtraction
Refolding
IterUnfolding
Secondaries
FiducialAcc
HadronicCorr
Clusterizer
Systemtaic uncertainty (%)
5 < p_T, jet ≤ 250 GeV/c
p_T (GeV/c)
0
10
20
30
40
0
2
4
6
8
10
12
14

A.2 Single Jet Momentum Bin: PCM-EMC

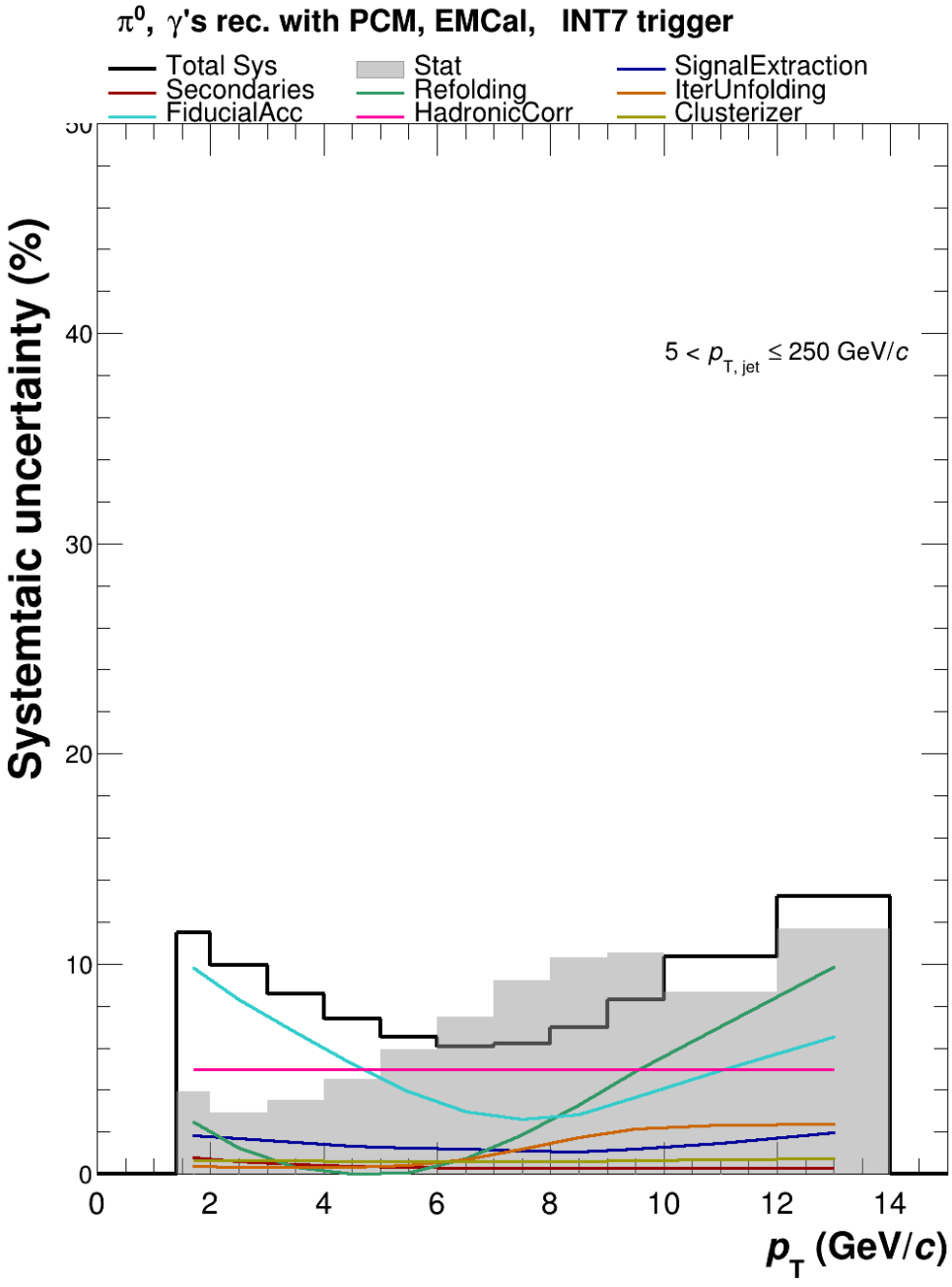

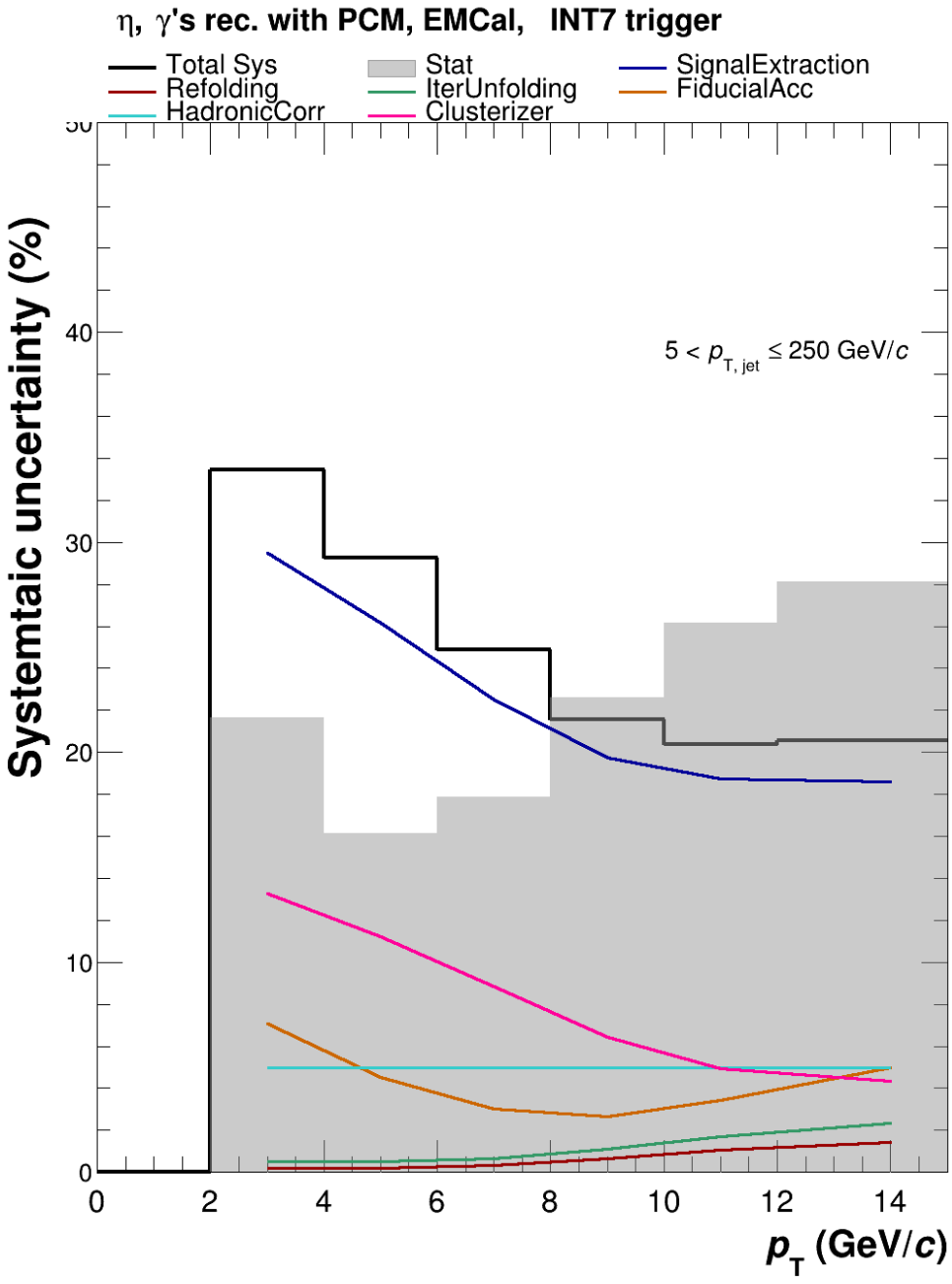
η, γ's rec. with PCM, EMCal, INT7 trigger
Total Sys
Refolding
HadronicCorr
Stat
IterUnfolding
Clusterizer
SignalExtraction
FiducialAcc
5 < $p_{T, jet}$ ≤ 250 GeV/c
Systemtaic uncertainty (%)
p_T (GeV/c)
0
10
20
30
40
0
2
4
6
8
10
12
14

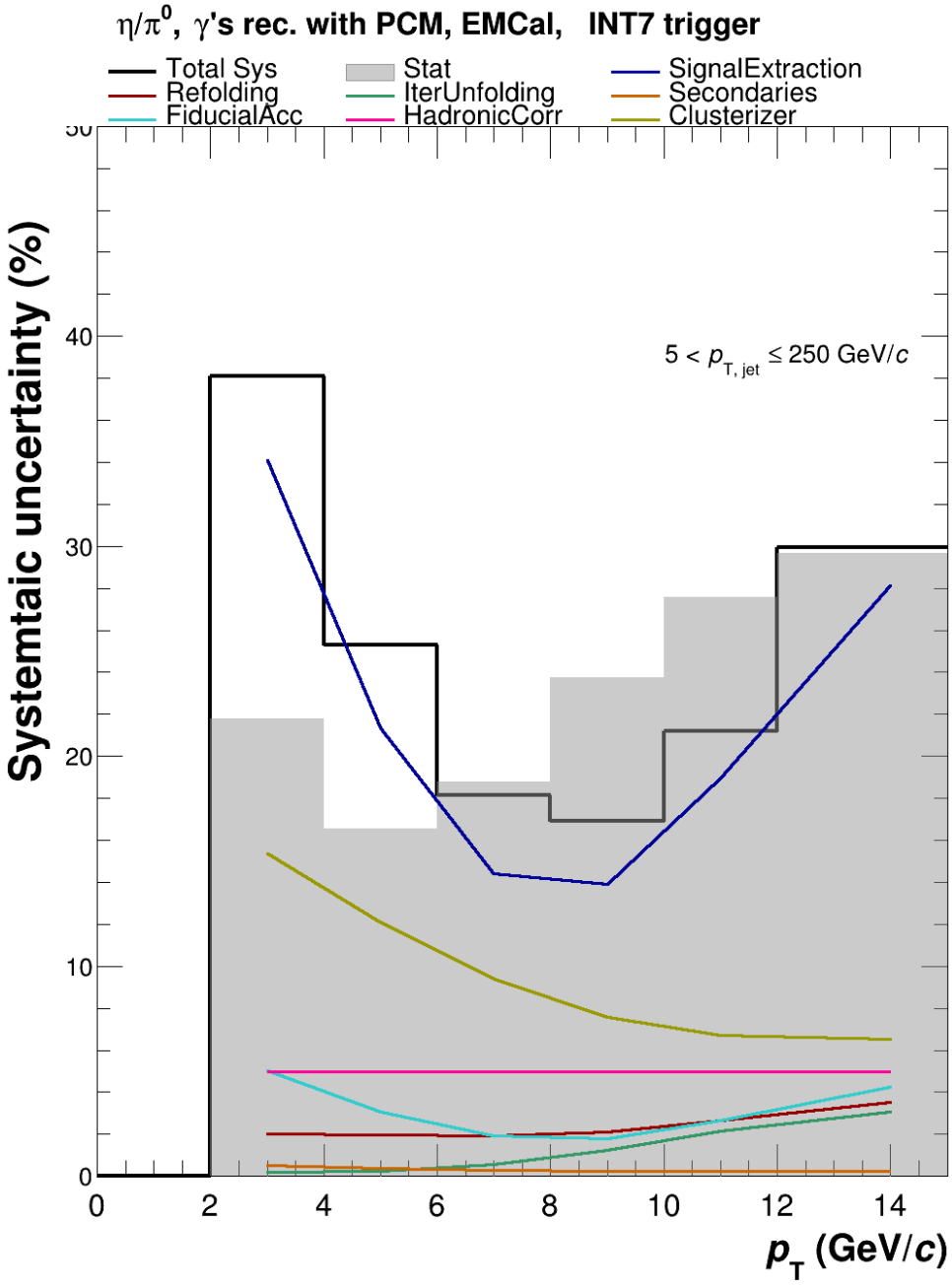
η/π⁰, γ's rec. with PCM, EMCal, INT7 trigger
Total Sys
Stat
SignalExtraction
Refolding
IterUnfolding
Secondaries
FiducialAcc
HadronicCorr
Clusterizer
5 < p_T, jet ≤ 250 GeV/c
Systemtaic uncertainty (%)
p_T (GeV/c)
0
10
20
30
40
0
2
4
6
8
10
12
14

A.3 Dual Jet Momentum Bins: PCM-EMC

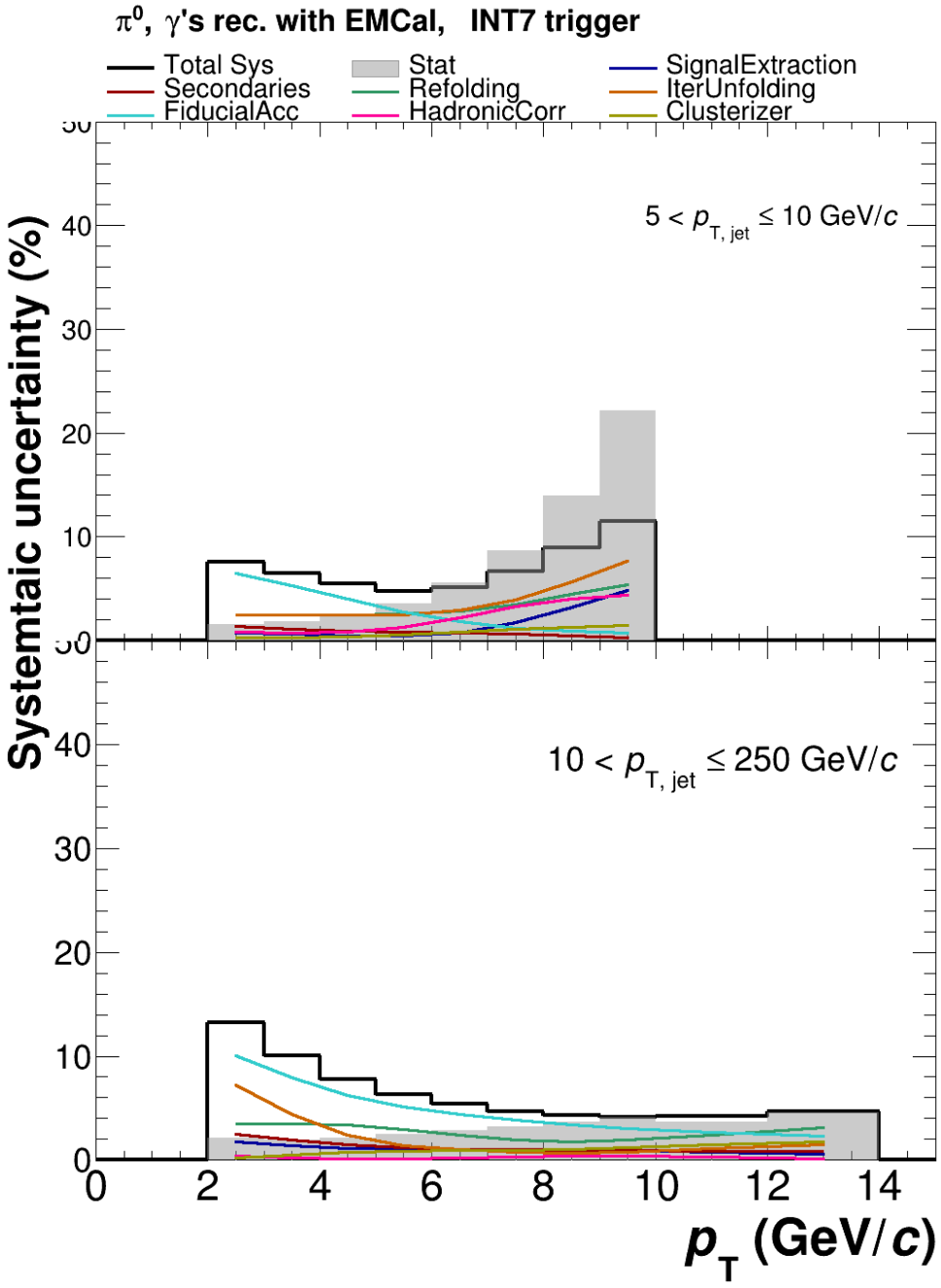

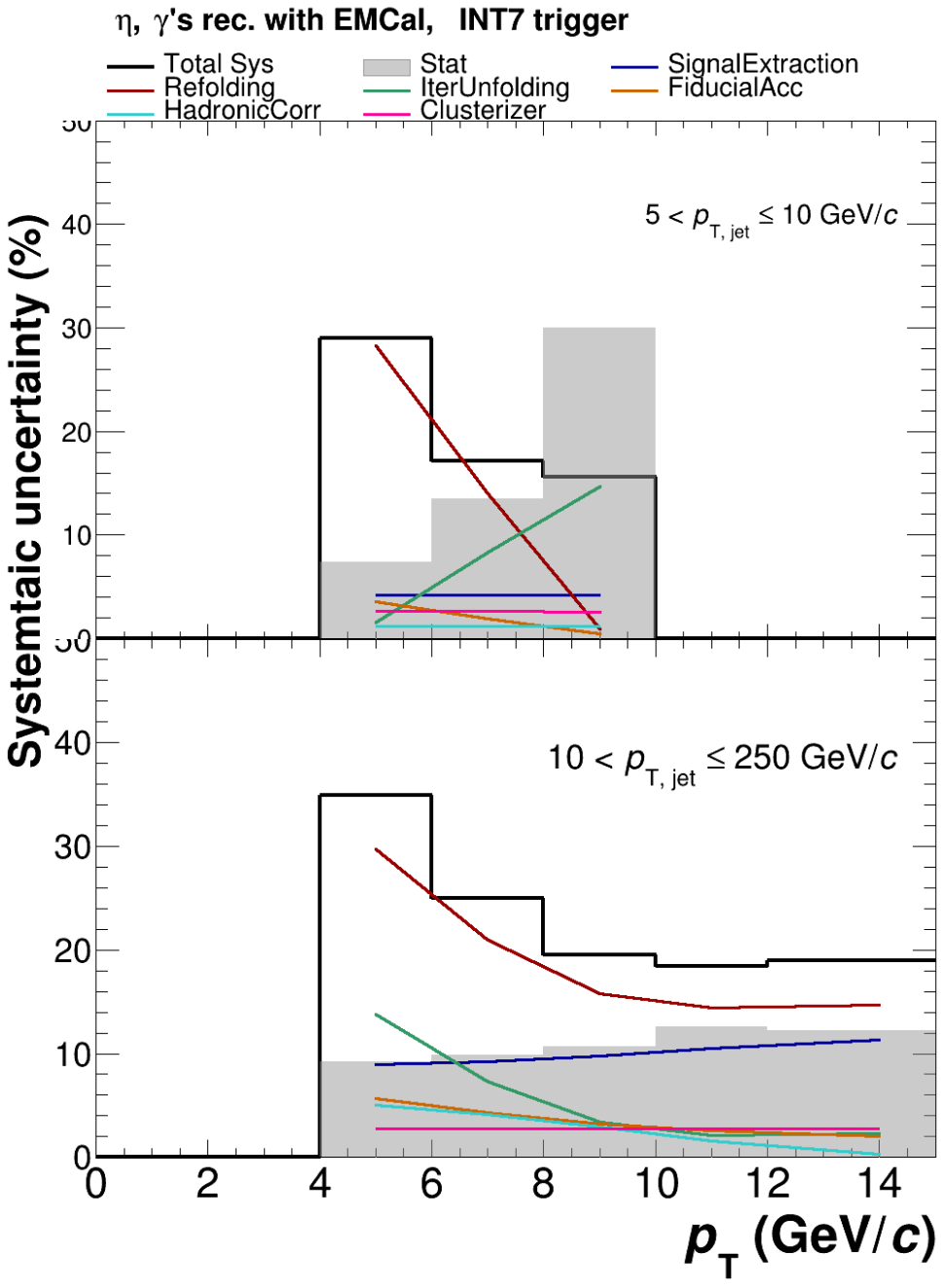
η, γ's rec. with EMCal, INT7 trigger
Total Sys
Refolding
HadronicCorr
Stat
IterUnfolding
Clusterizer
SignalExtraction
FiducialAcc
5 < p_T, jet ≤ 10 GeV/c
10 < p_T, jet ≤ 250 GeV/c
Systemtaic uncertainty (%)
p_T (GeV/c)

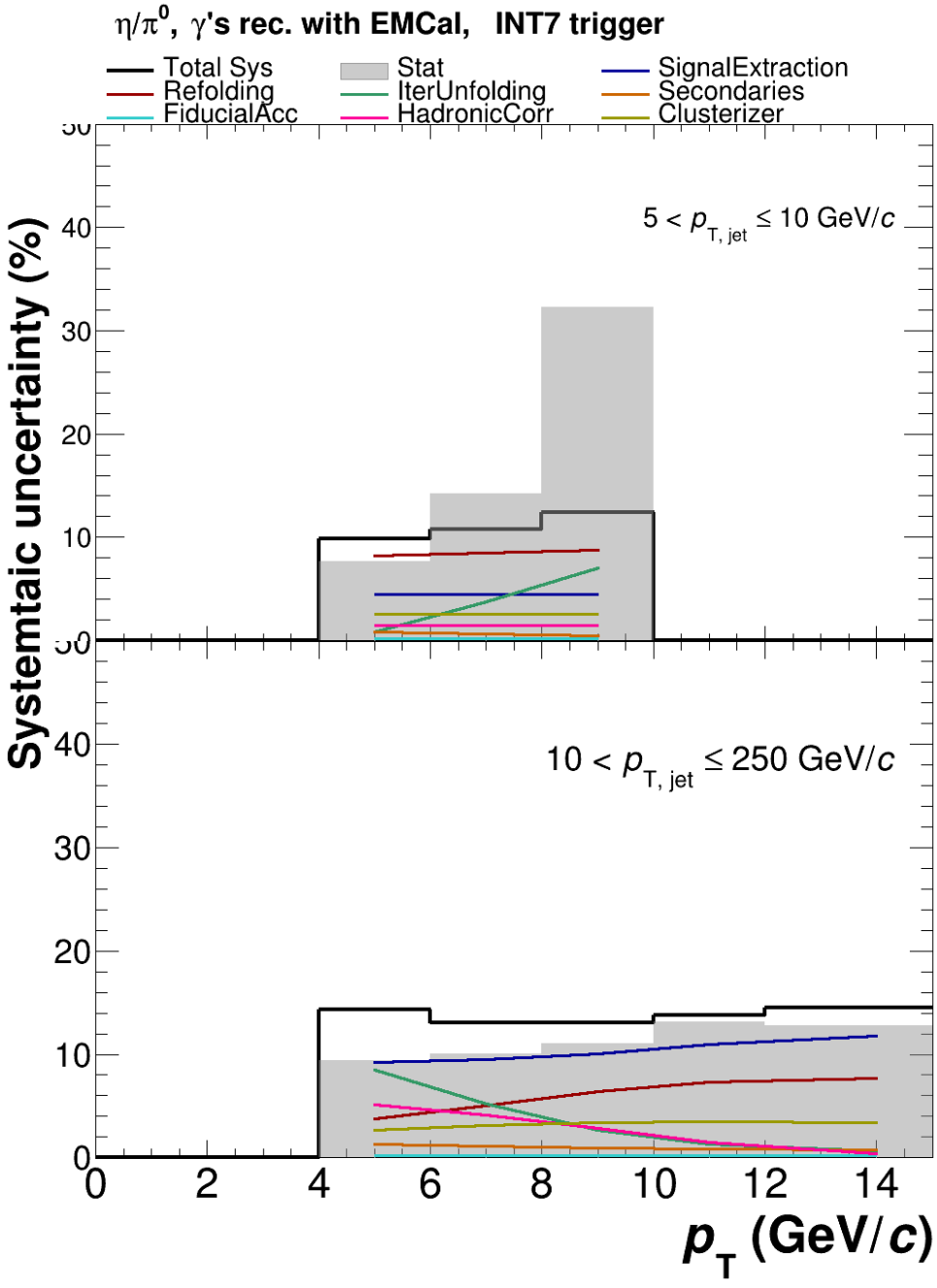
η/π⁰, γ's rec. with EMCal, INT7 trigger
Total Sys
Stat
SignalExtraction
Refolding
IterUnfolding
Secondaries
FiducialAcc
HadronicCorr
Clusterizer
Systemtaic uncertainty (%)
5 < p_T, jet ≤ 10 GeV/c
10 < p_T, jet ≤ 250 GeV/c
p_T (GeV/c)

A Signal Extraction Plots

A.1 Single Jet Momentum Bin: EMC-EMC

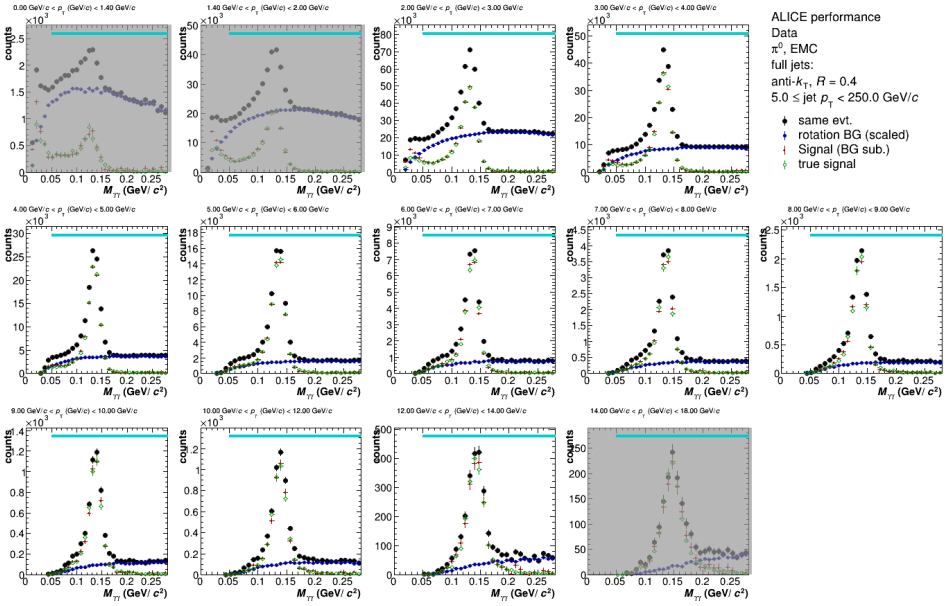

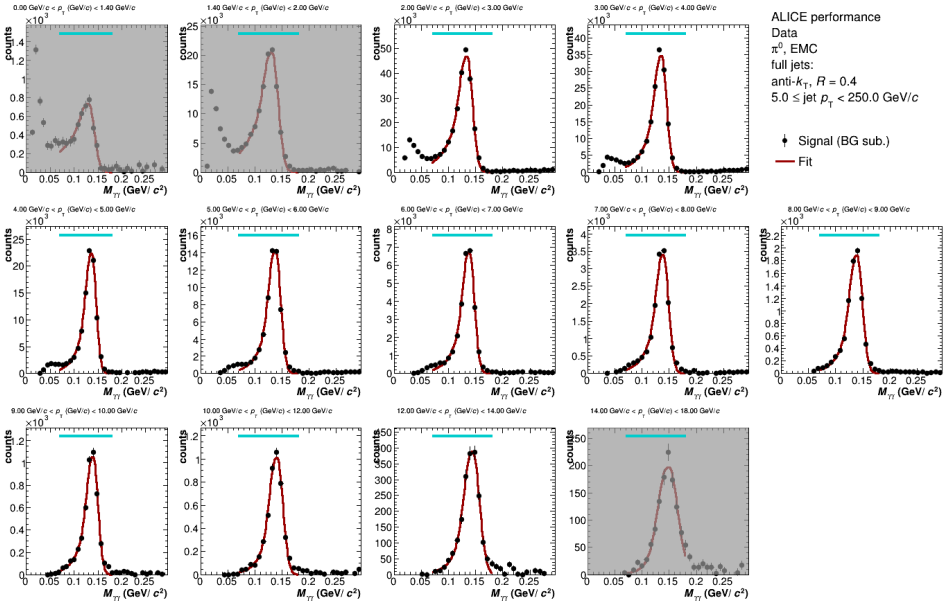

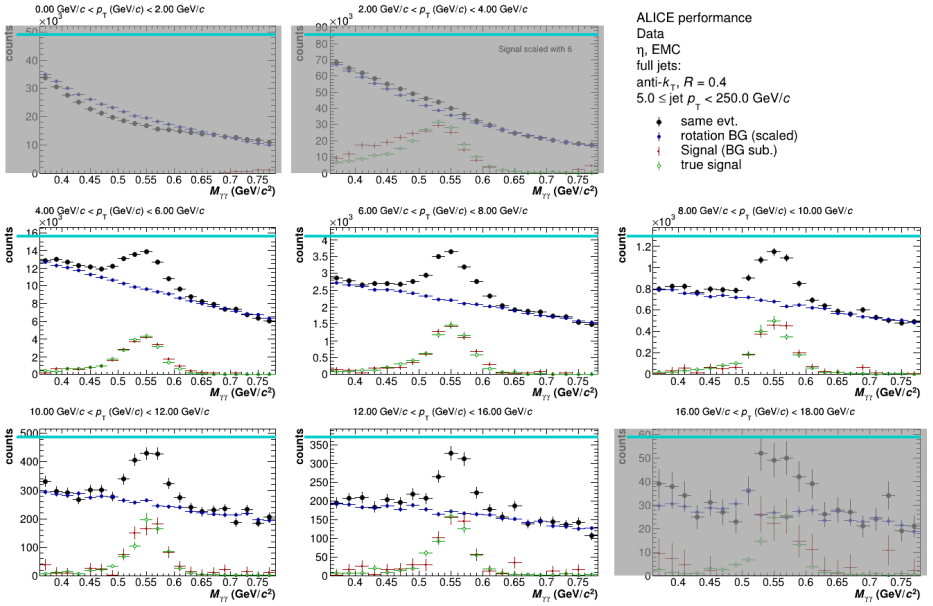
0.00 GeV/c < p_T (GeV/c) < 2.00 GeV/c
2.00 GeV/c < p_T (GeV/c) < 4.00 GeV/c
Signal scaled with 6
4.00 GeV/c < p_T (GeV/c) < 6.00 GeV/c
6.00 GeV/c < p_T (GeV/c) < 8.00 GeV/c
8.00 GeV/c < p_T (GeV/c) < 10.00 GeV/c
10.00 GeV/c < p_T (GeV/c) < 12.00 GeV/c
12.00 GeV/c < p_T (GeV/c) < 16.00 GeV/c
16.00 GeV/c < p_T (GeV/c) < 18.00 GeV/c
counts
$M_{\gamma\gamma}$ (GeV/c^2)
ALICE performance
Data
η, EMC
full jets:
anti-k_T, R = 0.4
5.0 ≤ jet p_T < 250.0 GeV/c
same evt.
rotation BG (scaled)
Signal (BG sub.)
true signal

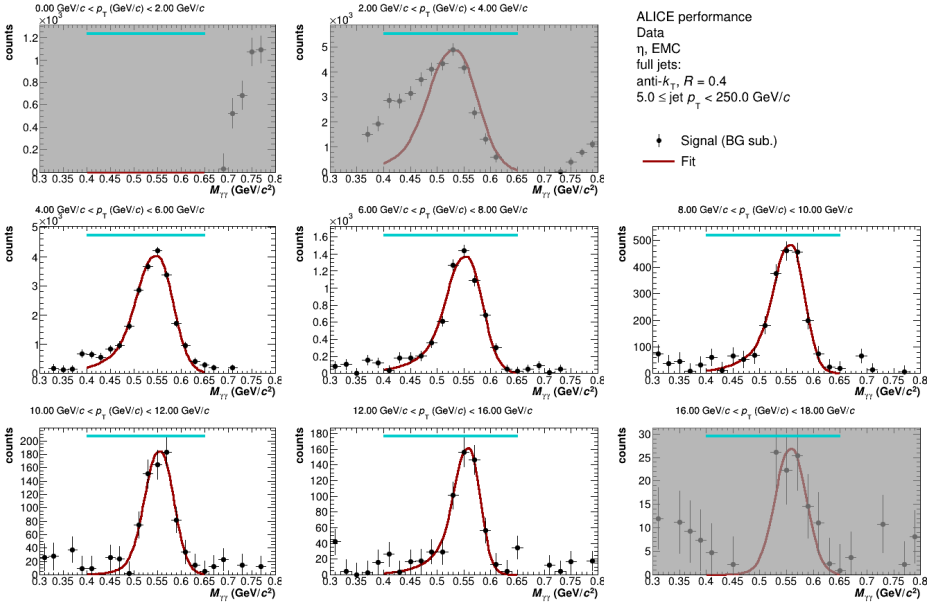
0.00 GeV/c < p_T (GeV/c) < 2.00 GeV/c
2.00 GeV/c < p_T (GeV/c) < 4.00 GeV/c
4.00 GeV/c < p_T (GeV/c) < 6.00 GeV/c
6.00 GeV/c < p_T (GeV/c) < 8.00 GeV/c
8.00 GeV/c < p_T (GeV/c) < 10.00 GeV/c
10.00 GeV/c < p_T (GeV/c) < 12.00 GeV/c
12.00 GeV/c < p_T (GeV/c) < 16.00 GeV/c
16.00 GeV/c < p_T (GeV/c) < 18.00 GeV/c
counts
$M_{\gamma\gamma}$ (GeV/c^2)
ALICE performance
Data
η, EMC
full jets:
anti-k_T, R = 0.4
5.0 ≤ jet p_T < 250.0 GeV/c
Signal (BG sub.)
Fit

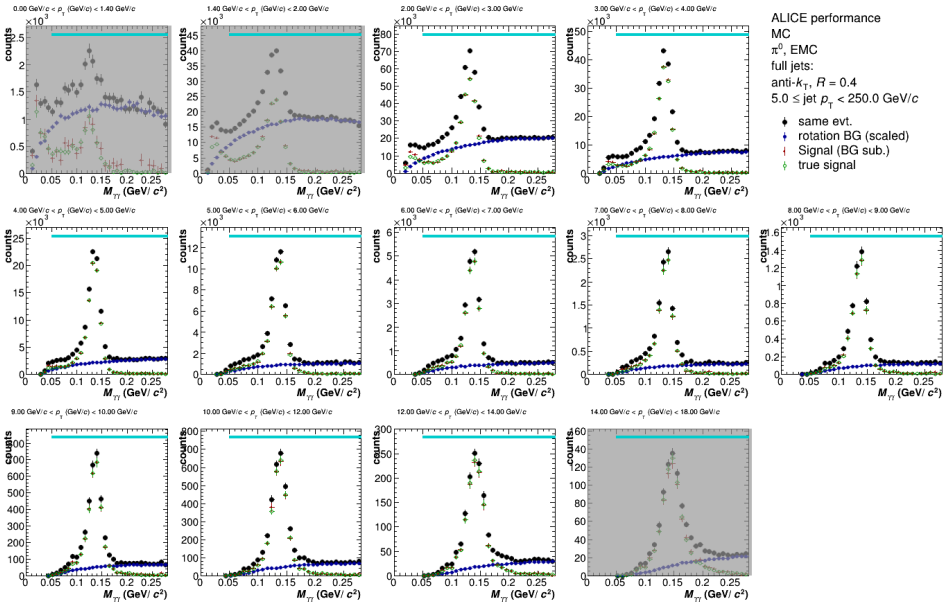
0.00 GeV/c < p_T (GeV/c) < 1.40 GeV/c
1.40 GeV/c < p_T (GeV/c) < 2.00 GeV/c
2.00 GeV/c < p_T (GeV/c) < 3.00 GeV/c
3.00 GeV/c < p_T (GeV/c) < 4.00 GeV/c
4.00 GeV/c < p_T (GeV/c) < 5.00 GeV/c
5.00 GeV/c < p_T (GeV/c) < 6.00 GeV/c
6.00 GeV/c < p_T (GeV/c) < 7.00 GeV/c
7.00 GeV/c < p_T (GeV/c) < 8.00 GeV/c
8.00 GeV/c < p_T (GeV/c) < 9.00 GeV/c
9.00 GeV/c < p_T (GeV/c) < 10.00 GeV/c
10.00 GeV/c < p_T (GeV/c) < 12.00 GeV/c
12.00 GeV/c < p_T (GeV/c) < 14.00 GeV/c
14.00 GeV/c < p_T (GeV/c) < 18.00 GeV/c
counts
$M_{\gamma\gamma}$ (GeV/ c^2)
ALICE performance
MC
π^0, EMC
full jets:
anti-k_T, R = 0.4
5.0 ≤ jet p_T < 250.0 GeV/c
same evt.
rotation BG (scaled)
Signal (BG sub.)
true signal

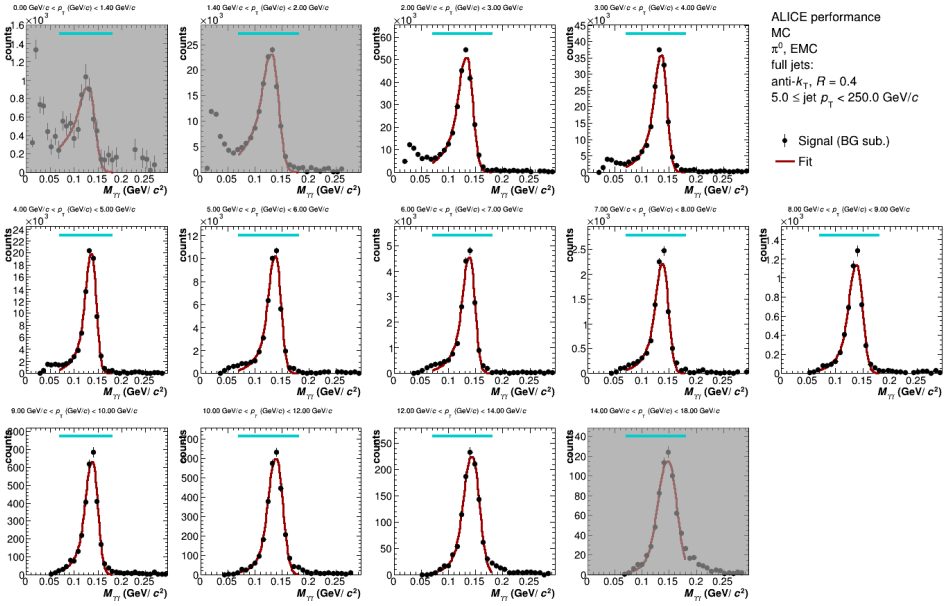
0.00 GeV/c < p_T (GeV/c) < 1.40 GeV/c
1.40 GeV/c < p_T (GeV/c) < 2.00 GeV/c
2.00 GeV/c < p_T (GeV/c) < 3.00 GeV/c
3.00 GeV/c < p_T (GeV/c) < 4.00 GeV/c
4.00 GeV/c < p_T (GeV/c) < 5.00 GeV/c
5.00 GeV/c < p_T (GeV/c) < 6.00 GeV/c
6.00 GeV/c < p_T (GeV/c) < 7.00 GeV/c
7.00 GeV/c < p_T (GeV/c) < 8.00 GeV/c
8.00 GeV/c < p_T (GeV/c) < 9.00 GeV/c
9.00 GeV/c < p_T (GeV/c) < 10.00 GeV/c
10.00 GeV/c < p_T (GeV/c) < 12.00 GeV/c
12.00 GeV/c < p_T (GeV/c) < 14.00 GeV/c
14.00 GeV/c < p_T (GeV/c) < 18.00 GeV/c
counts
$M_{\gamma\gamma}$ (GeV/ c^2)
ALICE performance
MC
π^0, EMC
full jets:
anti-k_T, R = 0.4
5.0 ≤ jet p_T < 250.0 GeV/c
Signal (BG sub.)
Fit

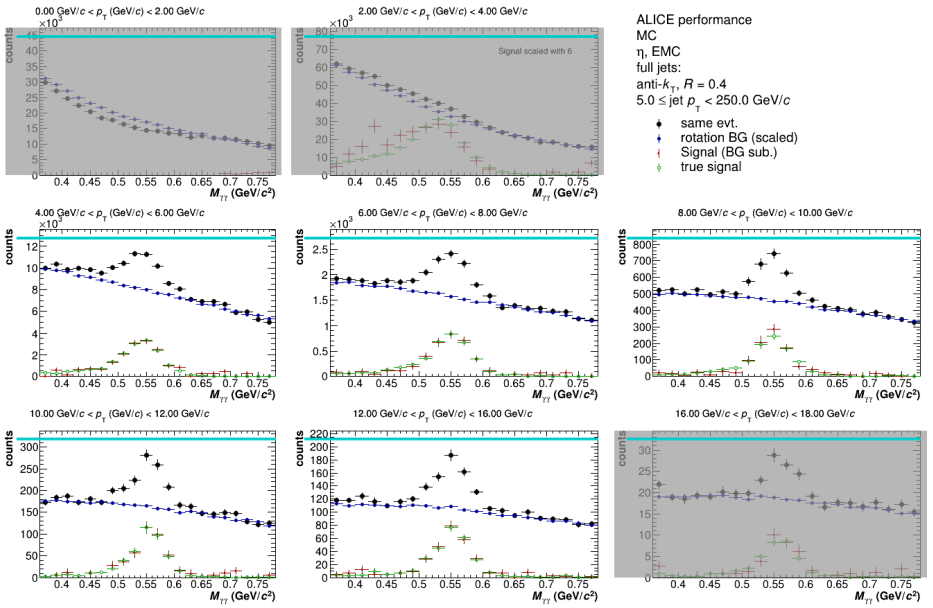
0.00 GeV/c < p_T (GeV/c) < 2.00 GeV/c
2.00 GeV/c < p_T (GeV/c) < 4.00 GeV/c
Signal scaled with 6
4.00 GeV/c < p_T (GeV/c) < 6.00 GeV/c
6.00 GeV/c < p_T (GeV/c) < 8.00 GeV/c
8.00 GeV/c < p_T (GeV/c) < 10.00 GeV/c
10.00 GeV/c < p_T (GeV/c) < 12.00 GeV/c
12.00 GeV/c < p_T (GeV/c) < 16.00 GeV/c
16.00 GeV/c < p_T (GeV/c) < 18.00 GeV/c
counts
$M_{\gamma\gamma}$ (GeV/c^2)
ALICE performance
MC
η, EMC
full jets:
anti-k_T, R = 0.4
5.0 ≤ jet p_T < 250.0 GeV/c
same evt.
rotation BG (scaled)
Signal (BG sub.)
true signal

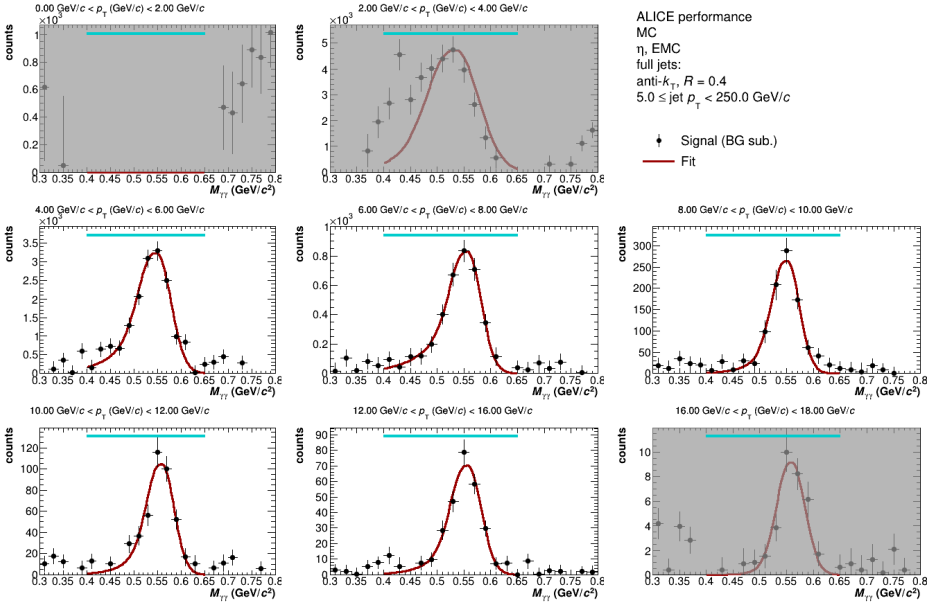
0.00 GeV/c < p_T (GeV/c) < 2.00 GeV/c
2.00 GeV/c < p_T (GeV/c) < 4.00 GeV/c
4.00 GeV/c < p_T (GeV/c) < 6.00 GeV/c
6.00 GeV/c < p_T (GeV/c) < 8.00 GeV/c
8.00 GeV/c < p_T (GeV/c) < 10.00 GeV/c
10.00 GeV/c < p_T (GeV/c) < 12.00 GeV/c
12.00 GeV/c < p_T (GeV/c) < 16.00 GeV/c
16.00 GeV/c < p_T (GeV/c) < 18.00 GeV/c
counts
$M_{\gamma\gamma}$ (GeV/c^2)
ALICE performance
MC
η, EMC
full jets:
anti-k_T, R = 0.4
5.0 ≤ jet p_T < 250.0 GeV/c
Signal (BG sub.)
Fit

A.2 Single Jet Momentum Bin: PCM-EMC

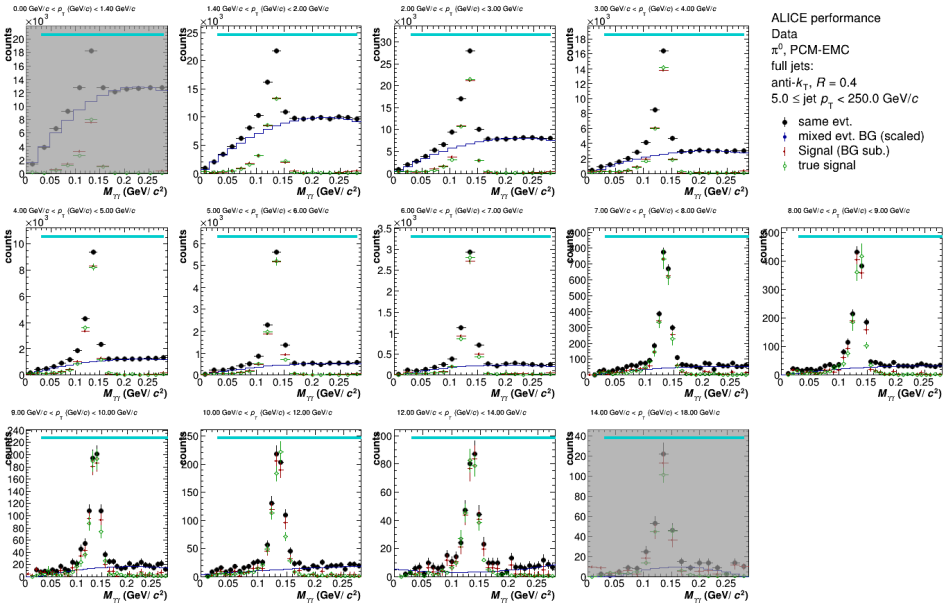

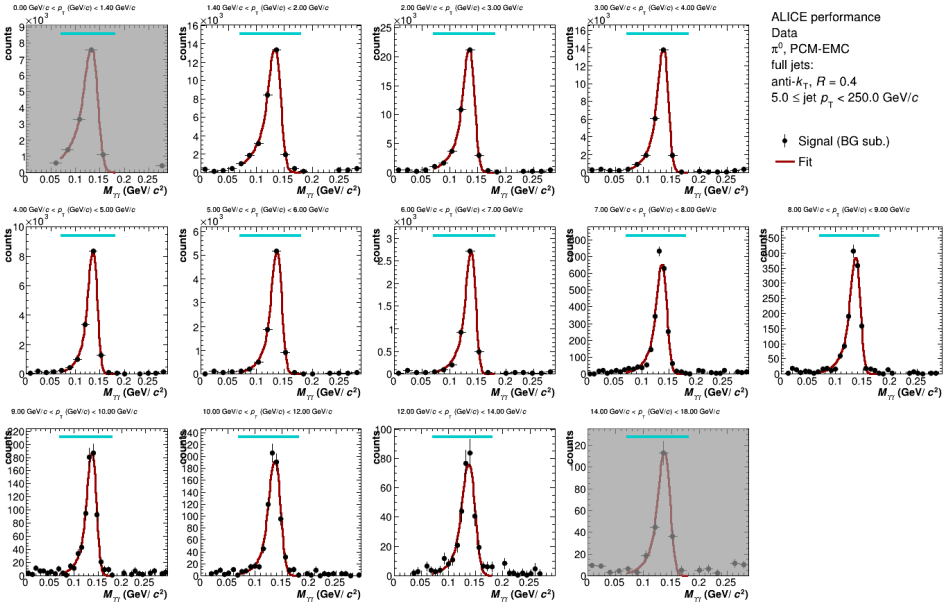

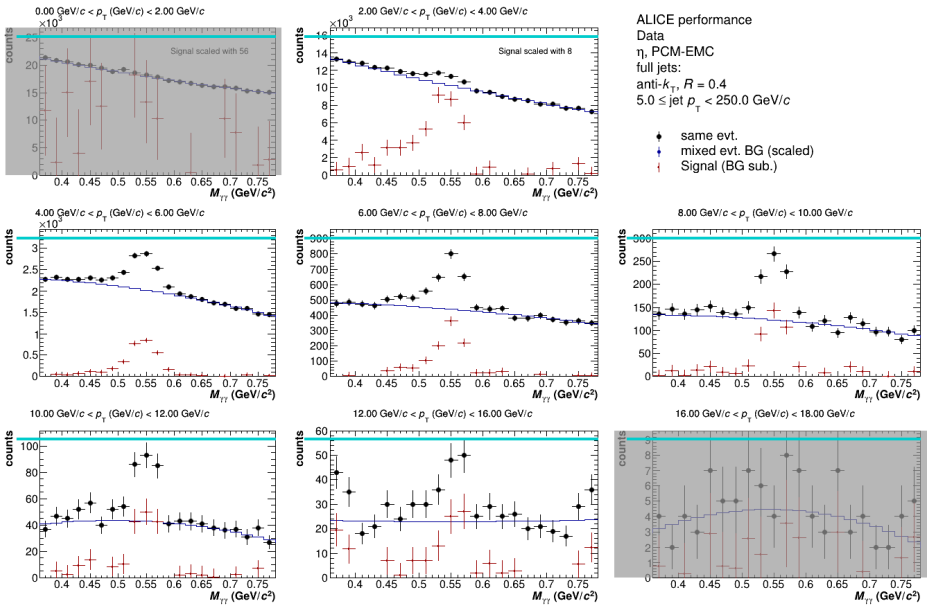
0.00 GeV/c < p_T (GeV/c) < 2.00 GeV/c
2.00 GeV/c < p_T (GeV/c) < 4.00 GeV/c
4.00 GeV/c < p_T (GeV/c) < 6.00 GeV/c
6.00 GeV/c < p_T (GeV/c) < 8.00 GeV/c
8.00 GeV/c < p_T (GeV/c) < 10.00 GeV/c
10.00 GeV/c < p_T (GeV/c) < 12.00 GeV/c
12.00 GeV/c < p_T (GeV/c) < 16.00 GeV/c
16.00 GeV/c < p_T (GeV/c) < 18.00 GeV/c
Signal scaled with 56
Signal scaled with 8
counts
M_γγ (GeV/c²)
ALICE performance
Data
η, PCM-EMC
full jets:
anti-k_T, R = 0.4
5.0 ≤ jet p_T < 250.0 GeV/c
same evt.
mixed evt. BG (scaled)
Signal (BG sub.)

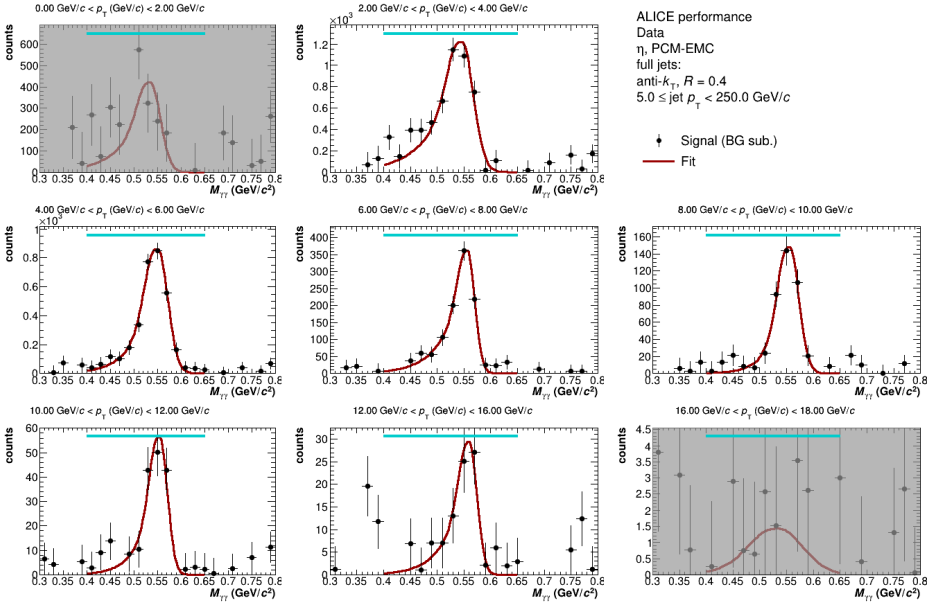
0.00 GeV/c < p_T (GeV/c) < 2.00 GeV/c
2.00 GeV/c < p_T (GeV/c) < 4.00 GeV/c
4.00 GeV/c < p_T (GeV/c) < 6.00 GeV/c
6.00 GeV/c < p_T (GeV/c) < 8.00 GeV/c
8.00 GeV/c < p_T (GeV/c) < 10.00 GeV/c
10.00 GeV/c < p_T (GeV/c) < 12.00 GeV/c
12.00 GeV/c < p_T (GeV/c) < 16.00 GeV/c
16.00 GeV/c < p_T (GeV/c) < 18.00 GeV/c
counts
M_γγ (GeV/c²)
ALICE performance
Data
η, PCM-EMC
full jets:
anti-k_T, R = 0.4
5.0 ≤ jet p_T < 250.0 GeV/c
Signal (BG sub.)
Fit

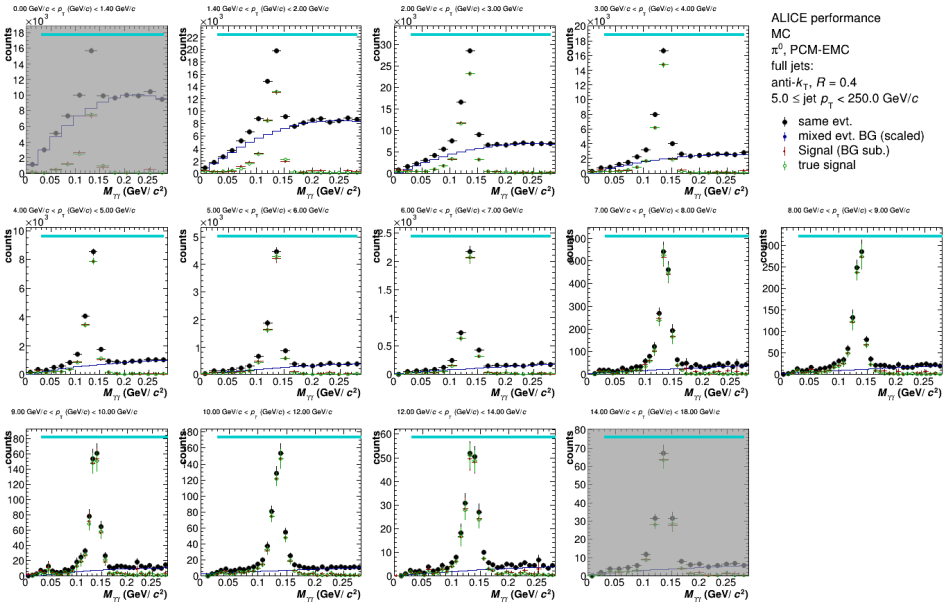
0.00 GeV/c < p_T (GeV/c) < 1.40 GeV/c
1.40 GeV/c < p_T (GeV/c) < 2.00 GeV/c
2.00 GeV/c < p_T (GeV/c) < 3.00 GeV/c
3.00 GeV/c < p_T (GeV/c) < 4.00 GeV/c
4.00 GeV/c < p_T (GeV/c) < 5.00 GeV/c
5.00 GeV/c < p_T (GeV/c) < 6.00 GeV/c
6.00 GeV/c < p_T (GeV/c) < 7.00 GeV/c
7.00 GeV/c < p_T (GeV/c) < 8.00 GeV/c
8.00 GeV/c < p_T (GeV/c) < 9.00 GeV/c
9.00 GeV/c < p_T (GeV/c) < 10.00 GeV/c
10.00 GeV/c < p_T (GeV/c) < 12.00 GeV/c
12.00 GeV/c < p_T (GeV/c) < 14.00 GeV/c
14.00 GeV/c < p_T (GeV/c) < 18.00 GeV/c
counts
$M_{\gamma\gamma}$ (GeV/ c^2)
ALICE performance
MC
π^0, PCM-EMC
full jets:
anti-k_T, R = 0.4
5.0 ≤ jet p_T < 250.0 GeV/c
same evt.
mixed evt. BG (scaled)
Signal (BG sub.)
true signal

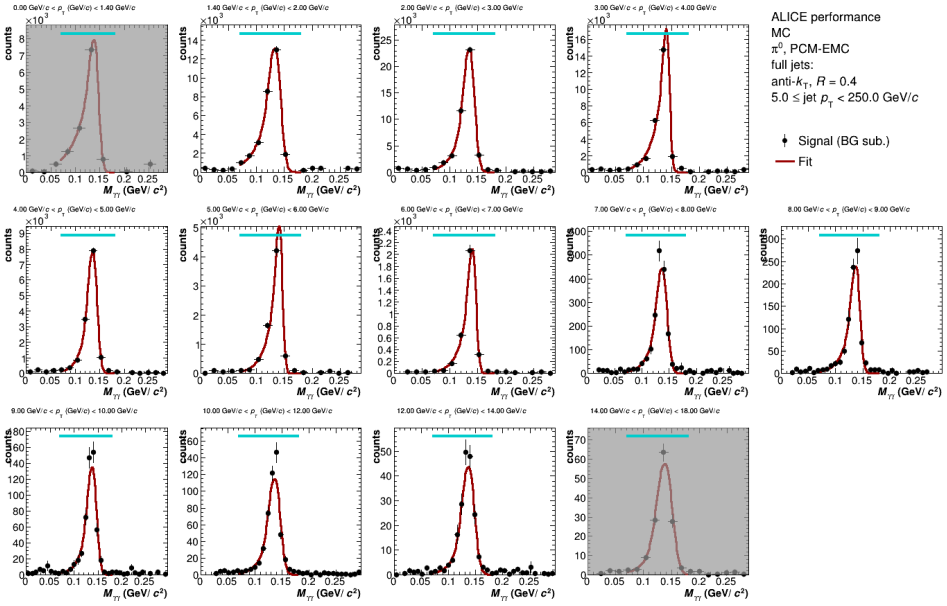
0.00 GeV/c < p_T (GeV/c) < 1.40 GeV/c
1.40 GeV/c < p_T (GeV/c) < 2.00 GeV/c
2.00 GeV/c < p_T (GeV/c) < 3.00 GeV/c
3.00 GeV/c < p_T (GeV/c) < 4.00 GeV/c
4.00 GeV/c < p_T (GeV/c) < 5.00 GeV/c
5.00 GeV/c < p_T (GeV/c) < 6.00 GeV/c
6.00 GeV/c < p_T (GeV/c) < 7.00 GeV/c
7.00 GeV/c < p_T (GeV/c) < 8.00 GeV/c
8.00 GeV/c < p_T (GeV/c) < 9.00 GeV/c
9.00 GeV/c < p_T (GeV/c) < 10.00 GeV/c
10.00 GeV/c < p_T (GeV/c) < 12.00 GeV/c
12.00 GeV/c < p_T (GeV/c) < 14.00 GeV/c
14.00 GeV/c < p_T (GeV/c) < 18.00 GeV/c
counts
$M_{\gamma\gamma}$ (GeV/ c^2)
ALICE performance
MC
π^0, PCM-EMC
full jets:
anti-k_T, R = 0.4
5.0 ≤ jet p_T < 250.0 GeV/c
Signal (BG sub.)
Fit

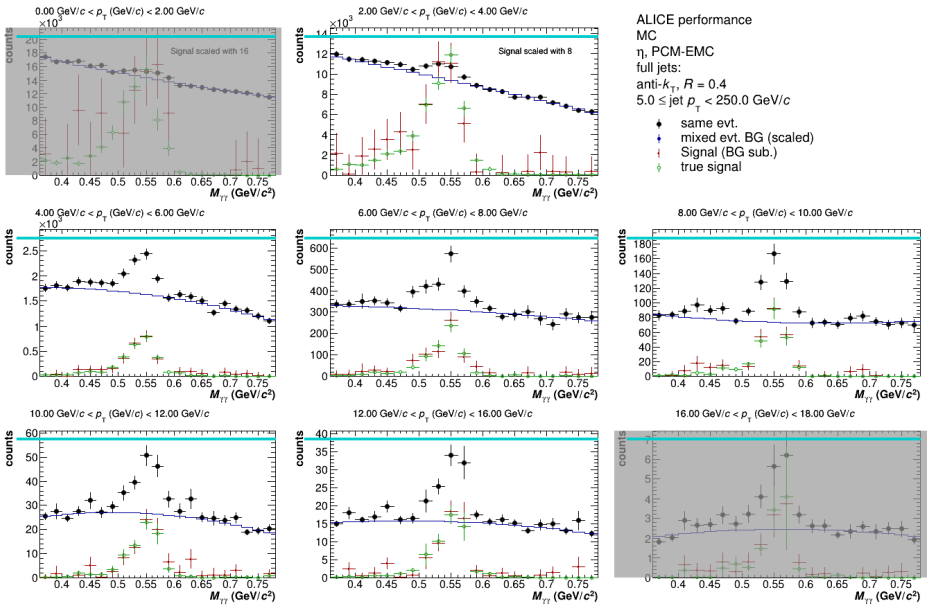
0.00 GeV/c < p_T (GeV/c) < 2.00 GeV/c
Signal scaled with 16
2.00 GeV/c < p_T (GeV/c) < 4.00 GeV/c
Signal scaled with 8
4.00 GeV/c < p_T (GeV/c) < 6.00 GeV/c
6.00 GeV/c < p_T (GeV/c) < 8.00 GeV/c
8.00 GeV/c < p_T (GeV/c) < 10.00 GeV/c
10.00 GeV/c < p_T (GeV/c) < 12.00 GeV/c
12.00 GeV/c < p_T (GeV/c) < 16.00 GeV/c
16.00 GeV/c < p_T (GeV/c) < 18.00 GeV/c
counts
M_γγ (GeV/c²)
ALICE performance
MC
η, PCM-EMC
full jets:
anti-k_T, R = 0.4
5.0 ≤ jet p_T < 250.0 GeV/c
same evt.
mixed evt. BG (scaled)
Signal (BG sub.)
true signal

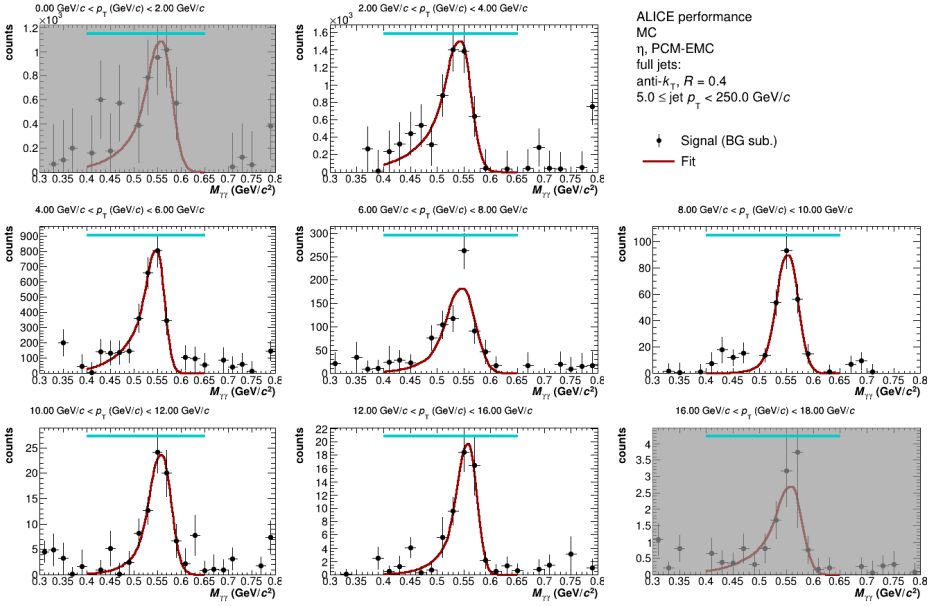
0.00 GeV/c < p_T (GeV/c) < 2.00 GeV/c
2.00 GeV/c < p_T (GeV/c) < 4.00 GeV/c
4.00 GeV/c < p_T (GeV/c) < 6.00 GeV/c
6.00 GeV/c < p_T (GeV/c) < 8.00 GeV/c
8.00 GeV/c < p_T (GeV/c) < 10.00 GeV/c
10.00 GeV/c < p_T (GeV/c) < 12.00 GeV/c
12.00 GeV/c < p_T (GeV/c) < 16.00 GeV/c
16.00 GeV/c < p_T (GeV/c) < 18.00 GeV/c
counts
M_γγ (GeV/c²)
ALICE performance
MC
η, PCM-EMC
full jets:
anti-k_T, R = 0.4
5.0 ≤ jet p_T < 250.0 GeV/c
Signal (BG sub.)
Fit

A.3 Dual Jet Momentum Bin: EMC-EMC

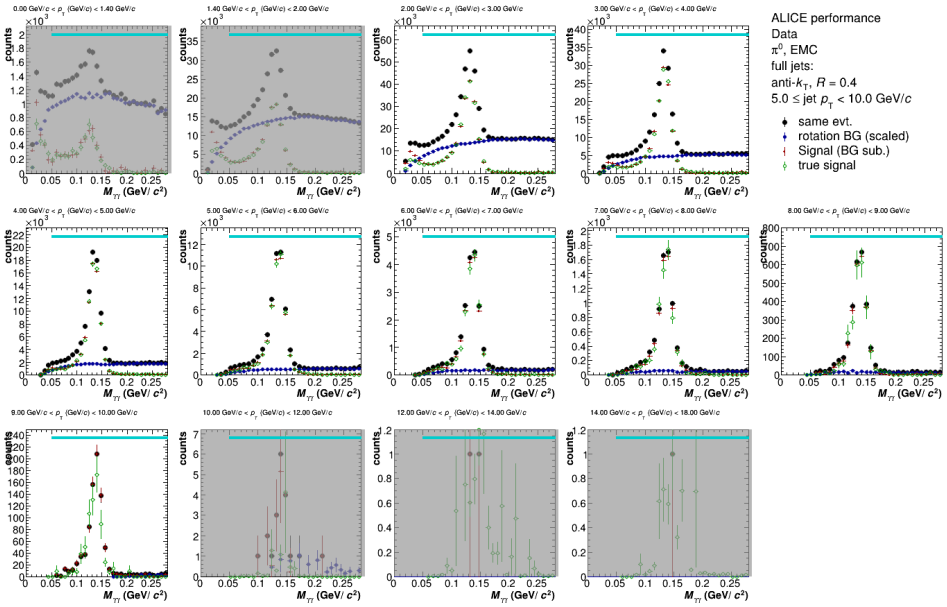

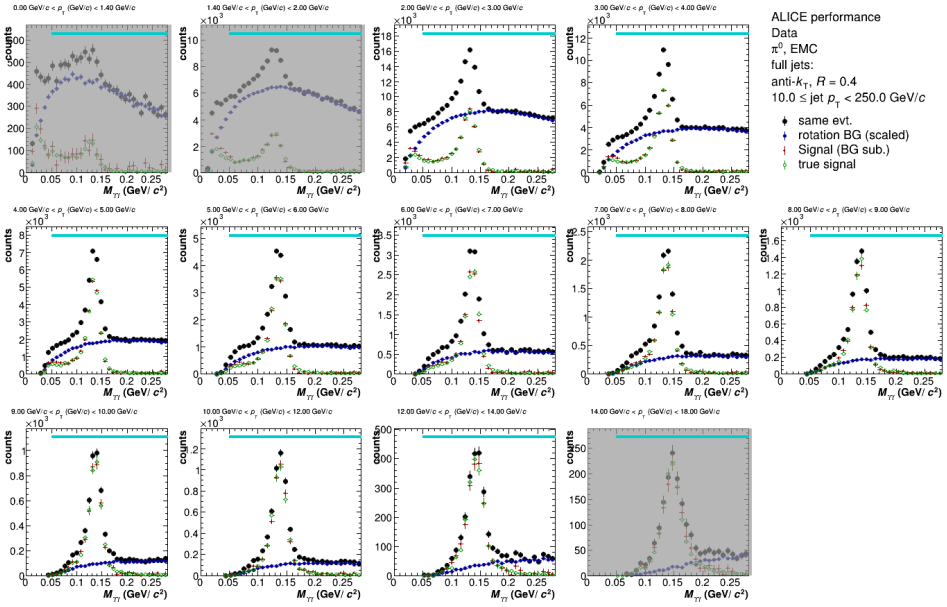

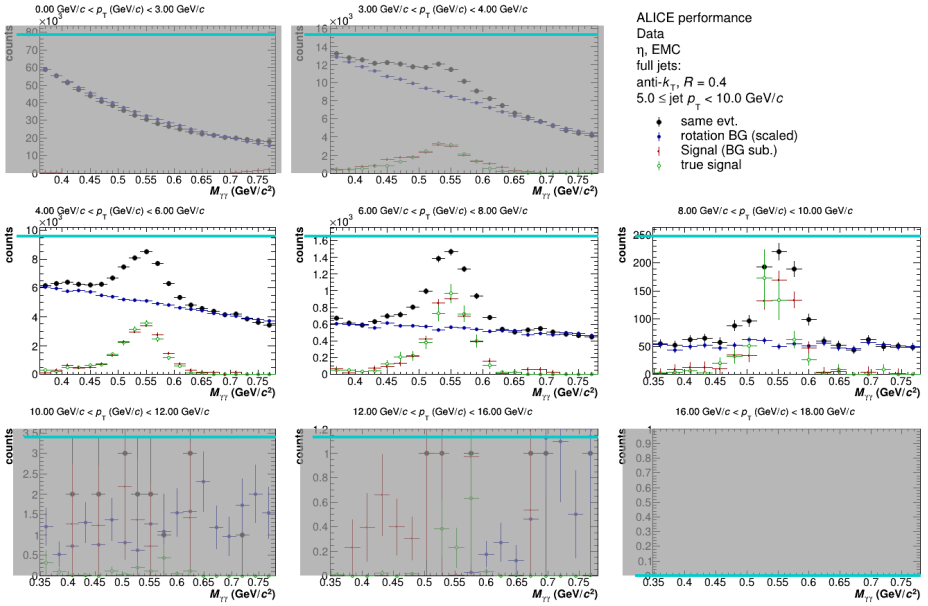
0.00 GeV/c < p_T (GeV/c) < 3.00 GeV/c
3.00 GeV/c < p_T (GeV/c) < 4.00 GeV/c
4.00 GeV/c < p_T (GeV/c) < 6.00 GeV/c
6.00 GeV/c < p_T (GeV/c) < 8.00 GeV/c
8.00 GeV/c < p_T (GeV/c) < 10.00 GeV/c
10.00 GeV/c < p_T (GeV/c) < 12.00 GeV/c
12.00 GeV/c < p_T (GeV/c) < 16.00 GeV/c
16.00 GeV/c < p_T (GeV/c) < 18.00 GeV/c
counts
$M_{\gamma\gamma}$ (GeV/c^2)
ALICE performance
Data
η, EMC
full jets:
anti-k_T, R = 0.4
5.0 ≤ jet p_T < 10.0 GeV/c
same evt.
rotation BG (scaled)
Signal (BG sub.)
true signal

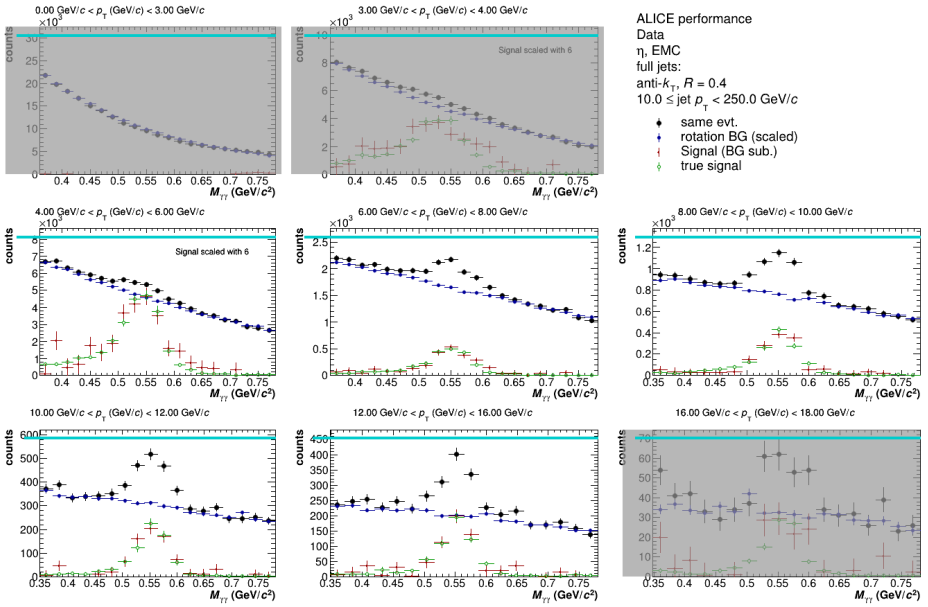
0.00 GeV/c < p_T (GeV/c) < 3.00 GeV/c
3.00 GeV/c < p_T (GeV/c) < 4.00 GeV/c
Signal scaled with 6
4.00 GeV/c < p_T (GeV/c) < 6.00 GeV/c
Signal scaled with 6
6.00 GeV/c < p_T (GeV/c) < 8.00 GeV/c
8.00 GeV/c < p_T (GeV/c) < 10.00 GeV/c
10.00 GeV/c < p_T (GeV/c) < 12.00 GeV/c
12.00 GeV/c < p_T (GeV/c) < 16.00 GeV/c
16.00 GeV/c < p_T (GeV/c) < 18.00 GeV/c
counts
$M_{\gamma\gamma}$ (GeV/c^2)
ALICE performance
Data
η, EMC
full jets:
anti-k_T, R = 0.4
10.0 ≤ jet p_T < 250.0 GeV/c
same evt.
rotation BG (scaled)
Signal (BG sub.)
true signal

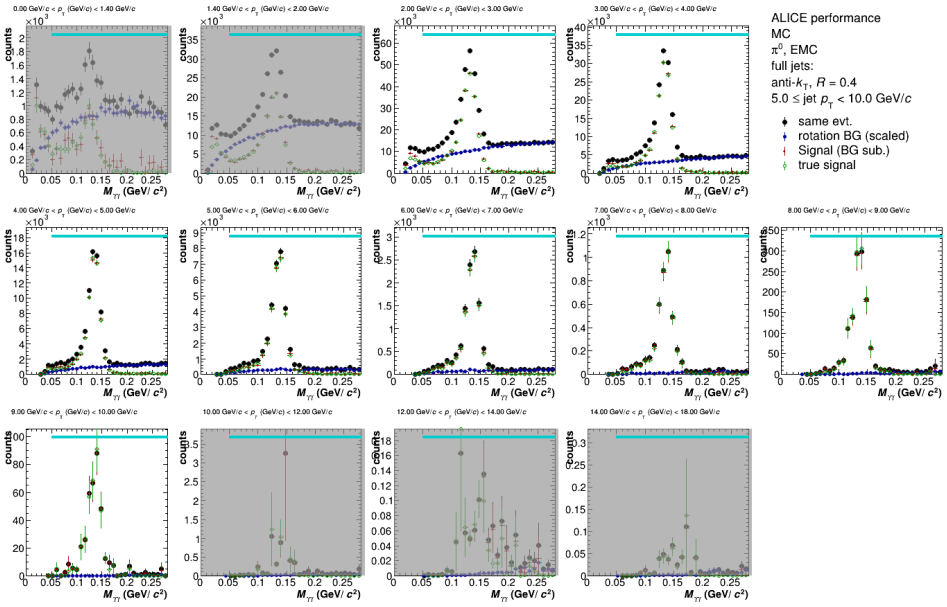
0.00 GeV/c < p_T (GeV/c) < 1.40 GeV/c
1.40 GeV/c < p_T (GeV/c) < 2.00 GeV/c
2.00 GeV/c < p_T (GeV/c) < 3.00 GeV/c
3.00 GeV/c < p_T (GeV/c) < 4.00 GeV/c
4.00 GeV/c < p_T (GeV/c) < 5.00 GeV/c
5.00 GeV/c < p_T (GeV/c) < 6.00 GeV/c
6.00 GeV/c < p_T (GeV/c) < 7.00 GeV/c
7.00 GeV/c < p_T (GeV/c) < 8.00 GeV/c
8.00 GeV/c < p_T (GeV/c) < 9.00 GeV/c
9.00 GeV/c < p_T (GeV/c) < 10.00 GeV/c
10.00 GeV/c < p_T (GeV/c) < 12.00 GeV/c
12.00 GeV/c < p_T (GeV/c) < 14.00 GeV/c
14.00 GeV/c < p_T (GeV/c) < 18.00 GeV/c
counts
$M_{\gamma\gamma}$ (GeV/ c^2)
ALICE performance
MC
π^0, EMC
full jets:
anti-k_T, R = 0.4
5.0 ≤ jet p_T < 10.0 GeV/c
same evt.
rotation BG (scaled)
Signal (BG sub.)
true signal

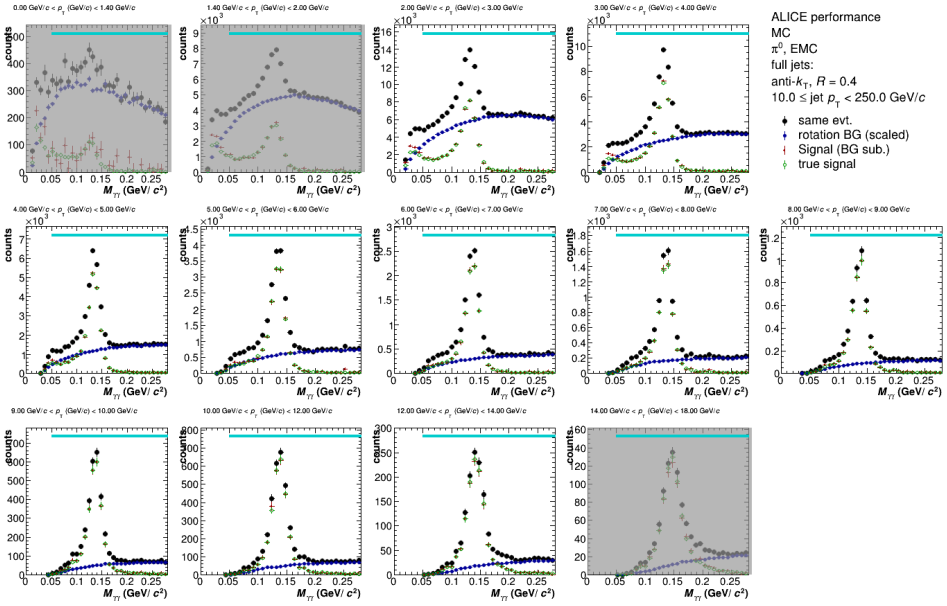
0.00 GeV/c < p_T (GeV/c) < 1.40 GeV/c
1.40 GeV/c < p_T (GeV/c) < 2.00 GeV/c
2.00 GeV/c < p_T (GeV/c) < 3.00 GeV/c
3.00 GeV/c < p_T (GeV/c) < 4.00 GeV/c
4.00 GeV/c < p_T (GeV/c) < 5.00 GeV/c
5.00 GeV/c < p_T (GeV/c) < 6.00 GeV/c
6.00 GeV/c < p_T (GeV/c) < 7.00 GeV/c
7.00 GeV/c < p_T (GeV/c) < 8.00 GeV/c
8.00 GeV/c < p_T (GeV/c) < 9.00 GeV/c
9.00 GeV/c < p_T (GeV/c) < 10.00 GeV/c
10.00 GeV/c < p_T (GeV/c) < 12.00 GeV/c
12.00 GeV/c < p_T (GeV/c) < 14.00 GeV/c
14.00 GeV/c < p_T (GeV/c) < 18.00 GeV/c
counts
$M_{\gamma\gamma}$ (GeV/ c^2)
ALICE performance
MC
π^0, EMC
full jets:
anti-k_T, R = 0.4
10.0 ≤ jet p_T < 250.0 GeV/c
same evt.
rotation BG (scaled)
Signal (BG sub.)
true signal

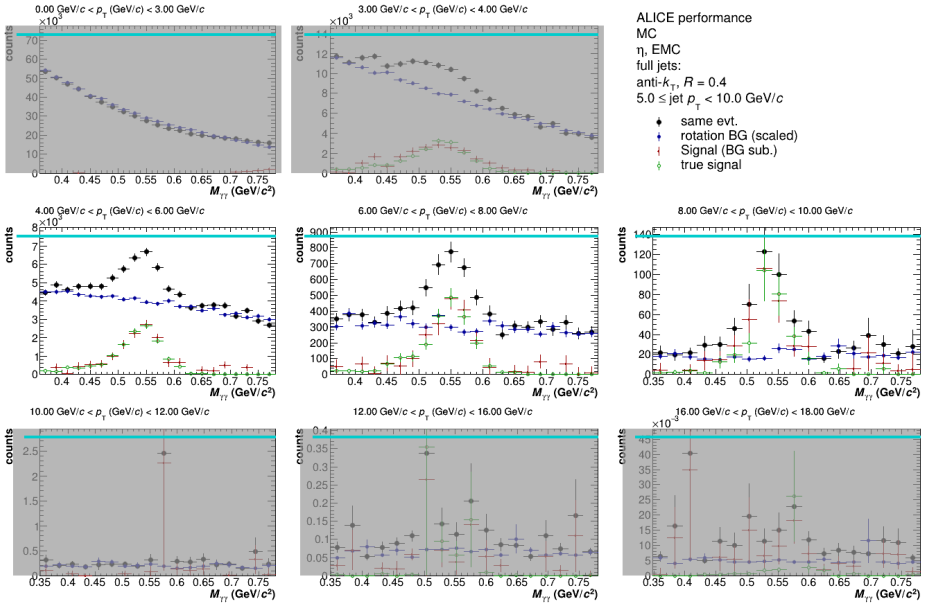
0.00 GeV/c < p_T (GeV/c) < 3.00 GeV/c
3.00 GeV/c < p_T (GeV/c) < 4.00 GeV/c
4.00 GeV/c < p_T (GeV/c) < 6.00 GeV/c
6.00 GeV/c < p_T (GeV/c) < 8.00 GeV/c
8.00 GeV/c < p_T (GeV/c) < 10.00 GeV/c
10.00 GeV/c < p_T (GeV/c) < 12.00 GeV/c
12.00 GeV/c < p_T (GeV/c) < 16.00 GeV/c
16.00 GeV/c < p_T (GeV/c) < 18.00 GeV/c
counts
$M_{\gamma\gamma}$ (GeV/c^2)
ALICE performance
MC
η, EMC
full jets:
anti-k_T, R = 0.4
5.0 ≤ jet p_T < 10.0 GeV/c
same evt.
rotation BG (scaled)
Signal (BG sub.)
true signal

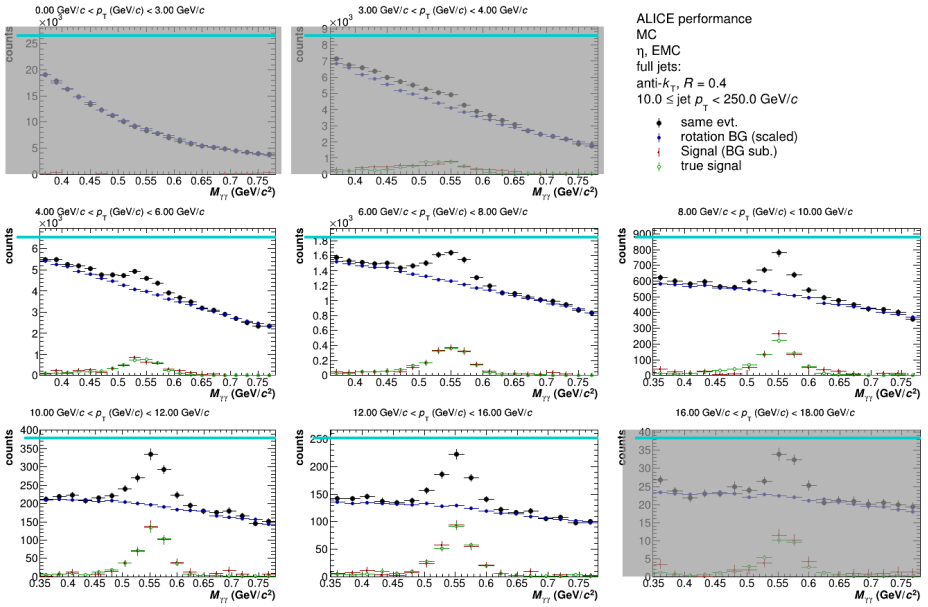
0.00 GeV/c < p_T (GeV/c) < 3.00 GeV/c
3.00 GeV/c < p_T (GeV/c) < 4.00 GeV/c
4.00 GeV/c < p_T (GeV/c) < 6.00 GeV/c
6.00 GeV/c < p_T (GeV/c) < 8.00 GeV/c
8.00 GeV/c < p_T (GeV/c) < 10.00 GeV/c
10.00 GeV/c < p_T (GeV/c) < 12.00 GeV/c
12.00 GeV/c < p_T (GeV/c) < 16.00 GeV/c
16.00 GeV/c < p_T (GeV/c) < 18.00 GeV/c
counts
$M_{\gamma\gamma}$ (GeV/c^2)
ALICE performance
MC
η, EMC
full jets:
anti-k_T, R = 0.4
10.0 ≤ jet p_T < 250.0 GeV/c
same evt.
rotation BG (scaled)
Signal (BG sub.)
true signal

References

[1] R. Aaij and others (LHCb Collaboration). Observation of $j/\psi p$ resonances consistent with pentaquark states in $\Lambda_b^0 \to j/\psi K^- p$ decays. *Phys. Rev. Lett.*, 115:072001, Aug 2015.

[2] J. Adams et al. Photon and neutral pion production in $Au + Au$ collisions at $\sqrt{s_{NN}} = 130gev$. *Physical Review C*, 70(4), 2004.

[3] S. Agostinelli et al. Geant4—a simulation toolkit. *Nuclear Instruments and Methods in Physics Research Section A: Accelerators, Spectrometers, Detectors and Associated Equipment*, 506(3):250–303, 2003.

[4] ALICE Collaboration. Eta/pi0 ratio inside jets as function of pt for different jet pt intervals with pythia, 2024. Accessed: 2024-02-14.

[5] ALICE O2 Group. Event mixing tutorial. https://aliceo2group.github.io/analysis-framework/docs/tutorials/eventMixing.html, 2024. Accessed: 2024-02-10.

[6] C. Bierlich, S. Chakraborty, N. Desai, L. Gellersen, I. Helenius, P. Ilten, L. Lönnblad, S. Mrenna, S. Prestel, C. T. Preuss, T. Sjöstrand, P. Skands, M. Utheim, and R. Verheyen. A comprehensive guide to the physics and usage of pythia 8.3, 2022.

[7] E. D. Bloom, D. H. Coward, H. DeStaebler, J. Drees, G. Miller, L. W. Mo, R. E. Taylor, M. Breidenbach, J. I. Friedman, G. C. Hartmann, and H. W. Kendall. High-energy inelastic $e - p$ scattering at 6° and 10°. *Phys. Rev. Lett.*, 23:930–934, Oct 1969.

[8] M. Cacciari, G. P. Salam, and G. Soyez. The anti-ktjet clustering algorithm. *Journal of High Energy Physics*, 2008(04):063–063, Apr. 2008.

[9] A. Collaboration. Performance of the alice electromagnetic calorimeter in lhc run 2 and its upgrade for run 3. *arXiv*, September 2022. CERN-EP-2022-197.

[10] M. Gyulassy and L. McLerran. New forms of qcd matter discovered at rhic. *Nuclear Physics A*, 750(1):30–63, Mar. 2005.

[11] J. Harris and B. Müller. The search for the quark-gluon plasma. *Annual Review of Nuclear and Particle Science*, 46(1):71–107, 1996.

[12] J. König. Measurement of light neutral meson production inside jets in pp collisions at $\sqrt{s} = 13$ tev with alice. Presented at Meson and Photon PAG Meeting, June 2023.

[13] V. S. Lang. *Measurement of the W boson production in association with jets using $\sqrt{s} = 8TeV$ proton-proton collisions at the ATLAS detector*. Dissertation, University of Heidelberg, Heidelberg, 07 2016.

[14] C. Lippmann. Performance of the alice time projection chamber. *Physics Procedia*, 37:434–441, 2012. Proceedings of the 2nd International Conference on Technology and Instrumentation in Particle Physics (TIPP 2011).

[15] M. M. Mondal and S. Chattopadhyay. A measurement of intrinsic transverse momentum of parton (kt) from two particle correlations for pp collisions at rhic. In *Proceedings of the International Symposium on Nuclear Physics*, page 542. Variable Energy Cyclotron Centre, Kolkata, India for STAR Collaboration, 2009.

[16] C. Nattrass. Measurements of jets in alice. *Acta Physica Polonica B*, 47(6), 2016.

[17] B. M. K. Nefkens and J. W. Price. The neutral decay modes of the eta-meson. *Physica Scripta*, T99(1):114, 2002.

[18] M. Omer and R. Hajima. Geant4 physics process for elastic scattering of γ-rays. 06 2018.

[19] C. Rizzi. *Proton-Proton Interactions and Their Simulation*, pages 69–81. Springer International Publishing, Cham, 2020.

[20] K. Røed, K. Ullaland, H. Helstrup, and T. Natås. Single event upsets in sram fpga based readout electronics for the time projection chamber in the alice experiment.

[21] M. Sas and J. Schoppink. Event shapes and jets in e+e and pp collisions. *Nuclear Physics A*, 1011:122195, 2021.

[22] M. H. P. A. Sas. *Illuminating Light: Neutral meson production and direct photon correlations from small to large collision systems at the LHC*. PhD thesis, Universiteit Utrecht, Utrecht, The Netherlands, June 2021.

[23] P. Steffanic. Heavy flavour in jets and azimuthal correlations. 06 2018.

[24] M. Thomson. *Modern Particle Physics*. Cambridge University Press, Cambridge, 2013.

[25] R. Workman and others (Particle Data Group). Review of Particle Physics. *Progress of Theoretical and Experimental Physics*, 2022(8):083C01, 08 2022.